POWDER INJECTION MOULDING OF TUNGSTEN BASED METAL MATRIX COMPOSITES

SHAUN HO PAN-WEI

A THESIS SUBMITTED FOR THE DEGREE OF DOCTOR OF PHILOSOPHY

DEPARTMENT OF MECHANICAL ENGINEERING

NATIONAL UNIVERSITY OF SINGAPORE

2009

ACKNOWLEDGEMENTS

This thesis would not have been possible without the support and direction of my supervisors, Professor Jerry Fuh Ying Hsi of the National University of Singapore (NUS) and Dr Li Qingfa of the Singapore Institute of Manufacturing Technology (SIMTech). Their guidance and constant encouragement was priceless during the entire course of my candidature.

I would also like to show my appreciation to the staff of the Forming Technology Group (FTG) of SIMTech. Mr Ho Meng Kwong, Mr Eric Pook, Dr Li Tao, Ms Yu Poh Ching and Ms Zhang Suxia constantly supported and challenged me with their knowledge and expertise in their respective fields, shaping my thesis and helping me chart a clear course of action throughout my work.

I would also like to thank the staff of the Department of Mechanical Engineering, NUS, with special mention to Professor Lu Li, Professor Manoj Gupta, Mr Maung Aye Thein, Dr Eugene Wong, Mr Ng Hong Wei and Ms Zhong Xiang Li for the assistance rendered during the phases of the study that were conducted in NUS.

Last but not least, I would like to thank my family for being pillars of support during the entire course of my study.

TABLE OF CONTENTS

SUMMARY

Due to their high hardness, thermal conductivity, electrical conductivity, wear resistance and customizable coefficient of thermal expansions (CTE), tungsten copper metal matrix composites (MMCs) have a wide variety of applications, especially in the fields of high current electrodes and thermal management.

Despite their widespread use, methods of manufacture have been largely confined to the infiltration of tungsten compacts produced by traditional powder pressing techniques.

This study explored methods and conditions that would make Powder Injection Moulding (PIM), a relatively new technology, suitable as a manufacturing precursor in producing MMCs with the aim of developing a more compact and robust processing method which could produce samples with high hardness, conductivity and percentage copper while retaining microstructural homogeneity and zero porosity. Variables such as the atmosphere, sintering/infiltration temperatures, sintering/infiltration holding times and feedstock compositions were attempted and their resulting products characterized.

Over moulding, infiltration joining, microwave sintering and powder pressing of yttria doped feedstocks were also attempted to further understand the mechanisms and processes involved. With the success of processing samples using tungsten and copper, the method was translated to the processing of tungsten silver MMC’s.

Optimum conditions were established through the analysis of data and explanations of significant features were presented. Mathematical models of infiltration and the conditions required for joining were also presented.

LIST OF FIGURES

LIST OF TABLES

LIST OF SYMBOLS

k_o	Grain growth equation constant
R	Universal gas constant
L	Lorenz number
g	Acceleration due to gravity.
G	Gravitational constant
Re	Reynold’s number
Z	Infiltration number
D_{final}	Final grain size
$D_{initial}$	Initial grain size
Q	Activation energy
T	Sintering temperature
t	Sintering time
r	Grain radius
γ	Surface energy per unit area (surface tension)
H_V	Vickers hardness
D_{ind}	Length of Vickers indentation
σ_y	Material yield strength
ρ_{resist}	Bulk resistivity
s	Spacing between probes of 4 point probe.
I	Applied current
V	Measured voltage

σ	Electrical conductivity
K	Thermal conductivity
B	Length
ρ_{liquid}	Density of infiltrating liquid
ρ_{sample}	Density of sample
ρ_{water}	Density of water
ρ_{w}	Density of tungsten
w_{air}	Weight in air
w_{water}	Weight in water
θ	Contact angle between liquid and solid phases
θ_{c}	Critical contact angle
X	Depth of submergence of the particle
F	Vickers indentation force
F_{displ}	Displacement force
$F_{Capillary}$	Capillary force
F_{υ}	Force acting on the particle-boundary interface
F_{sep}	Separation force
F_{drag}	Drag force
F_{weight}	Weight
$F_{gravitation}$	Force of gravity
η	Viscosity of liquid metal
v	Velocity
V_f	Volume fraction

d	Grain diameter
P_s	Pinning pressure
$\sigma_{sinter\ bond\ pressure}$	Sinter bond pressure
J	Neck diameter
N	Coordination number
h	Height
l	Neck radius and thinnest point
μ	Radius of curvature
α	Coefficient of thermal expansion of a material
$\alpha_{W\text{-}Cu}$	Coefficient of thermal expansion of tungsten copper MMC
α_{W}	Coefficient of thermal expansion of pure tungsten
α_{Cu}	Coefficient of thermal expansion of pure copper
m	Mass

1. Introduction

Tungsten (also known to some as wolfram) as a basis of composites have been a mainstay in commercial and industrial applications in the last century. Tungsten's high hardness (350H_V) and high melting point (3422°C, the highest among all known metals) has made machining and casting difficult. Tungsten's body centred cubic structure also results in its exceptionally low malleability, and makes cold working costly [1].

Copper however tells an entirely different story. Copper is a soft (38H_V) malleable metal that can easily be manipulated. The combination of copper's abundance, high conductivity (Table 1.1) as well as its ease of processing has made it one of the most popular materials for electrical and thermal dissipation applications [2, 3].

Table 1.1: Conductivities of Copper and Silver at 27°C

Thermal conductivity of Copper	$401 W\cdot m^{-1}\cdot K^{-1}$
Thermal conductivity of Silver	$429 W\cdot m^{-1}\cdot K^{-1}$
Electrical conductivity of Copper	$59.6 \times 10^6 S\cdot m^{-1}$
Electrical conductivity of Silver	$63.0\times 10^6 S\cdot m^{-1}$

From heat sinks to electrical wires to bronze statues, copper has had a profound influence on society at large. Despite having lower conductivities as compared to silver (Table 1.1), the relative abundance of copper both from mined and renewable resources has made its price low and more preferred over silver in a wide range of applications.

Copper, however, is also not without its weaknesses. Copper is considered too soft for many applications and has an extremely high coefficient of thermal expansion (CTE, $16.5 \times 10^{-6} K^{-1}$ at 25°C).

Given the merits and limitations of both materials, it was clear that a material that combined the hardness, wear resistance and low CTE of tungsten but possessed the conductive properties of copper would be in demand.

Their first known patent application for a composite of this nature was granted in 1915 and assigned to William D. Coolidge of the General Electric Company of America. His filing [4] was that of a simple composite where copper was adhered to a layer of tungsten by means of melting in a vacuum furnace. The proposed application of this was in the manufacture of X-ray targets. Tungsten being extremely dense is second only to lead when it comes to X-ray shielding. The method described in the patent was practiced in the early part of the 20th century and was nonetheless crude, producing products of tungsten and copper that where at best layered sandwiches of the two metals. Over the following half century, this combination of materials received only a lukewarm reception from industry players due in part to the high hardness and melting point of tungsten that made it very difficult to process.

Given Coolidge's revelation in 1915, it became apparent that both copper and tungsten were in fact, suitable as co-composite materials. In 1917, Charles L. Gebauer of Cleveland Ohio filed a patent [5] in which two metals of differing melting points could be processed into a homogenized composite. This method described briefly a technique in which a loose collection of chopped tungsten wires could be infiltrated by a lower melting point metal. This filing however was limited by its lack of detail as to how a net shape could be achieved. It is assumed from the patent description that the composite would take the shape of the receptacle by which infiltration occurred, and relied on post processing machining to develop the material into a desired shape.

Despite the knowledge that was present in producing MMCs based on the tungsten copper duality, the challenge at this point was to develop a process by which a net shape could be obtained with minimal need for post production machining.

The key to this seemed to be a method that had its roots as early as 1200 B.C. Powder Metallurgy (PM) is a technique that allows powders to be used in the formation of complex metal and ceramic parts. Despite its widespread use, it was only formally patented in 1941 by William Lamatter and Patrick Hume [6]. The relevance of this age old technique was the fact that it could be used to fabricate uniformly porous metal matrices through the formation of cold welds between adjacent particles. In 1925, Clemens A. Laise of Haworth, New Jersey filed a ground breaking patent that described a revolutionary method of manufacturing tungsten-copper metal matrix composites that had until then, not been used [7]. He described the formation of tungsten powder compacts by means of pressing and subsequent sintering at 900°-1000°C. These compacts were then dipped in baths of molten copper to produce metal matrix composites of copper and tungsten.

What Laise had done in his filing was described as the method which would later be popularly known as the press-sinter-infiltrate technique. Since his patent, there have been numerous variations of the process by which molten metals have been added into a porous preform produced by PM. The basis of producing the porous tungsten compacts by means of PM is still practiced widely today by most industry players in forming tungsten based metal matrix composites.

In 1961 a similar patent [8] describing the infiltration of a tungsten preform was filed. The difference between Laise and Weeton *et al.* was that while Laise prescribed full immersion of the preform into the molten bath, Weeton *et al.* described the infiltration by means of capillary action, where the fine open pores within the tungsten matrix act to draw molten copper in. The tungsten matrix described in the latter patent was however merely a bundle of loosely cut wires and the question of homogeneity as well as composition within the final composite was also in question.

Despite the technological capability at this juncture, tungsten-copper metal matrix composites never really found head way as a commercial mainstay. Applications in the early and middle part of the 20th century were limited. It was only with the advent of semiconductors in the 1960's that an enormous application for tungsten copper was unearthed.

In 1959, two researchers at Fairchild Semiconductor, Jean Hoerni and Robert Noyce developed a way to make silicon transistors. This method proved highly successful and the discovery catalyzed a global consumer electronics boom. One vital component of a semiconductor component was its packaging. The packaging had to be durable enough to protect the silicon chip from the environment, while dissipating heat away from the silicon component to prevent heat induced damage. While copper was a good heat dissipater, it's coefficient of thermal expansion (CTE) was considered too high to be compatible with a silicon substrate. CTE mismatches between a packaging and its carrier chip would result in strains within the chip, causing lower efficiency and possible failure. This issue of CTE mismatch ruled out pure copper as a packaging material for silicon substrates in the billion dollar semiconductor industry[9]. The solution would lie in a composite of copper containing an amount of tungsten. A combination of both materials would result in a composite that could have its CTE tailored to one that matched the silicon substrate based on its operating temperature. The MMCs durability as well as its relatively high conductivity also made it an obvious choice for semiconductor packaging.

Apart from the use of tungsten-copper in the semiconductor industry, the middle of the century also brought about new applications for tungsten based composites as electrodes for high current applications like electro discharge machining (EDM), electro chemical machining (ECM) and resistance welding (RW) [10-12]. Tungsten's high wear resistance and melting point complemented copper's excellent conductivity and produced electrodes that were able to withstand the high temperatures produced in such high current applications. While the former two applications were isolated to the field of mould and die manufacturing, the latter application allowed the composite to tap into the growing automobile and aerospace industry [13]. With this technology, a related composite, tungsten-silver, began to emerge. Although silver was deemed too costly in the production of semiconductor packages, its high conductivity was deemed necessary in high current contacts and electrodes (usually in excess of 50A) where a slight increase in resistivity would lead to unnecessarily high heating rates and energy losses that would reduce the life of the composite. [14-16].

In 1976, Ronald Rivers of Kokomo, Indiana officially filed a patent describing another method that could produce porous tungsten skeletons. This method, known generally as Powder Injection Moulding (PIM), and in this context specifically as Metal Injection Moulding (MIM), was an offshoot of polymer injection moulding where the polymer feedstock now contained an additional component of metals. This new method boasted the versatility and speed of production at a reduced cost that was already synonymous with PIM. Borrowing manufacturing and design principles that had long been established during the formative years of injection moulding, porous compact formation by means of injection moulding and polymer removal became accepted as an alternative to the conventional methods that were described by Laise.

The broad focus of this doctoral study was to examine and establish a series of streamlined conditions by which tungsten-copper metal matrix composites could be manufactured using the PIM technique. Considerations of this study included the time used in producing a homogenous pore free component, the relative cost of production (in terms of minimizing material wastage) and finally, the control of tungsten grain growth within the tungsten matrix. There has been great interest with regards to grain size on the effect of metal components since Hall and Petch’s simultaneous discoveries [17]. This aspect, however, has not been studied with respect to tungsten-copper MMCs produced by PIM and was embarked on in this report.

The first step of the PIM process was the manufacture of feedstocks for both copper and tungsten. Copper and tungsten were separately mixed with suitable polymeric binders that facilitated the flow of the softened feedstock during the injection moulding process. The volume loading of the polymeric binders within the tungsten feedstock was determined based on the level of porosity that was to be present within the tungsten preform. The polymeric binders within the copper feedstock were calculated based on the amount of copper to be present within the finished MMC. Polymeric binders and metal powders were heated, mixed and palletized to form pellets that could be easily fed into an Arburg Allrounder PIM machine and Battenfeld microsystem 50 micro injection moulding machine.

For the injection moulding process, pellets were fed into a heated injection moulding barrel via a hopper. The hopper feeds the pellets into a heated barrel by means of gravity. The barrel is heated to melt the polymeric binders present within the feedstock to lower its viscosity and facilitate its flow. A screw is present inside the barrel and both screw and barrel are coated with a layer of tungsten carbide to increase service life in light of the processing of hard metals and ceramics. The screw rotates and pushes softened heated feedstock towards the tapered tip of the barrel by means of displacement. The rotation of the screw also homogenizes the softened feedstock and contributes to the heating process by means of shear. The softened feedstock is then forced into the front of barrel (just behind the barrel nozzle) where the screw flight is shallower. During the injection moulding process, the screw is momentarily counter rotated and withdrawn. This causes a collection of feedstock to be accumulated at the front of the screw behind the barrel’s nozzle. This collection of softened feedstock at this point is known as a shot. The screw is then pushed forward at a high pressure acting as a plunger, forcing the shot out of the nozzle into a closed mould. The feedstock is then allowed to cool and solidify within the mould. The mould is finally opened and a finished, moulded component is ejected.

Several methods of injection moulding were attempted in this study. Components produced using the Arburg Allrounder S included bimetallic two material tensile bars consisting of a layer of copper and tungsten, a component with complex features as well as a basic two material bar. Micro injection moulding of single as well as two-material micro tensile bars was also successfully conducted on the Battenfeld Microsystem 50 micro injection moulding machine.

Following injection moulding, the moulded components were soaked in an organic solvent for four hours at 50°C and later heated in a hydrogen furnace at 450°C for 1 hour to remove polymeric binders from within the copper and tungsten moulded parts.

In the next phase of the study, a suitable atmosphere was determined for infiltration. Atmospheres ranging from hydrogen, air, vacuum and nitrogen were attempted with varying degrees of success. The aim was to establish the most optimum atmosphere by which a pore free homogenous composite could be obtained. Subsequently, various orientations of the copper portion with respect to the tungsten matrix were also permutated to define an optimum orientation for successful infiltration.

After both optimum atmosphere and orientation were determined, various sintering temperatures above the melting temperature of copper were attempted. These temperatures were maintained for 60 minutes to facilitate concurrent sintering and infiltration of copper. The purpose of this step was to characterize the behaviour of the resulting composite with regards to peak processing temperatures.

From the results obtained from the previous sub-studies, an optimum temperature was chosen and dwell times were then varied to determine its effect on the MMCs properties.

Results obtained at this point using one micron tungsten powders were deemed satisfactory, having copper contents of as high as 35.0wt% copper. However, final tungsten grain sizes remained constant at the two micron range.

To achieve a finer tungsten grain size in the finished composite, it was necessary to begin processing with even finer tungsten powders. Hence further experiments involving a variation in dwell temperatures was attempted with tungsten powders averaging 100 nm in diameter.

On the side, microwave sintering (in air) was also attempted. This was done to determine if the inverse heating profiles and high heating rates that were synonymous with microwave sintering could lead to finer final grain sizes.

Experiments targeted at reducing the overall processing time and the amount of costly hydrogen used was also attempted. This was an economic consideration that would lower overheads (in terms of hydrogen, power and man hours) as well as increase production rate of the composite. These series of experiments saw the combination of the thermal debinding and sintering/infiltration cycle into one combined heat cycle. Subsequently an increase in heating rate from 3°C/min to 5°C/min was also used. The overall reduction in time was as much as 50% from start to finish, inclusive of the man hours required to start and stop the furnace. These changes to the heat cycles were met with success and tungsten-copper MMCs with an even higher percentage of copper were also achieved.

The methods attempted managed to push the amount of copper within the composite to a maximum of 35.0wt%. Tungsten-copper MMCs with this amount of copper are commercially available although only through conventional PM methods.

There was, however, still a desire to further increase the amount of copper within the finished MMCs. This led to a change in the composition of tungsten feedstock where apart from the usual tungsten and polymeric binders, a small amount of copper (5.0wt%) was also added. The presence of copper reservoirs within the tungsten matrix meant that the overall percentage of copper within the finished MMC would be increased. The hypothesis was that upon melting, these reservoirs of copper within the tungsten matrix would decrease infiltration time through adhesion forces between the infiltrating copper and the copper reservoirs. While this new feedstock did manage to increase the overall amount of copper within the MMC, the copper reservoirs were not able to shrink upon the melting of copper, leading to regions of structural inhomogeniety.

The final phase of the study was to control the grain growth of tungsten via zener pinning. In this step, yttria was mixed into the tungsten feedstock. Yttria particles impinge against the tungsten grain boundaries and prevented them from necking, hence reducing subsequent densification and coarsening. Preliminary studies were done using various amounts of yttria mixed with tungsten and pressed using conventional PM methods. Favourable combinations were then translated into feedstock for PIM [18]. The infiltrated MMCs displayed a homogenous microstructure with fine tungsten grains and no presence of voids. The results of the tests were encouraging as yttria has been theorized to have a high contact angle with copper and could impede infiltration.

As with most research studies, this study was also fraught with non technical challenges. One major challenge that was faced during the entire duration of the experiment was with the purchase of tungsten powders. Ever since the events of September 11, 2001, the import of tungsten powder into South-East Asia has been strictly controlled by the Department of Homeland Security of the United States of America. Declarations regarding the purpose and details of the purchasing organization have to be submitted before a sale can proceed. What this translated to during the course of the study was higher costs (especially for 100nm powders), longer lead times and smaller available quantities. In light of the small domestic demand and the difficulties involved, many local powder suppliers had given up dealing with tungsten powders completely. When a supplier was finally located, there was a nine month delay from the time the powder was first ordered to the actual receipt at the laboratory.

The use and availability of a suitable furnace was also limited. The very nature of the infiltration process and the presence of a molten fluid phase meant that the potential for furnace contamination was high. Running elevated temperatures under a flammable gas like hydrogen was dangerous and as such, there were numerous safety guidelines that had to be adhered to with regards to the operation of such furnaces. It was eventually decided that a CM tube furnace in SIMTech was suitable for the study, and that it was only to be done with the strictest supervision. This furnace was shared by other researchers on several other projects and the windows of opportunity by which the furnace could be utilized for the project was very limited.

The biggest challenge faced within this project was however not administrative or technical, but in fact human. In July of 2005, a student was assigned to do an honours project related to this doctoral study. By September he was given access to the samples to do testing. However in November of 2005, the student disappeared, and took along several critical samples. This set back the projects progress by almost six months as he had taken a third of the samples that were fabricated at that point. In the next six months that followed, the samples taken were painstakingly remanufactured and characterized. The student finally reappeared in July 2006, but by that time, the samples that he had held on to were already oxidized and were of no value to the project.

In summary, this study was aimed at defining a method by which tungsten based composites could be successfully produced by the PIM route. Work was carried out with respect to streamlining the operational aspects without compromising on the quality of the finished product. Steps were also taken to increase the quantity of copper present within the MMC. Subsequently, the control of grain growth experienced within the tungsten matrix was also investigated with several options explored. Despite the many challenges that were faced during its course, it is nonetheless the hope that the findings of this project will have a positive impact towards the industrial mass production of tungsten products and its related composites.

References

1. Briant, C.L., *Tungsten: properties, processing, and applications.* Advanced Materials & Processes, 1998. **154**(5): p. 29-32.
2. Hui, P. and H.S. Tan, *Temperature distributions in a heat dissipation system using a cylindrical diamond heat spreader on a copper heat sink.* Journal of Applied Physics, 1994. **75**(2): p. 748-757.
3. Prestona, S.D., I. Brethertona, and B. A.Forty, *The thermophysical and mechanical properties of the copper heat sink material intended for use in ITER* Fusion Engineering and Design, 2003. **66-68**: p. 441-446
4. Coolidge, W.D., *United States Patent 1,162,341, Composite Metal Body*. 1915.

5. Gebauer, C.L., *United States Patent 1,342,801, Process of producing metal bodies*. 1920.

6. Lamatter, W.D.W. and H.P. Henry, *United States Patent 2,363,575, Powder metallurgy* 1944

7. Laise, C.A., *United States Patent 1,633,258, Refractory metal alloy of high density and melting point and making method of the same*. 1927.

8. Weeton, J.W., et al., *United States Patent 3,138,837, Method of making fiber reinforced metallic composites* 1964.

9. Moore, G.E., *No exponential is forever: But "forever" can be delayed!* Solid-State Circuits Conference, 2003. Digest of Technical Papers. ISSCC. 2003 IEEE International, 2003. **1**: p. 20-23.

10. Forster, R., A. Schoth, and W. Menz, *Micro-ECM for production of microsystems with a high aspect ratio.* Microsystem Technologies 2, 2005: p. 246-9.

11. Lee, H.T., F.C. Hsu, and T.Y. Tai, *Study of surface integrity using the small area EDM process with a copper-tungsten electrode.* Materials Science and Engineering A, 2004. **364**(1-2): p. 346-356.

12. Marafona, J.W., Catherine *New method of optimising material removal rate using EDM with copper-tungsten electrodes.* International Journal of Machine Tools and Manufacture, 2000. **40**(2): p. 153-164.

13. Prucher, B.P., *United States Patent 4,476,372, Spot welding electrode*. 1984.

14. Lindmayer, M. and M. Roth. *Contact resistance and arc erosion of W/Ag and WC/Ag*. in *Proc. 24th Helm Conf. Elect. Contacts*. 1978.

15. Findik, F. and H. Uzun, *Microstructure, hardness and electrical properties of silver-based refractory contact materials.* Materials & Design, 2003. **24**(7): p. 489-492.

16. Kim, C.-H.L.H., *A Comparison of Ag/W,Ag/WC, and Ag/Mo Electrical Contacts.* IEEE Transactions on Components, Hybrids, and Manufacturing Technology, 1984. **7**(1): p. 69-75.

17. Kang, H.-K., *Tungsten/copper composite plates prepared by a modified powder-in-tube method.* Scripta Materialia, 2004. **51**(6): p. 473-477.

18. Ho, P.W., et al. *Effect of Yttria addition on the structure and hardness of porous tungsten matrices*. in *Proc.8th Asia Pacific Conference on Materials Processing*. 2008.

2. Literature Review

2.1. Brief review of the tungsten copper MMC

The first scientific record of the manufacture of tungsten copper MMCs was in 1939 in an article written by Dr C.J Smithells and published in nature [1]. Smithells described a method in which he had mixed tungsten, copper and nickel powders into a crucible. He later heated the mixture to 1450°C and moulded the resulting slag into a desired shape. This seminal discovery was for the purpose of radium shielding. The resulting composite was a solid dispersion of tungsten particles in copper. Being a dispersion and not within a contiguous network, the tungsten phase did not serve a structural function, but its high atomic mass made it suitable as a radiation shield. Tungsten copper is still used today in radiation shield applications [2, 3].

Apart from radiation shielding, applications ranging from disposable resistance welding electrodes [4, 5], heat sinks [6, 7] and semiconductor packaging [8-10] have made tungsten copper a popular candidate material in the consumer electronics industry. While the importance of the material has grown, the methods of manufacture have not been extensively researched. Many of the tungsten copper components today are still manufactured by methods developed during the early half of the 20th century.

Tungsten copper MMCs have intermediary properties of copper and tungsten, displaying excellent conductivities, a stable coefficient of thermal expansion and relatively high hardness [11-13]. The strong interfacial bonds formed between tungsten and copper [14, 15] accounts for its excellent toughness and strength. Tungsten copper

MMCs with tungsten grains in the region of 0.5μm have also been reported to be a candidate for ultra fine super strength materials [16].

Table 2.1 below shows a summary of the properties for some commercially available tungsten copper MMCs.

Table 2.1: Properties of tungsten copper MMCs [17-19]

Wt%Cu	Relative density (%)	CTE ($10^{-6}K^{-1}$)	Electrical conductivity (%IACS)
90	95	8.6	43%
90	82	4.7	36%
90	100	6.8, 6.0, 6.5	49%, 48%, 39%
85	100	6.7,7.4	51%, 42%
80	100	8.2, 8.2	54%, 45%
75	100	9.9, 9.1	60%, 48%

The manufacture of tungsten powder begins with the bulk purchase of Ammonium Paratungstate (APT), $(NH_4)_{10}W_{12}O_{41} \cdot 5\ H_2O$. This compound is the first intermediate material that is produced from tungsten ore purification. Subsequently, the APT is heated in a furnace under hydrogen at 900°C. This reduces and dries the APT to produce the oxide of tungsten, $W_{20}O_{58}$. $W_{20}O_{58}$ is then heated at a lower temperature of 800°C to produce pure tungsten powder. The powders are then agitated to break down any agglomerates and sieved by particle size. Due to the absence of high energy milling in the forming of fine tungsten powders, tungsten powders formed of 1μm and below are monoclinic [20, 21].

Figures 2.1 and 2.2 show the nominal prices for both tungsten and copper for the last 100 years [22, 23].

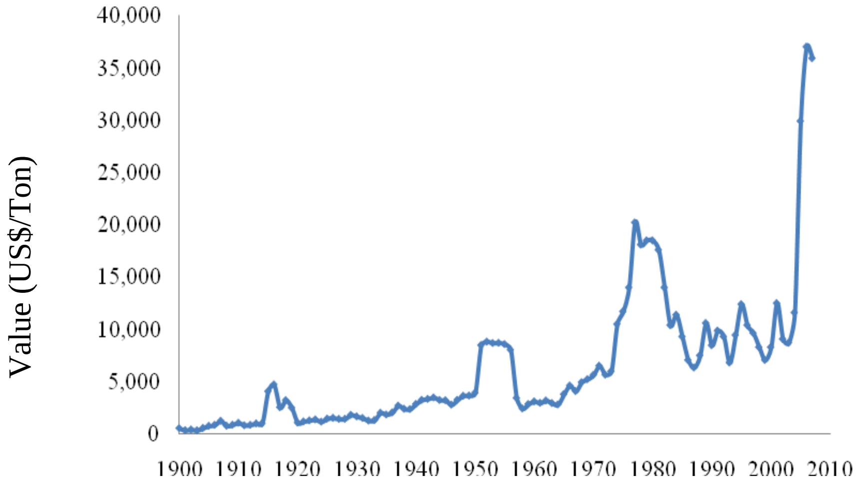

Figure 2.1: Tungsten prices for the last 300 years

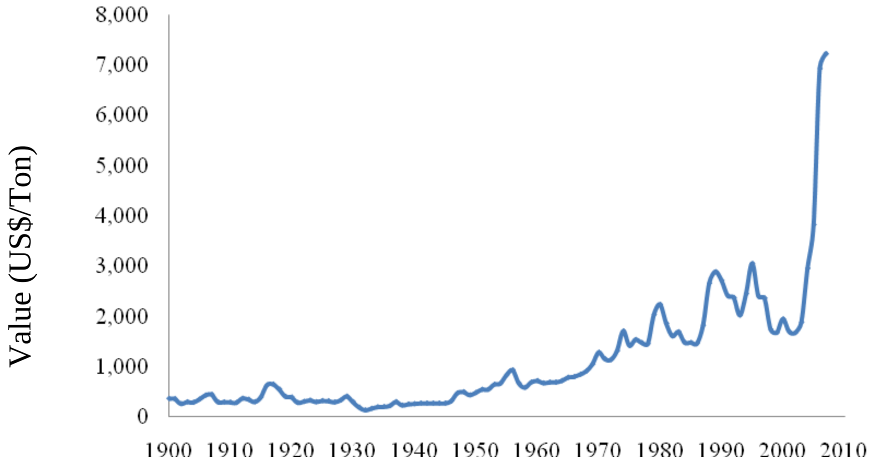

Figure 2.2: Copper prices for the last 100 years.

There has been a threefold surge in prices for both metals since 2000 despite advances in mining, extraction and recycling [24-30].

There is rising concern that copper is reaching peak levels [31-34]. Copper, being a finite resource has been mined extensively throughout out the last century. According to the Hubbert Peak Theory [35], once peak production levels have been reached, there will be a gradual reduction in the exhaustible resource, resulting in escalating prices due to increase demand and a lack of a substitutable commodity. The highest price for copper was recorded on 8th March 2008 and is set to rise further.

From Figure 2.3, the main use of copper is still in the electrical and building sectors, where its use in power transmission and piping is still dominant. This industry is still predicted to grow with increased industrialization and globalisation [22].

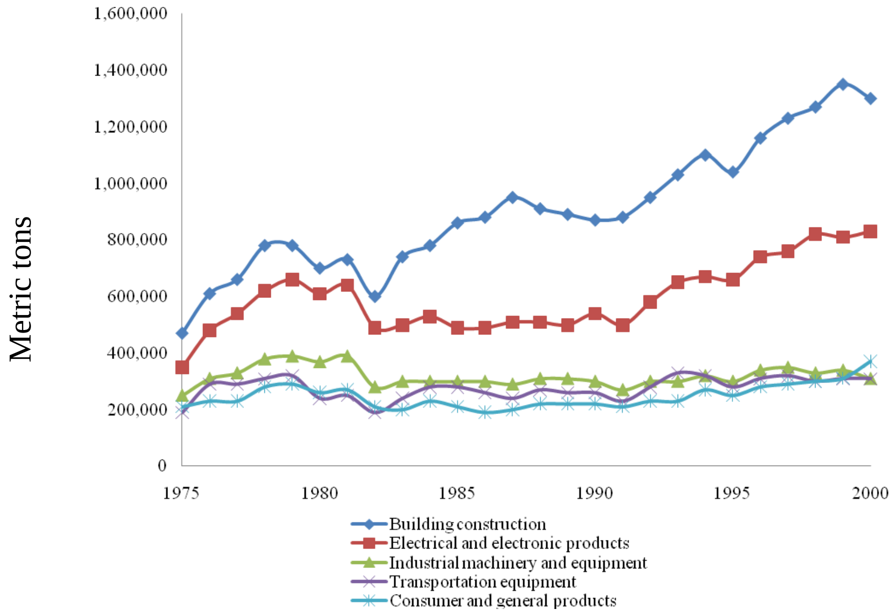

Figure 2.3: Major uses of copper within the past 25 years.

The use of tungsten is largely dominated by the carbide tooling industry (as seen in Figure 2.4). The introduction of power saving fluorescent illumination as opposed to traditional tungsten filament light bulbs has reduced dramatically the use of tungsten in the consumer and household sectors [36, 37].

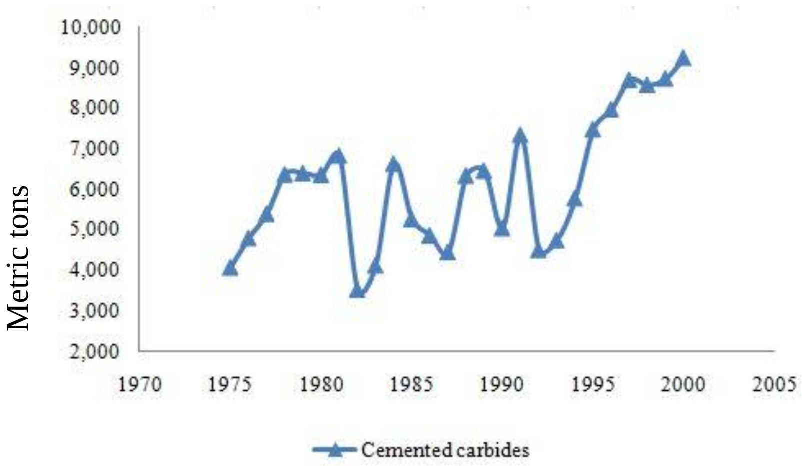

Figure 2.4: Use of tungsten in cemented carbides within the past 25 years.

For both materials, a combination of reduction in extraction as well as renewable resources and increase in demand has led to a sudden increase in prices within the last decade. It is therefore pertinent to explore new methods to reduce wastage within the manufacturing process.

2.2. Methods of manufacture

2.2.1. The press-sinter-infiltrate route

The predominant method of manufacture of tungsten copper MMCs is using the press-sinter-infiltrate technique [38, 39]. In this method powdered tungsten metal is consolidated using pressurized compaction and sintered to form a tungsten matrix. The compact is then heated to the melting point of copper in the presence of the latter. Copper is liquefied and distributes itself through the matrix while the tungsten matrix densifies and coarsens. Despite only being officially patented in 1999 by Yoo *et al* [40, 41], this method of infiltrating copper into a porous tungsten perform has been documented much earlier in previous publications [42, 43].

2.2.2. Compaction methods

Powder compaction and consolidation can be done in two ways. Die compaction (PM) and PIM. Die compaction has been used for decades and while it provides a simple concise method in producing tungsten compacts, due to the one dimensional nature of compaction, parts produced are less complex in nature with features only present in the direction of compaction [44]. Post sintering machining is required to create complex features in PM sintered parts. This additional step leads to a rise in overhead costs.

Due to friction between the tooling and powder, pressure gradients are present during PM compaction. These pressure gradients result in deformation during sintering and also dimensional scatter between individual components [45].

PIM does not have the limitations in part complexity as the die cavity does not change in shape during the compaction process. The lower pressures involved in PIM and the presence of a lubricating binder phase also reduces the amount of tooling-powder friction and results in a less undesirable pressure gradient.

The ability to automate the entire PIM process [46, 47] also serves to advance the tungsten matrix manufacturing process. The ability to control the amount of material in each shot precisely using a metering method also minimizes material wastage [48].

The ability of the PIM process to produce two material parts [49-52] opens the opportunity of conjoined tungsten copper bimetallic green parts. Such parts can be heated to produce copper infiltrated tungsten materials with minimum wastage and handling [53].

PM methods also reduce the amount of possible copper infiltration as compacted samples are more closely packed due to the higher pressures involved. PIM techniques involve the addition of a lubricating polymeric binder that forms the open pore network when removed [54]. The open porosity evolved during the debinding process translates directly to the amount of copper that can be introduced into the sample during the infiltration process.

In 2007, a report published [55] in a leading powder injection moulding journal reported that 60% of PIM companies based in North America (many with operations in Asia) have dedicated focuses on metal processing to serve the medical, aerospace and automotive industry. This value is likely to grow with further advances in metal injection moulding (MIM) technology, especially in the fields of micro-PIM components and MMCs [56]. The widespread acceptance of PIM over other traditional metal forming processes like machining and casting has made it an accessible and economical way to manufacture tungsten based composites.

Despite the popularity and versatility of PIM in forming composites, the main industry standard for forming of tungsten copper compacts is still PM [20, 57, 58]. Research related to this field is by and large within the scope of standard traditional powder pressing. Little research has been done with regards to using PIM as a manufacturing method for tungsten copper MMCs. Even the limited literature available is inclined towards feedstocks comprising of admixed tungsten and copper [41, 59-62].

2.2.3. Infiltration of tungsten by capillary action

Infiltration of a pure tungsten compact by means of capillary action has been the most common way in which tungsten copper MMCs have been formed [40, 43, 53, 63, 64]

This method involves having molten copper present when sintering the tungsten matrix. Copper can be introduced in two main ways; admixed with the tungsten prior to compaction or independently to the pure tungsten matrix via spontaneous infiltration. The low contact angle of molten copper with tungsten makes this process very suitable[14].

2.2.4. Admixing of tungsten with copper

Admixing copper and tungsten powders into homogenous powder mixtures has been a popular way of manufacturing tungsten based MMCs using powder precursors [59, 62, 65-70]. Admixing involves introducing the copper into the tungsten matrix upon compaction. This process is also known as mechanical alloying and is done by mixing copper and tungsten powder mixtures into a high energy ball mill [67]. The resulting powder mix is then either pressed directly and sintered in the PM route, or mixed with polymeric binders and injection moulded via the PIM route.

While this method has been shown to produce uniform microstructure, there is an inherent associated problem of porosity within the final MMC [65, 68]. Copper bleed out (Figure 2.5) is a common problem associated with admixed powders when copper amounts are large [71]. Bleed out leads to the necessity of post process machining and a significant drop in copper content.

Figure 2.5: Tungsten tensile bars infiltrated with copper displaying extensive copper bleed out.

Contamination has also been a problem associated with the admixing process [72]. Apart from metallic and ceramic inclusions during contamination, the presence of moisture and oxygen inside the milling crucibles result in the formation of an oxide layer on the tungsten powders which increases the contact angle between the subsequent molten copper phase and the tungsten powders. The high cost of dedicated milling machines and the high hardness of tungsten make the introduction of contaminants an inevitable problem in the mechanical alloying process.

2.2.5. Introduction of copper by means of spontaneous infiltration

Several studies have been done with regards to infiltration mechanics. Early researchers used a bundle of capillary tubes to simulate a metal matrix during infiltration. While this presented a simple explanation to the infiltration process [73-75], this method has been recognised as being deficient in accuracy as it does not represent accurately a tungsten porous medium [76].

Monte carlo simulations have been presented by Shih *et al* to characterize the infiltration process in porous powder matrices, but the work was theoretical and was not properly verified with experimental data [77]. K. P. Trumble was able to derive explanations with regards to the infiltration of non cylindrical capillary systems [78]. In his research, Trumble used geometrical methods to derive a condition by which closely packed spheres were able to be infiltrated through their tetrahedral pores. Pores are classified by their interstitial orientations (Figure 2.6). He suggested a critical contact angle, θ_c=50.7° as the upper limit for spontaneous capillary infiltration for closely packed spheres. However to date, there has been no research done specific to the spontaneous infiltration of tungsten matrices by molten copper.

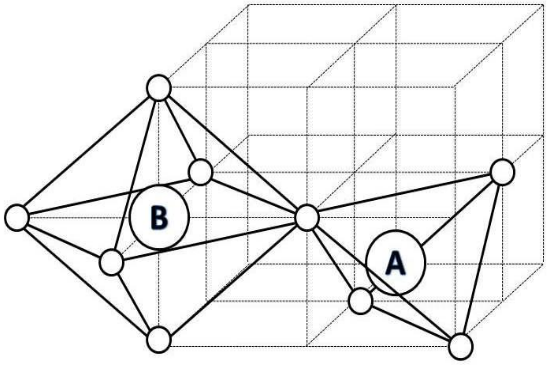

Figure 2.6: Diagram showing different interstatial sites.
B represents an octahedral site, while A represents a tetrahedral site.

2.3. Factors affecting tungsten copper MMCs

2.3.1. Grain size

Since its discovery, the Hall-Petch phenomenon has been extensively studied and it has been determined that within limits, smaller grain sizes in metals promote an increase in strength and hardness by means of grain boundaries impeding dislocation motion [79, 80]. This result was not only evident in steel but also in consolidated tungsten powders as well [81, 82]. As the strength of a metal matrix composite was determined by the strength of its constituent phases [83-85], increasing hardness and strength of the tungsten component of an MMC would strengthen the overall MMC. Studies have shown that hardness of porous tungsten matrices of 80% theoretical density has been determined to be in the region of 200-220 H_V [86]. Several methods in strengthening tungsten bodies by grain size refinement have been explored over the years. The common methods have been the variation of sintering parameters (sintering temperature and time), Zener additives and microwave sintering [87-89].

Studies with regards to the formation of sintered tungsten compacts have recorded grain sizes within the 2-4μm range [53, 82, and 90]. These samples were compacted with a variety of initial powder sizes and sintered in the range of 1000°C-1500°C.

With the processing of finer powders also comes the unwanted problem of abnormal grain growth [87-89, 91]. This phenomenon has been observed extensively in tungsten compacts sintered from tungsten powders [92]. Work by Straumal *et al* displayed exaggerated abnormal grain growth up to 11 times the initial powder size [93]. This was later verified by Kecskes *et al* with sizes up to 10 times their initial powder size [94]. In this work tungsten powders were sintered at 2000°C for periods ranging from 0.5 to 10.0 h. The results showed that with increasing sintering time, abnormal grains of as much as elevenfold the initial mean grains size was observed.

2.3.2. Processing parameters

Work by Kecskes *et al* [94] in the grain size control of Body Centred Cubic (BCC) metals has suggested that to produce fine grained tungsten, there is a need to reduce the sintering time, temperature, initial powder sizes and increase compaction pressure.

Given the insolubility of tungsten in liquid copper [95], the only way to produce submicron tungsten grain sizes is through the use of even smaller tungsten powders [96, 97]. Work done with regards to sintering submicron powders showed that regardless of starting powder sizes, tungsten grain sizes averaged at 2-5µm [82, 98, 99]. This tapering of grain sizes regardless of initial size suggests stability of tungsten at diameters of 2-5µm.

With the use of submicron and nanoscale powders comes the problem of abnormal grain growth. Smaller powders with their higher free surface to mass ratio have a greater driving force towards coarsening. This is also usually at the expense of surrounding grains [92], a feature that decreases a material's homogeneity.

From studies done on sintering kinetic equations [88], it was determined that an increase in sintering time and sintering temperature result in both coarsening and densification. These relationships can be seen in Figure 2.7 below. Sintering is essentially a material transport process with components of diffusion, viscous flow and evaporation-condensation. These components are all thermally activated with rates that increase with increased temperature and more discrete with extended periods of elevated temperatures.

The relationship in final and initial powder size has been theorized and can be expressed as:

$$D_{final}{}^{2} - D_{initial}^{2} = k_o t \exp\left(\frac{-Q}{RT}\right)$$

Where D_{final} and $D_{initial}$ are the final and initial grain size respectively, k_o is the equation constant, Q is the activation energy, T is the sintering temperature, t is the time and R is the universal gas constant [100].

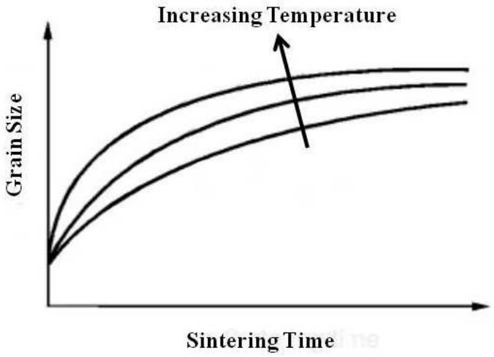

Figure 2.7: Graph showing relationship between grain size, sintering time and temperature.

It was also reported by Johnson *et al* [101] in 2005 that an increase in sintering temperature had a distinct effect on the densification of tungsten compacts sintered in liquid copper. In their study, temperatures varying from 900°C to 1500°C were used and it was noted that at temperatures exceeding the melting point of copper, greater shrinkage and a higher density were evident, likely due to the nature of the capillarity observed between adjacent tungsten particles caused by a copper liquid bridge.

Microwave sintering has also shown promise as an emerging field in metal powder sintering. Microwaves are electromagnetic waves that are able to oscillate atoms within a microwave opaque target body. While bulk metals tend to reflect the microwaves, powdered metals have been shown to be excellent absorbers of microwaves [102]. As a result of this internal heating, the temperature of powdered metals within a microwave environment increases more rapidly than conventional sintering processes [103]. This mode of heating is more efficient as energy is not lost through conduction/convection within the furnace. Extremely high heating rates that are ordinarily not possible with conventional heating methods [104-106] are possible with microwave sintering.

Studies done with regards to the microwave sintering of tungsten have been proven to be successful [107]. Further studies have also shown the possibility of sintering tungsten powders in as short as 20 minutes with grain sizes of as low as 0.5µm [108]. A study by Mondal *et al* [109] compared and contrasted the microwave and conventional sintering of tungsten copper (18.0wt%Cu) to 1300°C. The results are shown below.

Table 2.2: Comparison between microwave and conventional sintering on tungsten compacts.

	Microwave Sintering	Conventional Sintering
Vickers Hardness (H_V)	376	325
Average heating rates (°C/min)	15	5
Total heating profile time (min)	190	550
Tungsten Grain Sizes (µm)	2	4

It was evident that microwave sintering was able to reduce sintering profile time significantly (70%) and in the process reduce overall grain sizes and increased overall hardness. All samples were produced in a flowing hydrogen environment.

The major concern with microwave sintering would be the use of hydrogen as a flowing gas. Despite being widely regarded as a microwave absorber, densely agglomerated metal powders can behave as a reflector and lead to sparking. Tungsten powder itself is also known to be pyrophoric [110] in nature and can result in an explosion should sparking occur.

2.3.3. Oxide dispersion

One method in controlling grain growth during sintering is the addition of an incoherent phase that act to impinge grain boundaries [111, 112]. This process is known as Zener pinning. Zener pinning works by having a secondary incoherent particle at the grain boundary of two sintering grains. This secondary particle acts as a barrier to sintering and the pressure exerted by the particle counteracts the driving force of sintering between the two adjacent grains.

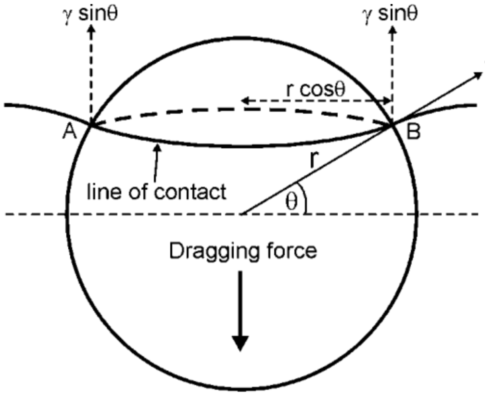

Figure 2.8: Zener pinning diagram with grain boundary and incoherent pinning particle of radius r. γ denotes boundary energy.

The total pinning force can be seen to act on the circumference by which the intersection of the boundary and particle occur. This circle has a radius of rcosθ and is denoted on Figure 2.8 above by a circle that intersects point A and B. The force per unit length acting along the diameter upwards is resolved to be γsinθ. The pinning force is resolved to be force per unit length acting in the direction of the dragging force against the boundary multiplied by the length of the circle for which the force acts.

$$F_{zener} = \text{Circumference of circle} \times \text{Force per unit length}$$

$$= 2\pi r\gamma\cos\theta\sin\theta$$

This has been shown to be successful in tungsten heavy metals where yttria was added to a tungsten-nickel-iron composition[113]. Work done in Japan by Itoh *et al* [114] also displayed grain size suppression with increased amounts of yttria addition. There was also growth displayed by both tungsten and yttria particles at higher sintering temperatures. It was shown that the strength of the pure tungsten sample sintered at 2037°C was greater than its yttria doped counterpart, although this trend was reversed at sintering temperatures of 2237°C and 2437°C.

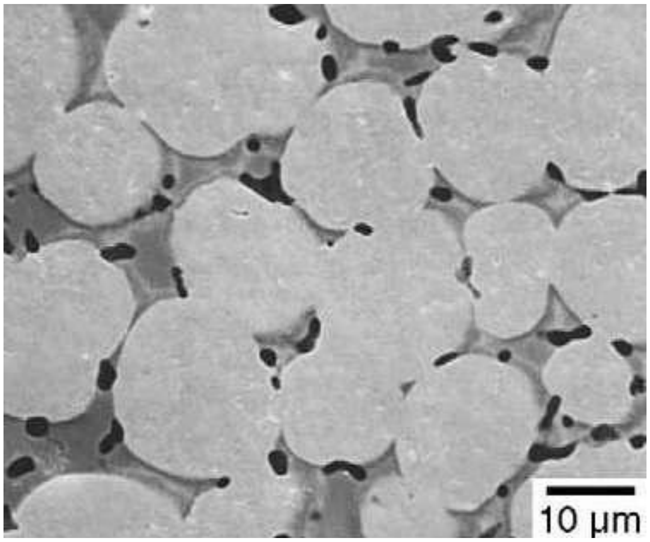

Figure 2.9 : Secondary Electron SEM image showing the effect of metal grain growth inhibition by an addition of a secondary oxide phase[113].

Studies have been done with both haffnia and yttria in microwave sintering environments [108, 115]. In these studies, tungsten grain sizes of ~0.5μm were achieved using the above mentioned oxide dopants. Particles used had a starting average size of 0.16μm. This was a reduction from the usual 2μm average grain sizes that were observed both in conventional as well as similar microwave sintering work [115].

No study however has been done using oxide dispersions in the manufacture of porous tungsten perform matrices. Infiltration of copper into a matrix of tungsten that contains oxide dispersions might prove difficult due to their low wetting characteristics [116]. Livey and Murray [117] attribute this to like repulsion of the electron cloud within a liquid metal and the anionic monolayer of ionic compounds.

The large contact angle molten copper displays on yttria surfaces [118] has been reported to be 130°. This non wetting characteristic of copper onto yttria is likely to act as a barrier for infiltration and will limit the amount of yttria that can be added to the tungsten as a grain growth inhibitor. An alternative to the system would be to include aluminium, which is said to reduce the contact angle from 130° to a mere 40°. However, the formation of copper-aluminium intermetallics is not desirable in the formation of tungsten copper MMCs. Many possible intermetallic combinations exist with variable physical, thermal and electrical properties which would inadvertently affect the quality and homogeneity of the resulting MMC [119].

2.3.4. Copper as a secondary phase

When considering the strength and properties of composites, it is essential to consider all phases within the composite as final properties are dependent on constituent phases [83].

Copper, although softer than tungsten, is essential as being the infiltrated phase within an open pore structure, it exerts a considerable effect on the properties of the MMC. The hardness of a die pressed porous copper matrix of 80% theoretical density has a value of approximately $250H_V$ [86].

While tungsten contributes to the low CTE and high hardness of the material, secondary phases like copper and silver are added to enhance the conductive properties of the finished material.

A reduction in conductivity and increase in hardness as compared to a law of mixtures result is due to strain hardening of the secondary, more conductive phase [120, 121]. This is caused by increased dislocations and grain boundaries which act as regions of electron scatter [80]. Copper, being of a face-centred cubic (FCC) lattice structure, allows for highly mobile gliding dislocations in one general direction. However tungsten, with a BCC structure is more prone to producing more dislocations due to the slipping of screw dislocations into several planes [122].

It has also been noted that for most cited literature and commercial product details, there has been a limit to the amount of copper that is commercially available [18, 19]. This value is due to the challenge within the industry of producing high copper composites with an acceptable degree of consistency.

One major problem in the addition of copper within the sample to enhance conductivity is due to secondary phase bleed out. The main reason for the bleed out is isothermal densification of tungsten at a temperature above the melting point of copper. This causes the interparticulate pores between tungsten grains to shrink, and squeezes previously infiltrated copper out from the surface of the MMC. This was observed in tungsten copper composites produced using the method described in U.S. Patent. 4,680,618 by Kurada *et al* [123, 124].

2.4. Suggested improvements

With this review it is clear that there are aspects within the field of tungsten copper MMCs that still have potential for research.

Improvements in the manufacturing and streamlining of the processes have been lacking with current commercially accepted methods. PIM offers a versatile alternative to die compaction in producing the MMCs. However, limited work has been done in studying the capabilities of PIM in the manufacture of MMC.

Secondly, while work has been done to control the grain size of tungsten compacts, there has been little or no work done in the study of controlling the grain sizes of porous tungsten compacts, and no work done in the study of how factors influencing grain growth would affect the subsequent infiltration of the matrix by copper. This is an avenue to be looked into as finer tungsten grains are likely to improve the properties of resulting MMCs. Factors like heating profiles, starting powder sizes and oxide dispersions are just some of the parameters that can be studied.

Finally, with copper being a finite resource, it is imperative that an alternative infiltrant metal be found. One suggestion is that of silver. While currently more costly, the inevitable rise in copper prices and silver's higher conductivity could make it a more cost efficient substitute to copper in the imminent future.

These issues highlighted here will be the focus of this dissertation and will be covered in detail within the following chapters.

References

1. Smithells, C., *A New Alloy of High Density.* Nature, 1937. **139**(3516): p. 490-491.

2. Jones, D. and P. Munnery, *Production of Tungsten alloy penetration radiation shields.* Powder Metallurgy, 1967. **10**: p. 156-173.
3. Kobayashi, S., N. Hosoda, and R. Takashima, *Tungsten alloys as radiation protection materials.* Nuclear Instruments and Methods in Physics Research-Section A Only, 1997. **390**(3): p. 426-430.
4. Prucher, B.P., *United States Patent 4,476,372, Spot welding electrode*, in *United States Patent and Trademark Office*. 1984.
5. Stone, C., et al., *United States Patent 3,909,581, Disposable Resistance Welding Electrode*, in *United States Patent and Trademark Office*. 1975.
6. Itoh, Y., M. Takahashi, and H. Takano, *Design of tungsten/copper graded composite for high heat flux components.* Fusion Engineering and Design, 1996. **31**(4): p. 279-289.
7. Ehlert, M.R. and E.R. Helderman, *United States Patent 4,788,627, Heat sink device using composite metal alloy*, in *United States Patent and Trademark Office*. 1988.
8. Jech, D. and J. Sepulveda. *Advanced copper-refractory metal matrix composites for packaging heat sink applications*. in *International Symposium on Microelectronics*. 1997. Philadelphia, USA: IMAPS.
9. Zweben, C., *Advances in composite materials for thermal management in electronic packaging.* JOM Journal of the Minerals, Metals and Materials Society, 1998. **50**(6): p. 47-51.

10. Watari, T. and H. Murano, *Packaging technology for the NEC SX supercomputer.* IEEE Transactions on Components, Hybrids, and Manufacturing Technology, 1985. **8**(4): p. 462-467.

11. Panichkina, V., M. Sirotyuk, and Y. Pilipovskii, *Effect of alloying on the properties of tungsten-copper pseudoalloys.* Powder Metallurgy and Metal Ceramics, 1985. **24**(7): p. 540-542.

12. Sebastian, K., *Properties of sintered and infiltrated tungsten-copper electrical contact material.* International Journal of Powder Metallurgy, 1981. **17**: p. 297-303.

13. Sampath, A., et al., *Enhancing the thermal properties of W/Co composites.* Powder Metallurgy, 2001. **44**(4): p. 313-316.

14. Challita, A., B. Chelluri, and D.P. Bauer, *Minimizing Non-arcing Contact Material Deposition on Rails.* IEEE Transactions on Magnetics, 1995. **31**(1): p. 134-137.

15. Nicholas, M. and D. Poole, *The influence of oxygen on wetting and bonding in the copper-tungsten system.* Journal of Materials Science, 1967. **2**(3): p. 269-274.

16. Provenzano, V. and M. Imam, *Ultrafine superstrength materials.* Nanostructured Materials(UK), 1992. **1**(1): p. 89-94.

17. Sampath, A., et al., *Enhancing thermal properties of W/Cu composites* Powder Metallurgy, 2001. **44**(4): p. 313-6.

18. *Your one source for parts made with the composites: Molydbdenum-Copper, Tungsten-Copper*. 2005, Ameteck Speacialty Metal Products.

19. *Technical Data - Tungsten/Copper - Moly/Copper - Cu/Mo/Cu Heat Sink Materials* in *Marketech International, Inc.* . 2006.

20. Lassner, E. and W. Schubert, *Tungsten: Properties, chemistry, technology of the element, alloys, and chemical compounds*. 1999: Plenum Publishing Corporation.

21. Turrell, K., *Tungsten*. 2004: Benchmark Books.

22. Edelstein, D., *Copper: Minerals yearbook minerals yearbook*. Vol. 1. 2008, Reston, VA: US Geological Survey, Department of Interior.

23. Shedd, K., *Tungsten: Minerals yearbook minerals yearbook*. Vol. 1. 2008, Reston, VA: US Geological Survey, Department of Interior.

24. Harris, P. and D. Humphreys, *Tungsten: A review.* The Institution of Mining and Metallurgy, 1983: p. 42.

25. Bhosale, S., S. Mookherjee, and R. Pardeshi, *Current practices in tungsten extraction and recovery.* High-temperature materials and processes, 1990. **9**(2-4): p. 147-162.

26. Kieffer, B. and E. Lassner, *Tungsten Recycling in Todays Environment.* BHM Berg- und Hüttenmännische Monatshefte, 1994. **139**: p. 340-340.

27. Smith, G., *Materials flow of tungsten in the United States*. 1994, United States Department of the Interior, Bureau of Mines.

28. Gockmann, K., *Recycling of copper.* Canadian Mining and Metallurgical Bulletin, 1992. **85**(958): p. 150-154.

29. Bertram, M., et al., *The contemporary European copper cycle: waste management subsystem.* Ecological Economics, 2002. **42**(1-2): p. 43-57.

30. Zeltner, C., et al., *Sustainable metal management exemplified by copper in the USA.* Regional environmental change, 1999. **1**(1): p. 31-46.

31. Gordon, R., M. Bertram, and T. Graedel, *Metal stocks and sustainability.* Proceedings of the National Academy of Sciences, 2006. **103**(5): p. 1209-1214.

32. Lifset, R., et al., *Where has all the copper gone: The stocks and flows project, part 1.* JOM Journal of the Minerals, Metals and Materials Society, 2002. **54**(10): p. 21-26.

33. Graedel, T., et al., *Multilevel cycle of anthropogenic copper.* Environ. Sci. Technol, 2004. **38**(4): p. 1242-1252.

34. Kapur, A., et al., *The contemporary copper cycle of Asia.* Journal of Material Cycles and Waste Management, 2003. **5**(2): p. 143-156.

35. Hubbert, M., *Nuclear energy and the fossil fuels*. 1956: Shell Development Co., Exploration and Production Research Division.

36. Suflis, S., *Scenarios for a large scale installation of compact fluorescent lamps: influence on the power quality.* WSEAS Transactions on Circuits and Systems, 2004. **3**(5): p. 1386-1391.

37. Cook, B., *High efficiency lighting in industry and commercial buildings.* Power Engineering, 1998. **12**(5): p. 197-206.

38. Kumar, S., V. Bai, and T. Rajasekharan, *Aluminium matrix composites by pressureless infiltration: the metallurgical and physical properties.* Journal of Physics D: Applied Physics, 2008. **41**(10): p. 105403.

39. Aghajanian, M., et al., *The fabrication of metal matrix composites by a pressureless infiltration technique.* Journal of Materials Science, 1991. **26**(2): p. 447-454.

40. Yoo, M.K., et al., *United States Patent 5,963,773 ,Tungsten skeleton structure fabrication method employed in application of copper infiltration and tungsten-copper composite material fabrication method thereof* in *United States Patent and Trademark Office*. 1999.

41. Dorfman, L.P., et al., *United States Patent 5,956,560, Tungsten-copper composite powderfabrication method thereof* in *United States Patent and Trademark Office*. 1999.

42. Matejczyk, D.E., *United States Patent 4,710,223 ,Infiltrated sintered articles* in *United States Patent and Trademark Office*. 1987.

43. Wang, W.S. and K.S. Hwang, *The Effect of Tungsten Particle Size on the Processing and Properties of Infiltrated W-Cu Compacts.* Metallurgical and Materials Transactions A, 1998. **29A**: p. 1509-1516.

44. German, R., *Powder Injection Molding: Design and Applications*. 2003: Innovative Material Solutions.

45. German, R.M. and A. Bose, *Injection Molding of Metals and Ceramics*. 1997, New Jersey: Metal Powder Industries Federation.

46. Fleischer, J., C. Buchholz, and H. Weule, *Automation of the Powder-Injection-Moulding Process for Micro-Mechanical Parts.* CIRP Annals-Manufacturing Technology, 2003. **52**(1): p. 419-422.

47. Fleischer, J. and A. Dieckmann, *Automation of the powder injection molding process.* Microsystem Technologies, 2006. **12**(7): p. 702-706.

48. Vervoort, P., R. Vetter, and J. Duszczyk, *Overview of powder injection molding.* Advanced Performance Materials, 1996. **3**(2): p. 121-151.

49. Dechavanne, J., *United States Patent 4,165,959, Apparatus for injection-moulding several moulding materials onto one another* in *United States Patent and Trademark Office*. 1978.

50. Hahn, J., et al., *United States Patent 7,393,199, Multi-shot injection molding arrangement*, in *United States Patent and Trademark Office*. 2008.

51. Goodship, V., *Arburg Practical Guide to Injection Moulding*. 2004: Rapra Technology.

52. Taoka, F., N. Tanno, and H. Watanabe, *United States Patent 4,315,724, Process and machine for multi-color injection molding*, in *United States Patent and Trademark Office*. 1982.

53. Ho, P.W., Q.F. Li, and J.Y.H. Fuh, *Evaluation of W–Cu metal matrix composites produced by powder injection molding and liquid infiltration* Materials Science and Engineering: A, 2007. **485**(1-2): p. 657-663

54. Hwang, K.S. and Y.M. Hsieh, *Comparative Study of Pore Structure Evolution During Solvent and Thermal Debinding of Powder Injection Molded Parts.* Metallurgical and materials transactions A, 1996. **27A**: p. 245-253.

55. German, R., *Powder Injection Molding in North America–Upbeat Again.* Powder Injection Moulding International, 2007. **1**(3): p. 25-31.

56. Ye, H., X. Liu, and H. Hong, *Fabrication of metal matrix composites by metal injection molding—A review.* Journal of Materials Processing Tech., 2008. **200**(1-3): p. 12-24.

57. Moxson, V. and F. Froes, *Fabricating sports equipment components via powder metallurgy.* JOM Journal of the Minerals, Metals and Materials Society, 2001. **53**(4): p. 39-41.

58. Belhadjhamida, A. and R. German, *Tungsten and Tungsten Alloys by Powder Metallurgy--a Status Review.* 1991.

59. Kim, J., et al., *Densification behavior of mechanically alloyed W-Cu composite powders by the double rearrangement process.* Scripta Materialia, 1998. **39**(6): p. 669-676.

60. Moon, I., *Metal injection moulding of nano-structured tungsten-copper powders.* Metal Powder Report, 2001. **56**(2): p. 36-36.

61. Maneshian, M., A. Simchi, and Z. Hesabi, *Structural changes during synthesizing of nanostructured W–20wt% Cu composite powder by mechanical alloying.* Materials Science & Engineering A, 2007. **445**: p. 86-93.

62. Kim, S., M. Suk, and Y. Kim, *Metal Injection Molding of W-Cu Powders Prepared by Low Energy Ball Milling.* Metals and Materials International, 2006. **12**(1): p. 39-44.

63. Jedamzik, R., A. Neubrand, and J. Rödel, *Functionally graded materials by electrochemical processing and infiltration: application to tungsten/copper composites.* Journal of Materials Science, 2000. **35**(2): p. 477-486.

64. Lezanski, J., *Space filling of the capillaries during spontaneous infiltration in a gas atmosphere.* Rudy i Metale Niezelazne, 2004. **49**(8): p. 407-411.

65. Dorfman, L., D. Houck, and M. Scheithauer, *Consolidation of tungsten-coated copper composite powder.* Journal of Materials Research, 2002. **17**(8): p. 2075-2084.

66. Raghu, T., et al., *Synthesis of nanocrystalline copper–tungsten alloys by mechanical alloying.* Materials Science & Engineering A, 2001. **304**: p. 438-441.

67. Kim, J. and I. Moon, *Sintering of nanostructured W-Cu alloys prepared by mechanical alloying.* Nanostructured Materials, 1998. **10**(2): p. 283-290.

68. Kim, J., et al., *Metal injection molding of nanostructured W-Cu composite powder.* International Journal of Powder Metallurgy(USA), 1999. **35**(4): p. 47-50.

69. Hong, S. and B. Kim, *Fabrication of W–20 wt% Cu composite nanopowder and sintered alloy with high thermal conductivity.* Materials Letters, 2003. **57**(18): p. 2761-2767.

70. Houck, D.L., et al., *United States Patent 5,439,638, Method of making flowable tungsten/copper composite powder*, in *United States Patent and Trademark Office*. 1993.

71. Dorfman, L.P., et al., *United States Patent 6,103,392, Tungsten-copper composite powder,* in *United States Patent and Trademark Office*. 2000.

72. Koch, C., *Synthesis of nanostructured materials by mechanical milling: problems and opportunities.* Nanostructured Materials, 1997. **9**(1-8): p. 13-22.

73. Martins, G., D. Olson, and G. Edwards, *Modeling of infiltration kinetics for liquid metal processing of composites.* Metallurgical and Materials Transactions B, 1988. **19**(1): p. 95-101.

74. Semlak, K. and F. Rhines, *The rate of infiltration of metals.* Trans. Metall. Soc. AIME, 1958. **212**(June).

75. Ligenza, J. and R. Bernstein, *The Rate of Rise of Liquids in Fine Vertical Capillaries.* J. Am. Chem. Soc, 1951. **73**(10): p. 4636-4638.

76. Panichkina, V., V. Skorokhod, and N. Pavlenko, *Porous structure of sintered tungsten.* Powder Metallurgy and Metal Ceramics, 1977. **16**(12): p. 950-951.

77. Shih, M. and L. Hourng, *Numerical simulation of capillary-induced flow in a powder-embedded porous matrix.* Advanced Powder Technology, 2001. **12**(4): p. 457-480.

78. Trumble, K., *Spontaneous infiltration of non-cylindrical porosity: Close-packed spheres.* Acta Materialia, 1998. **46**(7): p. 2363-2367.

79. Hughes, G., et al., *Hall-petch strengthening for the microhardness of twelve nanometer grain diameter electrodeposited nickel.* Scripta Metallurgica, 1986. **20**(1): p. 93-97.

80. Callister, W.D., *Fundamentals of Materials Science and Engineering: An Integrated Approach*. 2nd ed. 2004: Wiley.

81. Vashi, U., R. Armstrong, and G. Zima, *The hardness and grain size of consolidated fine tungsten powder.* Metallurgical and Materials Transactions B, 1970. **1**(6): p. 1769-1771.

82. German, R.M., et al., *Processing model for tungsten powders and extension to nanoscale size range.* Powder Metallurgy, 2006. **49**(19-27).

83. Fan, Z., P. Tsakiropoulos, and A. Miodownik, *A generalized law of mixtures.* Journal of Materials Science, 1994. **29**(1): p. 141-150.

84. McDanels, D., et al., *Analysis of Stress-Rupture and Creep Properties of Tungsten-Fiber-Reinforced Copper Composites*. 1967: National Aeronautics and Space Administration; For sale by the Clearinghouse for Federal Scientific and Technical Information.

85. Cooper, G., *The structure and mechanical properties of composite materials.* Reviews of Physics in Technology, 1971. **2**(2): p. 49-91.

86. Selcuk, C., et al., *Microhardness as a measure of homogeneity of porous tungsten.* Materials Letters, 2004. **58**(12-13): p. 1873-1876.

87. German, R.M., *Sintering Theory and Practice*. 1996: Wiley.

88. Kang, S.J.L., *Sintering: Densification, Grain Growth, and Microstructure*. 2005: Butterworth-Heinemann.

89. Rahaman, M.N., *Ceramic Processing and Sintering*. 2nd ed. 2003: CRC Press.

90. Jain, M., et al., *Microwave Sintering: A New Approach to Fine-Grain Tungsten-I.* International Journal of Powder Metallurgy, 2006. **42**(2): p. 45-52.

91. Jo, W., D. Kim, and N. Hwang, *Effect of interface structure on the microstructural evolution of ceramics.* Journal of the American Ceramic Society, 2006. **89**(8): p. 2369-2380.

92. Briant, C., F. Zaverl, and W. Carter, *The effect of deformation on abnormal grain growth in tungsten ingots.* Acta Metallurgica et Materialia, 1994. **42**(8): p. 2811-2822.

93. Straumal, B., et al. *Normal and abnormal grain growth in tungsten polycrystals*: Trans Tech Publications.

94. Kecskes, L., et al., *Grain size engineering of bcc refractory metals: Top-down and bottom-up—Application to tungsten.* Materials Science & Engineering A, 2007. **467**(1-2): p. 33-43.

95. Johnson, J. and R. German, *Solid-State Sintering in the Presence of a Liquid Phase.* Sintering Technology, 1996: p. 237.

96. Kothari, N., *Effects of particle size on the sintering kinetics in tungsten powder.* Powder Metall, 1964. **7**: p. 251-60.

97. Kothari, N., *Sintering kinetics in tungsten powder.* J. Less-Common Metals, 1963. **5**(2): p. 140-150.

98. Qu, X., J. Fan, and B. Huang. *Sintering of injection molded nano-structured tungsten heavy alloy powder compacts*. 2000.

99. Qu, X. and J. Fan, *Powder injection molding and solid-state sintering of nano-crystalline tungsten heavy alloy.* Chinese Journal of Materials Research(China), 2001. **15**(1): p. 130-134.

100. Beck, P., et al., *Grain growth in high-purity aluminum and in an aluminum-magnesium alloy.* Metals Technol., 1947. **14**(6): p. 23.

101. Johnson, J., J. Brezovsky, and R. German, *Effects of tungsten particle size and copper content on densification of liquid-phase-sintered W-Cu.* Metallurgical and materials transactions A, 2005. **36**(10): p. 2807-2814.

102. Roy, R., D. Agrawal, and J. Cheng, *United States Patent 6,183,689, Process for sintering powder metal components*, in *United States Patent and Trademark Office*. 2001.

103. Agrawal, D., *Microwave Sintering Of Ceramics, Composites, Metals, And Transparent Materials.* Journal of Materials Education, 1997. **19**: p. 49-58.

104. Clark, D. and W. Sutton, *Microwave processing of materials.* Annual Review of Materials Science, 1996. **26**(1): p. 299-331.

105. Haque, K., *Microwave energy for mineral treatment processes—a brief review*. International Journal of Mineral Processing, 1999. **57**(1): p. 1-24.

106. Adam, D., *Microwave chemistry: Out of the kitchen.* Nature, 2003. **421**(6923): p. 571-572.

107. Prabhu, G., A. Chakraborty, and B. Sarma, *Microwave sintering of tungsten.* International Journal of Refractory Metals and Hard Materials, 2008.

108. Dinesh, A., et al. *Microwave sintering of tungsten and its alloys*. in *8th International Conference on the Science of Hard Materials*. 2004. San Juan, Puerto Rico.

109. Avijit, M., U. Anish, and A. Dinesh. *Sintering Advances in Consolidating W Based Alloys*. in *Proceedings of the 1st Global Congress on Microwave Energy Applications*. 2008. Japan.

110. Sliwa, A., *Pyrophoric properties of metal powders and dusts.* Rudy Metale Niezelazne, 1971. **16**(11): p. 559-564.

111. Doherty, R.D., *Current issues in recrystallization: a review.* Materials Science and Engineering: A, 1997. **238**(2): p. 219-274.

112. Couturier, G., et al., *3D finite element simulation of the inhibition of normal grain growth by particles.* Acta Materialia, 2005. **53**(4): p. 977-989.

113. Ryu, H.J. and S.H. Hong, *Fabrication and properties of mechanically alloyed oxide-dispersed tungsten heavy alloys.* Materials Science and Engineering A, 2003. **363**: p. 179-184.

114. Itoh, Y. and Y. Ishiwata, *Strength properties of yttrium-oxide-dispersed tungsten alloy*. JSME international journal. Series A, Solid mechanics and material engineering. **39**.

115. Jain, M., et al., *Microwave Sintering: A New Approach to Fine-Grain Tungsten-II.* International Journal of Powder Metallurgy, 2006. **42**(2): p. 53-57.

116. Naidich, J., V. Zhuravljov, and N. Frumina, *Wetting of rare-earth element oxides by metallic melts.* Journal of Materials Science, 1990. **25**(4): p. 1895-1901.

117. Livey, D. and P. Murray, *Wetting Properties of Solid Oxides and Carbides by Liquid Metals*. 1956, AERE-M/R--1746, Atomic Energy Research Establishment, Harwell (England).

118. Barzilai, S., et al., *Interface phenomena in the Y2O3/(Al–Cu) system.* Materials Science & Engineering A, 2006. **420**(1-2): p. 291-295.

119. Braunovic, M. and N. Alexandrov, *Intermetallic compounds at aluminum-to-copper electricalinterfaces: effect of temperature and electric current.* IEEE

Transactions on Components, Packaging, and Manufacturing Technology, Part A, 1994. **17**(1): p. 78-85.

120. Everett, R. and R. Arsenault, *Metal matrix composites: processing and interfaces.* Academic Press, Inc, 1250 Sixth Ave, San Diego, California 92101, USA, 1991. 228, 1991.

121. Everett, R. and R. Arsenault, *Metal matrix composites: mechanisms and properties.* Academic Press, Inc, 1250 Sixth Ave, San Diego, California 92101, USA, 1991. 415, 1991.

122. Greer, J., C. Weinberger, and W. Cai, *Comparing the strength of fcc and bcc sub-micrometer pillars: Compression experiments and dislocation dynamics simulations.* Materials Science & Engineering A, 2008. **493**(1-2): p. 21-25.

123. Kuroda, T. and K. Kumazawa, *United States Patent 4,680,618 , Package comprising a composite metal body brought into contact with a ceramic member*, in *United States Patent and Trademark Office*. 1983.

124. Polese, F.J., *United States Patent 5,878,322, Heat-dissipating substrate for micro-electronic devices and fabrication method*, in *United States Patent and Trademark Office*. 1997.

3. EXPERIMENTAL STUDY

The aims of this study were to develop economical processing methods to manufacture tungsten based MMCs and also study the microstructure and properties of the produced MMCs.

The broad layout of the experiment is shown clearly in the schematic chart below.

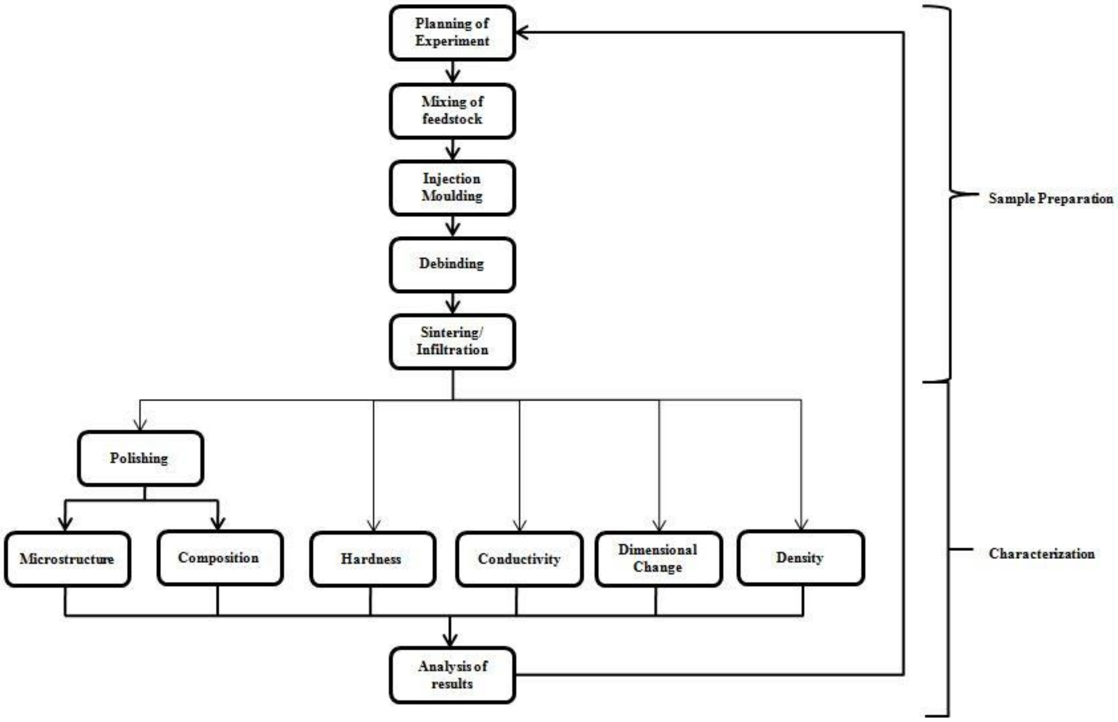

Figure 3.1: Schematic diagram showing the sample preparation and the characterization processes

3.1. Sample process overview

In this study, the steps involved in chronological order are; the initial planning, feedstock preparation, injection moulding, debinding of the moulded part and finally a combined sintering and infiltration step where the tungsten-copper MMC is produced.

3.1.1. Planning of sample preparation

The careful planning of the samples to be manufactured is essential as this determines the processing variables to be modified. Adjustments to variables are based on data collected from tests conducted on samples manufactured previously. The overall aim is to achieve more desirable microstructural properties.

The variables in this study were the materials used for the feedstock, the solid volume loading of the feedstock, the starting powder, the heating profile, the furnace atmosphere, the sintering/infiltrating temperature and the sintering/infiltrating dwell time.

The ratio of thermoplastic polymer against solid powder affects the final properties of the tungsten matrix and the ease of injection moulding. Binder deficit will make the feedstock hard to inject as the binder serves to lower the viscosity of the melt during injection moulding by acting as an interparticulate lubricant (Figure 3.2).

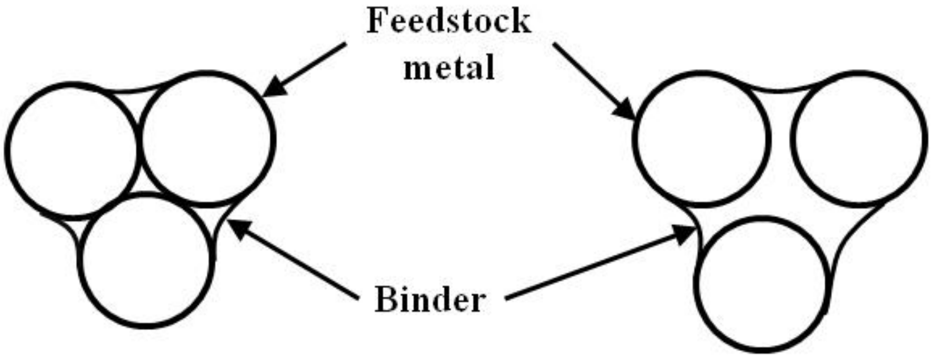

(i) (ii)

Figure 3.2: Picture showing the interaction between polymer binder and feedstock metal with (i) insufficient polymer leading to contact between particles and (ii), excess binder allowing for the lubrication of the adjacent particles. While increase in binder concentrations result in smoother injection moulding, excessive binder amounts will lead to collapse of the moulded green part upon debinding. This is known as the critical solid loading concept.

Excessive binder addition will cause collapse of the powdered compact during debinding as the solid powders are not drawn close enough to maintain structural integrity upon debinding. Excessive binders will also lead to flashing (material wastage) and inhomogeneity within the final injection moulded component. It is important to note that in this process, a porous metal compact is desirable as the pores present serve as conduits by which the liquid metal infiltrant will later occupy. Hence the amount of polymer added must be carefully determined and be sufficient to produce porosity, but not excessive to the point where structural integrity and homogeneity of the MMC are compromised.

In two material PIM where two feedstocks are overmoulded in a special die, solid loading of the feedstocks play a very important role. Unlike the overmoulding of polymeric components, the removal of binder in stages for PIM green parts result in differential shrinkage between both materials and dimensional mismatches. Such problems of distortion can be addressed in product design (e.g. increasing the moment of inertia of the component by the addition of ribs to prevent bending) but should nonetheless be carefully minimized with the careful planning of polymer contents within the relevant feedstocks to reduce shrinkage variations.

Materials chosen for feedstock formulation affect directly the composition of the final MMC. Tungsten is invariant throughout the entire study while copper and silver are both used as the secondary infiltrating metal. The choice of the secondary infiltrating metal determines the lowest temperature by which the tungsten matrix can be sintered. The presence of additives introduced into the tungsten feedstock affects the final dimensional properties of the tungsten matrix. The addition of ceramic additives has been shown [1] to constrain the growth of tungsten particles subjected to sintering. The presence of such additives can also affect the overall wetting characteristics of the tungsten matrix by an infiltrating metal [2].

To achieve a designated tungsten grain size within the final MMC, starting tungsten powders have to be finer than the target grain size. This is to allow for grain growth and densification which will occur during sintering [3]. There has been no recorded dissolution of tungsten into molten copper or silver (in the absence of nickel) and hence no necessity to expect a significant reduction in tungsten particle sizes during liquid phase sintering.

This study focused mainly on the changes associated with the integration of the thermal debinding process into the sintering/infiltration heat cycle as a means of reducing process time. The effect of solvent debinding on tungsten compacts has been studied previously by Hwang *et al* [4] and was not covered in the scope of this study.

As the sample set up consists of two layers (high and low melting point components), there is therefore an option to vary the orientation by which moulded samples were placed inside the furnace during sintering. The different orientations of the layers determine the final density and microstructure of the sample as gravity can act as either a supplementary driving force or an unexpected obstacle.

The heating profile in which the samples are subjected to is by far the most critical among all the variables. The infiltration/sintering temperature and holding time determines the final structure of the tungsten matrix, with a minimum temperature required to melt the infiltrant metal phase. The heating and cooling rates also determine the stress levels between the two interweaving matrices and also affect grain growth characteristics of tungsten.

Sintering atmospheres have an influence on both the tungsten and infiltrant phases. Oxides of tungsten are known to be volatile at high temperatures [5] and oxides in general are reported to display low wetting characteristics when subjected to liquid metals of copper and silver [2]. Hydrogen is also known to be soluble in several molten metals [6, 7] with diatomic hydrogen gas being evolved during the solidification process to produce smooth, rounded pores.

3.1.2. Feedstock preparation

Feedstock mixing is the process by which metal powders are admixed with relevant polymeric binders. The metal powders, thermoplastic polymer binders and dopant powders (where applicable) were first carefully measured using a Precisa 40SM-200A and put into sealed receptacles. It is important to note that finely divided metals, specifically tungsten, are known to be pyrophoric in nature and care has to be taken that they are not exposed to sparking or an open flame.

The three main metal powders used in this study were 10µm copper, 1µm tungsten and 100nm tungsten powder (morphology is shown in Figure 3.3 below).

Polymeric binders used in this study consisted of three main components namely a backbone polymer that provided the bulk of the strength for the moulded component, a binder soluble in organic solvents that was to be removed in the first stage of debinding (solvent debinding) and finally a surfactant that allowed the backbone and soluble binder to bond with the metal and ceramic powders in use [8]. In this study, a standard polymer mixture consisting of polypropylene as the backbone polymer, stearic acid as the surfactant and paraffin wax as the soluble component of the binder was used.

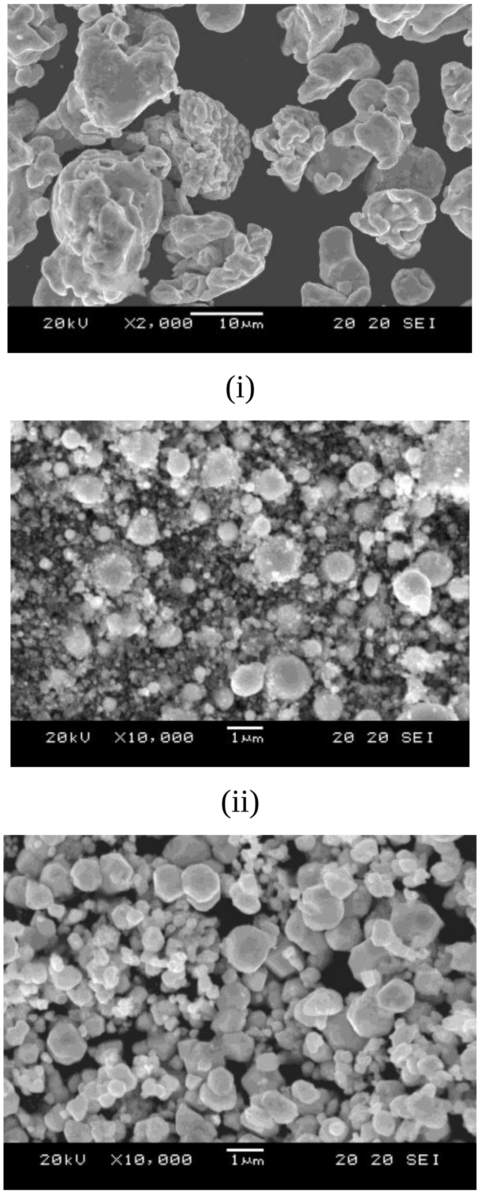

(i)

(ii)

(iii)

Figure 3.3: SEM photos showing morphology of the metal powders (i) 10μm copper powder, (ii) 100nm tungsten powders (with distinct agglomeration) and (iii) 1μm tungsten powder.

The tungsten, silver and copper feedstocks were prepared separately with their respective polymeric binders. This was done in a Ross double planetary mixer (Figure 3.4).

Figure 3.4: Photo of the Ross planetary mixer used in the mixing process

In the mixing process, the mixer was first heated to 80°C with polymers (amounting to 50% volume of the final mix) present within the crucible. Upon melting, a tablespoon of the metal powder was then added. The double planetary mixer was then closed and left to rotate at 60 revolutions per minute for 10 minutes. After 10 minutes, the resulting slurry was then examined visually for homogeneity. If this was deemed satisfactory, more power was added, if not it would be mixed until it was homogenous. This step was done until all the metal powder had been introduced into the mixing crucible. When all the powder and polymer was added to the mixer and the mixture was deemed to be homogenous, the temperature was then raised to 175°C and the mixer was evacuated to extract air. This was done to lower the viscosity of the mix to facilitate more uniform mixing while reducing the amount of trapped air. The resulting slurry is mixed for a total of four hours, with a change in rotating direction every hour. A slurry with consistency similar to toothpaste results. This was a rheological indicator that the feedstock could be injection moulded with ease at 175°C. After the cycle was complete, the slurry was removed, cooled and crushed manually to produce feedstock pellets small enough to be fed into the barrels of the respective PIM machines. The same general process was executed in the production of all feedstocks for PIM in this study.

3.1.3. Injection moulding

During the course of this project, PIM was done in three different machines, namely the Arburg Allrounder 220s, the Arburg Allrounder 420C (with two barrels capable of multi shot injection moulding) and the Battenfeld Microsystem 50 Micro injection moulding machine (Figure 3.5 below).

(i)

(ii)

(iii)

Figure 3.5: Photos of PIM machines. From Top left corner (i) the Arburg Allrounder420C capable of Multi-shot injection moulding, (ii) the Battenfeld Microsystem 50 micro injection moulding machine (iii) the Arburg Allrounder 220S injection moulding machine

The injection moulding machine consists of several components. The main components are a hopper which directs the feedstock into the barrel, a barrel and screw assembly that is coated with carbide to ensure a longer service lifespan, and a mould with cooling channels and ejector pins. All these components are controlled through a central computer custom built into the PIM machine.

The heated barrel (at a temperature of 165°C) melts the polymer present within the feedstock and reduces the melts overall viscosity. The screw within the barrel rotates to soften the feedstock further and also serves to homogenize the melted softened feedstock through shear. The flight depth of the screw gets progressively narrower towards the tip and this facilitates the removal of trapped gases through compression. The compressed feedstock is brought into the region in front of the screw tip behind the nozzle of the barrel. The feedstock accumulated in this region is called the shot, and it is filled when feedstock begins to “drool” from the barrel nozzle. The process of filling the shot in this region is termed as metering and the shot volume is determined by the actual volume of the component and its associated sprues and runners.

When sufficient material is accumulated behind the nozzle, the barrel is forced towards the runner inlet of a closed die. This forms a seal and the screw is forced forward, closing a check ring at the nozzle tip (that serves as a no return valve) that expels the feedstock into the mould at a high pressure and velocity to fill the cavity.

Within the mould, the feedstock is cooled by means of custom built cooling channels that remove heat from the feedstock. This removal of heat solidifies the feedstock. When the feedstock has solidified, the die is parted and the part is ejected onto a cushioned platform by means of ejector pins.

One unique feature of this study is the inclusion of two-material PIM into some of the processes investigated. There are several methods of multi-injection moulding, but the method used in this study is specifically over moulding where a portion of a previously injection moulded component (known as an insert) is put back into a larger die and a second shot of a second material is injected over, forming a two-material moulded part (Figure 3.6). In all experiments, tungsten was the insert material.

(i) (ii)

Figure 3.6: Photos showing overmoulded tensile bars, (i) Micro tensile bar with two halves made from copper and tungsten, (ii) Micro tensile dual layer bimetallic bar made from copper and tungsten.

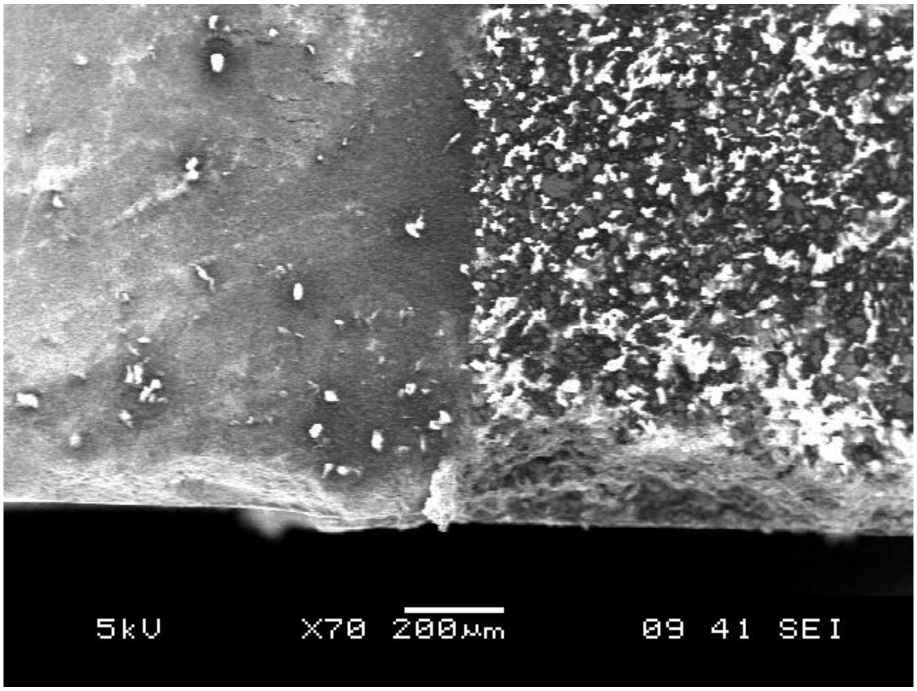

Figure 3.7: SEM micrograph of a two material joining interface of a green part. The left half is of 100nm tungsten powders while the right half is of 10µm copper powders. Darker regions are metals while the lighter white regions are polymeric regions.

Overmoulding is the fundamental system involved in the injection of parts that consist of two materials. Material combinations that can be successfully implemented using the over moulding method can be transferred to other more complex multi material moulding methods with relative ease. These methods include co-injection moulding, multi shot injection moulding, insert moulding, lamellar injection moulding and multi component injection moulding [9, 10].

Bimetallic tensile bars of tungsten and its infiltrant metal reduce material wastage as fixed amounts of the infiltrant metals can be controlled through the formulation of feedstock to minimize excess. Handling and setting of the moulded sample is also simplified as only one component (the bimetallic component) is handled. Conventional methods require the handling of both a tungsten component as well as a separate infiltrant metal component.

Micro tensile bars were moulded in the Battenfeld Microsystem 50 micro injection moulding machine. Macro tensile bars and the diagnostic component were moulded in the Arburg Allrounder 220S injection moulding machine while rectangular bars were moulded in the Arburg Allrounder420C injection moulding machine.

3.1.4. Debinding

Following injection moulding, the polymeric binders were removed from the moulded component before sintering. This is done in two stages; the solvent and thermal debinding phases.

In the first phase, known as solvent debinding, moulded components were put into a solution of heptane for four hours at a temperature of 50°C. For the sake of safety, a Memmeret heated water bath (Figure 3.8 below) was used as many organic solvents are flammable and not suitable to be heated over an open flame.

Figure 3.8: The Memmeret WNB 45 waterbath used in the solvent debinding process.

During the solvent debinding process, paraffin wax that is soluble in the abovementioned organic solvent is dissolved into the heated bath, leaving behind only the backbone and surfactant polymers within the component. The voids left within the moulded sample act as conduits by which the remaining polymers flow out from. This has been shown to reduce considerably both the time required for the debinding process and the amount of distortion subjected to the debinded part [4, 11].

Following solvent debinding, the solvent debinded samples were placed on a ceramic plate and put inside a furnace and heated to 450°C at a rate of 3°/minute under hydrogen. This temperature was held for a period of one to two hours depending on the heating profile and was done in a CM horizontal tube furnace (Figure 3.9 below).

Figure 3.9: A standard CM horizontal tube furnace

Thermal debinding decomposes the remaining polymers into vapours that flow out through the conduits left behind by the soluble binders. In the initial phases of the study, thermal debinding was done as a standalone heating profile. This meant that following the 450°C heating, the sample was subsequently heated to a further 700°C, known as presintering, and then cooled to room temperature. This additional ramp up was to ensure that there was a degree of sinter bonding between adjacent powder particles such that the debinded part possessed sufficient green strength to withstand the shear and adhesive forces that were to come later in the infiltration phase.

Heating profiles conceived later in the study integrated thermal debinding and sintering/infiltration into one heating profile, i.e. after thermal debinding at 450°C (see Figure 3.10), the furnace was immediately heated up to the sintering/infiltration temperature. This was more effective as it resulted in overall time savings and also a savings on costly hydrogen gas. Heating profiles of this nature are referred to as direct sintering in this thesis.

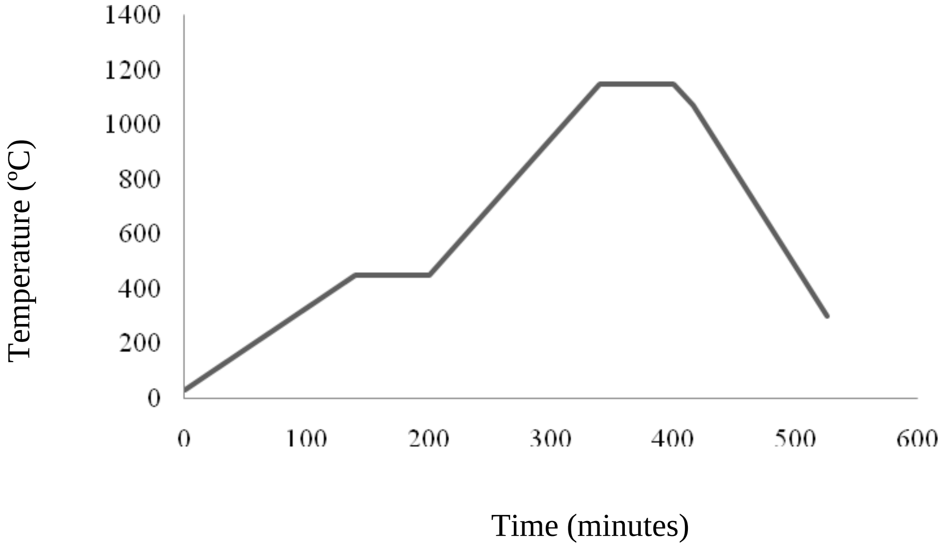

Figure 3.10: An integrated thermal debinding and sintering/infiltration heating profile. In this integrated profile, the furnace is heated to 450°C at a rate of 3°C/min and held at 450°C for one hour. It is then heated to the sintering/infiltrating temperature of 1150°C at a rate of 5°C/min and held for another one hour. Finally the temperature is lowered to 300°C at a rate of 3°C/min and subsequently left to cool naturally to room temperature.

3.1.5. Sintering/Infiltration

Sintering and infiltration was done concurrently and to facilitate this, only temperatures above the melting point of the infiltrant metal were chosen. The lowest temperatures chosen for copper was 1150°C and not lower to give allowances for a slight deviation of heat distribution within the tube furnace. Sintering/infiltration were done in the same CM horizontal tube furnace that was used in the thermal debinding process.

In the initial phases, various atmospheres were tested. The atmospheres were vacuum (700Pa), reducing and an inert environment. The gases used for the latter two were hydrogen and nitrogen respectively.

Orientations of the infiltrant piece with respect to the tungsten matrix were investigated. Samples were tested and examined microscopically and the most suitable environment where low porosity, high homogeneity and high amounts of infiltrant metal present in the finished MMC was used for later studies.

After a suitable atmosphere was determined, three different sintering/infiltraion temperatures were tested. For copper the three temperatures were 1150°C, 1200°C and 1250°C. Subsequently, sintering/infiltration dwell time (time at which a chosen temperature was held at) was varied (times used were one minute, five minutes and 60 minutes). The aim of this was to reduce the time tungsten particles were exposed to elevated temperatures and to minimize the degree of coarsening and increase the level of open porosity.

During the sintering/infiltration phase two concurrent activities occur. The first is the coarsening and densification of the tungsten particles. This happens at as low as 70% of their absolute melting temperature [12]. The other step is that of infiltration. This happens after the infiltrant metal has been melted and infiltrated through a series of displacement and capillary forces.

Silver was later explored as a possible secondary infiltrant metal. Given the relatively low melting temperature of silver (961.78°C), temperatures used in the infiltration of silver were 1050°C and 1150°C. The aim of introducing silver was to expand the technology used to other tungsten based two material systems that had significant impact to the economy.

3.1.6. Additional tests

Apart from the standard PIM method described above, several other methods were also attempted in the manufacture of samples.

As tungsten powder is costly and hard to obtain due to legal and security restrictions, Powder Metallurgy (PM) was used in this study as a means to test the viability of certain powder formulations before the addition of polymeric binders in the feedstock formulation. The key composition that utilized the PM intermediary was the addition of yttria as a Zener grain growth inhibitor. Tungsten powders of 1μm and 100 nm particulate sizes were mixed with 2.0wt%, 4.0wt% and 10.0wt% yttria of particle size of 30 nm. Samples containing no yttria were also examined as a means of control. The testing sample matrix is given in Table 3.1 below.

Table 3.1: Composition of compacts used in the study of yttria addition on the structure of sintered tungsten powders.

Sample	Wt% of 100nm W	Wt% of 1μm W	Wt% of Y_2O_3
1	0	100	0
2	0	98	2

3	0	96	4
4	100	0	0
5	98	0	2
6	96	0	4

Dry tumbling of the mixture was conducted in an Inversina shaker mixer for 24 hours under air. Powders were then separated into portions of 10g according to their sample composition.

Separated powders were cold pressed in a Wabash 30-ton press at a pressure of 370MPa for 300 seconds to form circular discs of 15mm in diameter and 1-2mm in height. The punch, die and a pressed disc are shown in Figure 3.11.

Pressed discs were then sintered in hydrogen for one hour at 1250°C and the resulting product was sectioned, polished and examined microscopically for densification and grain growth.

Figure 3.11: Photo showing components of the PM process clockwise from left, the punch, the die, the base and two pressed tungsten discs.

Another test done in the earlier stages was that of microwave sintering. In this attempt, the samples were sintered and infiltrated inside a microwave furnace. It was reported that microwave sintering of tungsten powders was able to produce nano-grained tungsten microstructures[13]. Microwave heating differs from conventional induction heating systems as the heating of the material is due to energy conversion of the electromagnetic radiation within the samples as opposed to other systems which rely on convective and conductive heat transfer. This results in extremely high heating rates and shorter sintering times that can result in smaller grain sizes.

For this experiment, debinded tungsten copper samples (from 100nm size tungsten powders) were placed inside an alumina crucible that was then heated in a modified microwave oven. Unlike tests that were done in a CM tube furnace, a hydrogen environment could not be applied to this setup as the risk of arcing and sparking occurring between the metals under microwave could lead to combustion of the hydrogen gas. After the microwave cycle was complete, the alumina crucible was then emptied and its contents analyzed.

Addition of copper into the tungsten matrix during the injection moulding phase was also explored. This test saw the inclusion of 5.0wt% of 10µm copper added to feedstock consisting of 1µm tungsten. The aim of this test was to increase the percentage copper within the final matrix by means of adhesion effects during infiltration.

It is theorized that the addition of a small amount of copper (5.0% by weight) into the tungsten feedstock could increase the amount of copper infiltration within the finished sample. Upon reaching a temperature above the melting point of copper, these admixed grains of copper form reservoirs within the tungsten matrix that increase the flow of additional copper up through the matrix by the process of cohesion and surface tension. Cohesion effects between like materials attract the upwards flowing copper towards the copper reservoirs. Upon contact, surface tension acts to join the copper reservoir and copper infiltrating front as one entity to reduce the free surface area of the liquid. This causes the reservoir to be pulled downwards into the copper front, but also exerts an equal force that pulls the copper front further up through the tungsten matrix.

The high surface tension displayed by liquid copper (as shown in Table 3.2 below) also further makes it a suitable candidate for this admixing process. This infiltration process was carried out for one hour at 1150°C.

Table 3.2 Surface tension data for several reference liquids

Liquid	Surface tension (Dyne/cm)
Mercury @ 20ºC	435.5
Water @ 20ºC	72.8
Silver @ 962ºC	838.0
Copper @ 1083ºC	1300.0

3.2. Characterization

3.2.1. Microstructure evaluation

The study of microstructure is to observe visually the building blocks of the material and attempt to relate its structure to its intrinsic properties. This is done with the use of a Scanning Electron Microscope (SEM)[14].

SEM works by aiming a focused electron beam towards a sample in vacuum. The incident electrons knock out secondary electrons within the sample. These secondary electrons are measured using a detector and the signal is sent to an amplifier. An image is then built up from the electrons emitted from each spot on the sample. The beam is scanned back and forth across a sample, row by row, resulting in a complete image. To prepare a sample for SEM analysis, the sample has to be made smooth, scratch free and electrically conductive. The SEM machine used in this study was the JEOL JSM 5600LV SEM using a conventional tungsten filament.

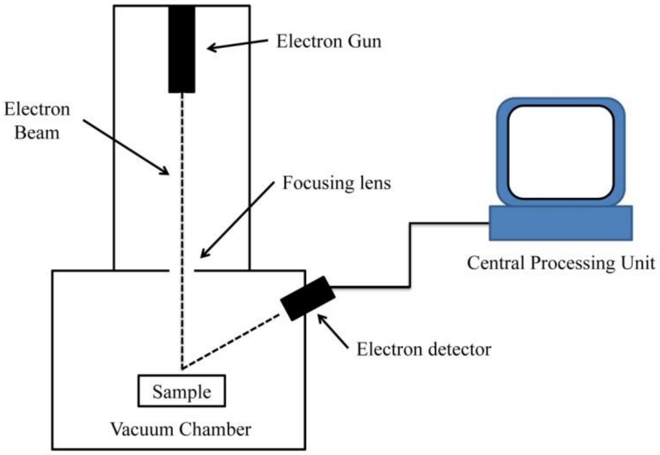

Figure 3.12: Visual schematic of an SEM

Samples are prepared for SEM analysis by placing them into an epoxy thermosetting base. This is done by placing the sample into a latex mould using placing clips, and subsequently pouring catalyzed epoxy over the sample The catalyzed epoxy hardens to a hard clear plastic manifold that allows for the sample to be manipulated with ease (Figure 3.13 below). Epoxy was chosen over other resins like phenolic and acrylic resins as they have negligible shrinkage and harden quickly (approximately four hours under room temperature and pressure).

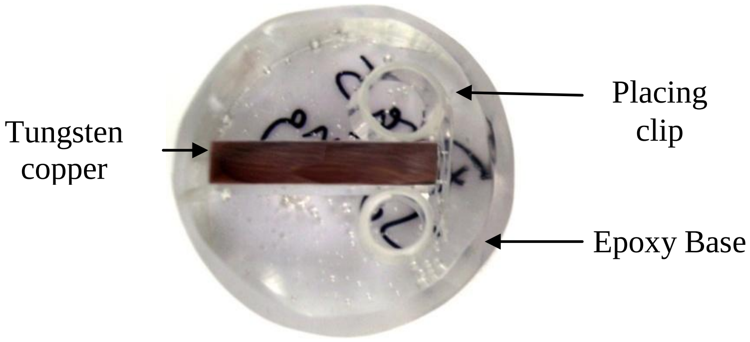

Figure 3.13: Polished sample mounted in epoxy with plastic placing clip visible.

After the epoxy has hardened, the embedded samples are then wet ground and polished using a Persi Mecapol P225U polisher (shown below in Figure 3.14). This is done by grinding with successively finer abrasive media applied to a rotating disc. The abrasives used for this study were silicon carbide at the initial grinding stages and diamond paste for the final polishing stage. Unlike other metals, etching of tungsten based composites is usually not required as tungsten, given its high density, produces a much darker colouration in contrast to other lighter metals under SEM analysis, making grain boundaries distinguishable without the need for etching.

Figure 3.14: The Persi Mecapol P225U polisher/grinder used in this study.

After polishing, samples were coated with a conductive layer of gold. This coating prevents electrons from building up within the insulating epoxy mould by discharging the electrons to the earth via the conductive stage. A build up of negatively charged electrons will deflect incoming electrons and result in a blurred signal.

Common features observable by SEM analysis are that of grain size, compositional/microstructural homogeniety and porosity. Inhomogeniety and porosity in MMCs are undesirable as they lead to variations in resistivity and thermal conductivity, while grain size affects the strength of the material. The University of Texas Health Science Centre at San Antonio ImageTool version 3.0 software[15] was used in the analysis of porosity and grain size.

3.2.2. Compositional analysis

The composition of constituents within an MMC can be used to predict its properties based on their respective weight percentage value. A volume fraction method is used as a predictor for many intrinsic properties (Voight’s Law) for uniformly distributed composites.

Compositional testing was done using an Energy dispersive X-ray spectroscopy (EDX, though sometimes also referred to as EDS). This test is done with a detector set up as an attachment to a standard SEM apparatus. The EDX used in this study was by Oxford Instruments and was linked to an INCA software system.

When an electron bean is targeted at an atom, it knocks out electrons from within an inner valence shell. When a valence electron from an inner shell is knocked out, the atom drops in stability. To retain its original stability, an electron from an outer shell makes a jump into the inner shell. This move causes a drop in energy as the outer shell electron is of a higher energy level. The energy that is released takes the form of X-rays that have unique wavelengths and energies. This data is then collected by a detector and a graph of X-ray intensity against energy level (measured in eV) is then plotted (Figure 3.15 below).

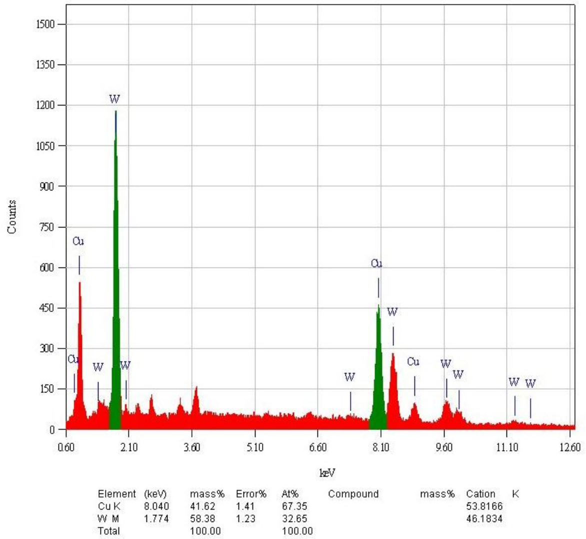

Element	(keV)	mass%	Error%	At%	Compound	mass%	Cation	K
Cu K	8.040	41.62	1.41	67.35			53.8166	
W M	1.774	58.38	1.23	32.65			46.1834	
Total		100.00		100.00				

Figure 3.15: EDX scan of tungsten copper MMC with 41.6wt% copper.

The position of the peaks is used to identify the material within the sample by comparing it with a database of known material peaks.

To quantify the amount of elements within a scanned sample, background noise on the scan is first reduced through a Gaussian fit and the areas under the respective peaks are calculated. The values are then subjected to an algorithm (most common is the ZAF, Atomic number-Absorbance-Fluorescence Algorithm) to calculate the weight percent of an element within the sample.

One point to note when doing EDX scanning is to remove any coating from a sample before analysis. Though sputter coatings result in clearer SEM images, the level of error within the analysis is increased as the penetration level of electrons into the sample is reduced The addition of another element (common sputtering agents are Gold and Carbon) will cause additional peaks that affect the accuracy of Gaussian fit, altering the actual area under the peaks of various energy levels and subsequently affect the ZAF analysis.

3.2.3. Hardness

Hardness is an important property which determines a metals ability to resist plastic deformation under the effect of indentation. A common method of measuring hardness is the Vickers indentation test. In this method an indent is made on the material using an indenter with a fixed amount of force. The indenter used in Vickers hardness testing is a square-based pyramid whose opposite sides meet at the apex at an angle of 136°. The Vickers Hardness value (H_V) is calculated using the formula[16]:

$$H_V = 1.854 \frac{F}{D^2}$$

Where *F* is force in KgF and *D* is length of the indentation in mm. To convert to an SI unit scale of MPa, the H_V value is multiplied by the acceleration due to gravity, g, (commonly taken as $9.81 m/s^2$). The force used in throughout this study was 100KgF and the method used was in accordance to ASTM E 384.

Testing was done on samples that were already polished and mounted in epoxy. This ensured that there was a large flat base to ensure stability when the load was applied.

The presence of a sputter coat also made the indentation more distinguishable (as can be seen below in Figure 3.16)

The apparatus used to determine the hardness was a Matsuzawa MMT-X3 Digital Vickers hardness tester.

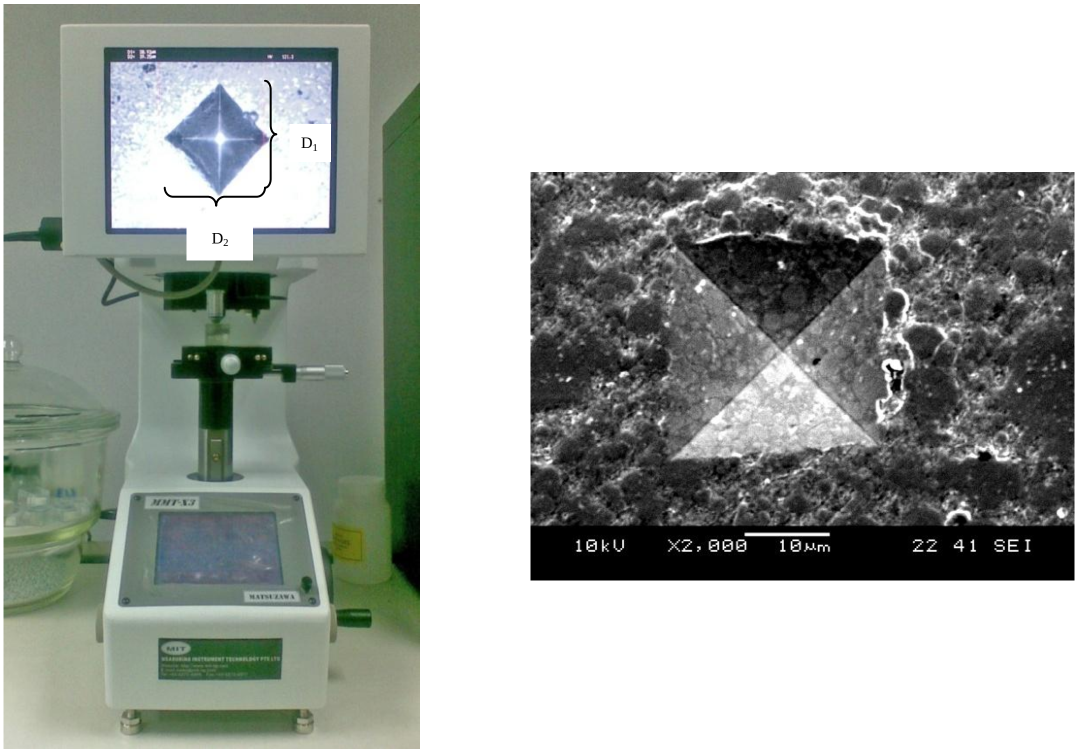

Figure 3.16: Photo showing on the left, the Matsuzawa hardness machine with a magnified indentation. D$_1$ and D$_2$ denote two diagonals used in the hardness measurement and right, SEM image of a Vickers indentation.

The Vickers hardness value is exceptionally useful as it can be used to estimate the yield strength of the sample by the simple relationship:

$$\text{Vickers Hardness} \sim 3\sigma_y$$

Where σ_y is the yield strength of material. This is especially useful when a tensile test is not available.

3.2.4. Conductivity

Heat Sinks and electrodes are common applications of tungsten copper and tungsten silver metal MMCs. As these two applications are dependent on a material's thermal and electrical conductance, it is therefore important to determine the conductivity of the sample produced.

Bulk conductivity was measured using a four-point probe. The four point probe used in this study is a Keithley 4200 four point probe.

The bulk resistivity for a sample is calculated as:

$$\rho_{resist} = 2\pi s\left(\frac{V}{I}\right)$$

Where ρ_{resist} is the bulk resistivity, s is the spacing between the probe tips (1mm), I is the applied current and V is the measured voltage.

Conductivity is a reciprocal of resistivity and is expressed as a percentage of the conductivity of annealed copper (%IACS). This value is important as a major use of tungsten based composites is in the field of high voltage electrodes where the conductivity can determine the amount of energy loss within a system. For metals, the electrical conductivity is an excellent indication of its thermal conductivity and is proportional to the absolute temperature. This relationship is called the Wiedemann-Franz law and it is expressed by [17]:

$$\frac{K}{\sigma} = LT$$

Where K is the thermal conductivity, σ is the electrical conductivity, T is the absolute temperature and L is the Lorenz number, the constant between two metals that is only variable to absolute temperature.

3.2.5. Dimensional change

Dimensional analysis, specifically that of shrinkage, is an important parameter for PIM components as it determines the amount of shrinkage occurring from the post-injection moulded green parts to the final sintered states. This data allows die makers to design dies that are able to produce samples of a final sintered size given the relevant shrinkage data. It also gives the production engineer data on how feedstock formulations can be adjusted to facilitate required tolerances.

To quantify these features, measurements was done in two ways, the first with a digital vernier caliper, and the second with an optical comparator.

The vernier caliper used was a Mitutoyo 500 series digital vernier caliper. The caliper had a resolution of 0.01 mm and was used only for disc, tensile and rectangular bar shaped samples. For compacted discs, their diameter and thickness were measured while rectangular injection moulded bars had their length, breadth and thickness measured. For tensile bars, apart from thickness and length, the breadth of both the thinner centre and the wider ends were measured.

The optical comparator (Figure 3.17 below) was used to measure the dimensions of the more complex diagnostic component that consisted of gaps, through holes and overhang features (Figure 3.18 below). An optical comparator works by measuring the silhouette casted on a translucent screen. Features are then measured by moving the image along stipulated positions on the screen. The final displacement will be the length to be measured. Apart from linear dimensions, the optical comparator is also able to measure angles as well as the diameters of circular components. The comparator used in this study was a Deltronic DH 216 optical profile comparator.

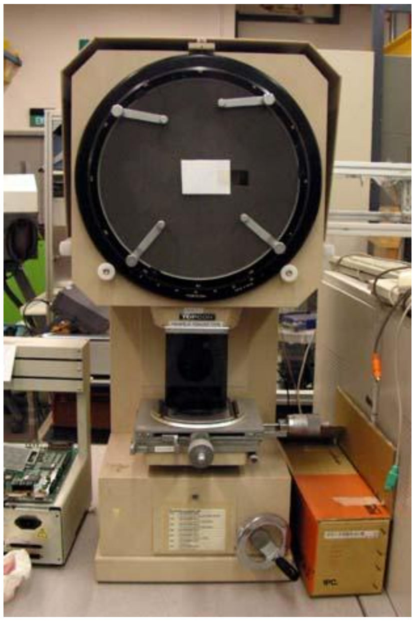

Figure 3.17: An optical comparator.

Figure 3.18: PIM diagnostic component featuring different linear, radial and resolution features.

To collect useful data for the PIM process, dimensions were measured for post injection moulded components after the samples had been sintered and infiltrated. The corresponding dimensions are then compared and shrinkage data is calculated.

3.2.6. Thermal expansion

As the MMC investigated in this study is used in heat dissipation applications such as in semiconductor packaging as well as heat sinks, it is therefore important to determine the coefficient of thermal expansion (CTE) at the operating temperatures. Mismatch of CTE between heat sink and base materials will result in thermal stresses that can damage or reduce the lifespan of their base material.

To determine CTE, the sample must first be ground into smaller pieces less than five millimeters thick with a parallel top and base. The grounded samples are then placed into a thermo-mechanical analyzer where a quartz probe is used to measure the expansion of the sample as it is heated to a predetermined temperature. The samples are immersed in nitrogen during the heating process to prevent any oxidation. The TA instruments TMA 2940 was used in this study (Figure 3.19). The temperature range investigated was from 25°C to 450°C.

Figure 3.19: Photo of TA instruments TMA 2940, the TMA used in this study

The CTE is given by the expression:

$$\alpha = \frac{\Delta B}{B}\left(\frac{1}{\Delta T}\right)$$

Where α is the coefficient of thermal expansion to be determined, *ΔB* is the change in length, *B* is the original length and *ΔT* is the change in temperature.

3.2.7. Density

As with all materials made from powder constituents a comparison of theoretical density (calculated by the volume fraction of the constituent densities) and final density can be a good indication of the extent of sintering that has occurred.

The most direct method of calculating density is by using the Archimedes principle of displacement and buoyancy. In this method, the sample is first weighed in air and subsequently measured while immersed in a fluid of known density[18]. In this study, distilled water was used. The density of the sample can then be determined by the formula given by:

$$\rho_{sample} = \left(\frac{w_{air}}{w_{air} - w_{water}} \right) \rho_{water}$$

Where ρ_{sample} is the sample density, ρ_{water} is the density of water, and w_{air} , w_{water} are their weights in air and water respectively[18].

Figure 3.20: Density Determination kit.
(Top cone is for measuring w_{air} lower cone is for measuring w_{water})

In this study, for every sample that is infiltrated, a non infiltrated tungsten skeleton is produced concurrently using the same conditions by which the infiltrated sample is produced. This uninfiltrated sample is also subjected to density measurements.

A good use of this measured density is the calculation of composition. With the final density as well as the density of both copper and tungsten known, it is possible to establish the volume fraction of copper and tungsten with the material. This method can not only be used to determine the composition of the sample, it can also be used to determine if there has been porosity or incomplete infiltration occurring within the sample.

The Precisa 40SM-200A (Figure 3.20) with a density measurement kit was used in this study to measure density.

3.3. Overview of samples produced

A complete summary of experiments planned and variables tested during the course of this study can be found in Appendix A.

References

1. Ryu, H.J. and S.H. Hong, *Fabrication and properties of mechanically alloyed oxide-dispersed tungsten heavy alloys.* Materials Science and Engineering A, 2003. **363**: p. 179-184.
2. Naidich, J.V., V.S. Zhuravljov, and N.I. Frumina, *Wetting of rare-earth element oxides by metallic melts* Journal of Materials Science, 1990. **25**(4): p. 1895-1901.

3. German, R.M., et al., *Processing model for tungsten powders and extension to nanoscale size range*. Powder Metallurgy, 2006. **49**(19-27).
4. Hwang, K.S., G.J. Shu, and H.J. Lee, *Solvent Debinding Behavior of Powder Injection Molded Components Prepared from Powders with Different Particle Sizes.* Metallurgical and materials transactions A, 2005. **36A**(161-167).
5. Ghoniem, N.M. (1998) *High temperature oxidation of Tungsten and Molybdenum*. APEX study group meeting, The University of California at Los Angeles.
6. Bagshaw, T. and A. Mitchell, *The Solubility of Hydrogen in Liquid Silver.* Transactions of the Metallurgical Society of AIME 1968(2): p. 343.
7. Fukai, Y., *The metal-hydrogen system: basic bulk properties*. 2005: Springer Verlag.
8. German, R.M. and A. Bose, *Injection Molding of Metals and Ceramics*. 1997, New Jersey: Metal Powder Industries Federation.
9. Rosato, D., *Injection molding handbook.* 2000: Kluwer Academic Publishers.
10. Osswald, T.A., L.S. Turng, and P.J. Gramann, *Injection molding handbook*. 2001: Hanser New York.
11. Hwang, K.S. and Y.M. Hsieh, *Comparative Study of Pore Structure Evolution During Solvent and Thermal Debinding of Powder Injection Molded Parts.* Metallurgical and materials transactions A, 1996. **27A**: p. 245-253.
12. German, R.M., *Sintering Theory and Practice*. 1996: Wiley.
13. Jain, M., et al., *Microwave Sintering: A New Approach to Fine-Grain Tungsten-II.* International Journal of Powder Metallurgy, 2006. **42**: p. 53-57.

14. Plucknett, K.P. and P.F. Becher, *Processing and Microstructure Development of Titanium Carbide-Nickel Aluminide Composites Prepared by Melt Infiltration/Sintering (MIS).* Journal of the American Ceramic Society, 2001. **84**(1): p. 55-61.

15. Wilcox, C.D., et al., *ImageTool Version 3.0*, U.o.T.H.S.C.a.S. Antonio, Editor. 2002.

16. *ASTM standard E 384 - 99, "Standard Test Method for Microindentation Hardness of Materials"*. 1999, ASTM International.

17. M.Tritt, T., *Thermal Conductivity, Theory, Properties, and Applications*. 2004: Springer.

18. *British Standard EN 623-2:1993, "Advanced technical ceramics - Monolithic ceramics -General and textural properties - Part 2: Determination of density and porosity"*. 1993, European Committee for Standardization (CEN).

4. RESULTS AND DISCUSSION

This chapter will focus on explaining the mechanisms and theories of the results. A full presentation of results by sample can be found in Appendix B.

4.1.Discussion of hypothesis investigated

4.1.1. The effect of atmosphere on the infiltration process

In the first stage, reducing (hydrogen), inert (nitrogen) and vacuum atmospheres were explored. These tests were covered in samples 1, 2 and 3. Sample 1, where the tungsten matrix was infiltrated with copper at a temperature of 1250°C under hydrogen for 60 minutes revealed a homogenous void-free finished product (Figure 4.1). Further microstructural analysis using commercial image analysis programs [1] showed the average particle sizes for sample 1 to be in the range of one to two microns.

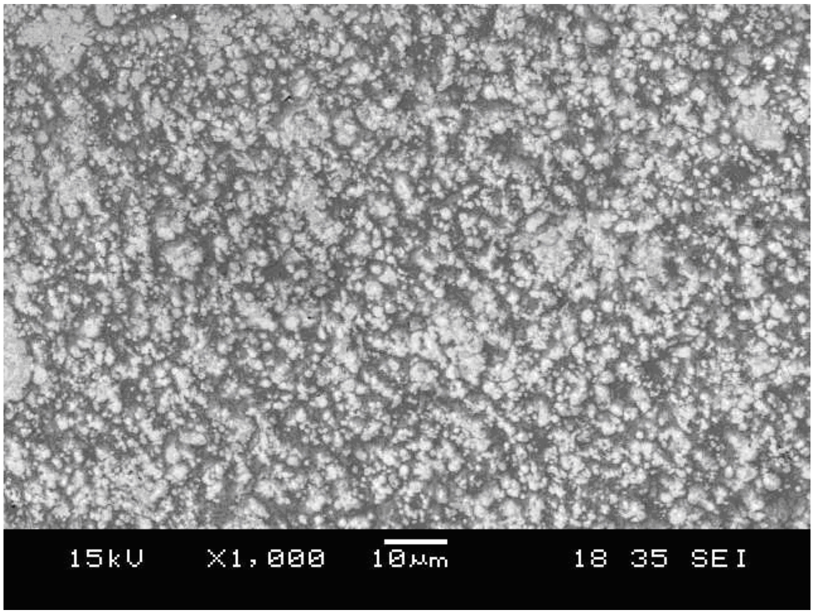

Figure 4.1: SEM micrograph of a polished cross sectional area of the infiltrated sample 1. Light regions are tungsten and darker regions are of copper.

Samples 2 and 3, which were processed in nitrogen and vacuum (700Pa) respectively, showed no signs of infiltration. The post processed tungsten compacts for samples 2 and 3 were encapsulated within a copper shell when removed from the furnace. This can be seen in Figure 4.2 below.

This phenomenon is attributed to the formation or a tenacious oxide layer on the free surfaces of the tungsten matrix. The equation for this oxidation is expressed as:

$$xW(s)+\frac{1}{2}yO_2(g)\longleftrightarrow W_xO_y(s) \tag{4.1}$$

The oxide layer forms as a result of exposure to air during the handling process. The high surface area attributed to fine powders makes it susceptible to spontaneous oxidation.

(i) (ii) (iii) (iv)

Figure 4.2: Photo showing failed infiltration when sintering/infiltrating under vacuum (i and ii) and under nitrogen (iii and iv).

Metal oxides have been shown to display high contact angles with molten copper [2]. Low contact angles are necessary for effective capillary action [3].

Visual examination of all infiltrated products processed in hydrogen (samples 4-21 and sample 33), showed that the integral features of the original injection moulded component were retained with little or no distortion.

Important observations from samples 7, 8 and 9 where a complex diagnostic component was produced (Figure 4.3 below) showed that small through holes remained open and no accumulation of copper at sharp angled corners was observed. Excess copper, when present, accumulated at the bottom of the sample and was easily removed with no damage to the bulk. Importantly, upwards infiltration was not obstructed by the gap. Resolution of the patterned feature on the top of the diagnostic samples also proved dimensionally congruent with the injection moulded green part and was proportionally reduced based on measured shrinkage factors.

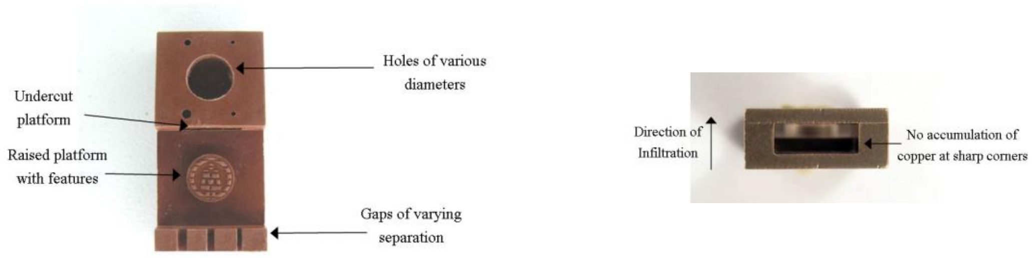

(i) (ii)

Figure 4.3: Finished product showing (i) full resolution of infiltrated sample and (ii), no accumulation of excess copper at the edges of the lower edge.

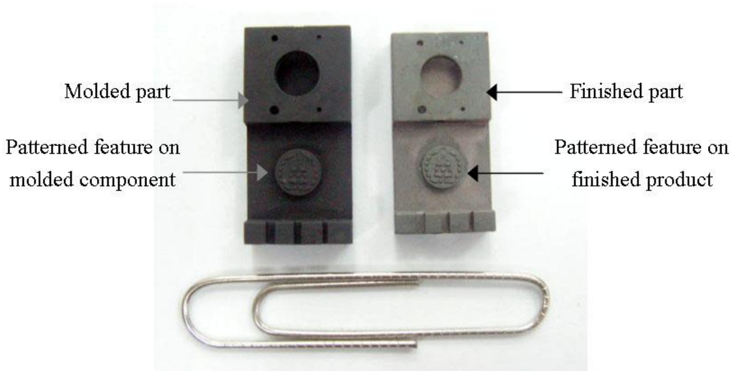

Figure 4.4: Macroscopic comparison of moulded component (left) and finished product showing clear resolution of injection moulded features and a direct shrinkage of the features in the finished component (right) Shrinkage factors were found to be between 5.6%- 6.9% for diagnostic components sintered for 60 minutes. A paperclip is used as a reference for the scale that the sample can be reduced to.

To explain the phenomena of infiltration, a cubic close packing of spheres was used. In this arrangement, each sphere can be resolved three dimensionally into truncated decahedrons. This is an Archimedean solid that is able to perpetuate through the entire matrix and can be used as a model to represent uniform space filling [4]. Forces of capillary action and volumetric displacement serve to push the liquid copper through the pores of the tungsten matrix. Viscous drag will result in opposition towards infiltration. First we consider the effect of capillary action on the infiltration process. The interfacial force acting upwards on spherical particle acting at a liquid-gas interface has been derived to be [5].

$$F_{capillary} = 2\pi r\gamma\left(1+\cos\theta-\frac{X}{r}\right) \tag{4.2}$$

Where r is the particle radius of the perform particles,γ is the surface tension of liquid, θ is the contact angle between liquid infiltrant and particle material and X is the depth of submergence of the particle.

This capillary force acts to pull the liquid copper through the tungsten matrix. This force is largely dependent on the wettibility of liquid copper onto tungsten. Contact angle for liquid copper on tungsten has been found to be less than 20° [6] which is a condition suitable for spontaneous infiltration.

When tungsten particles descend into the liquid copper, volumetric displacement will force the liquid up along the pores of the preform structure. The force required to raise the level of fluid to its new level (relative to the sphere, Figure 4.5) is analogous to the weight of the liquid melt displaced by the particle. This is a direct consequence of Archimede's principle and can be shown mathematically by:

$$F_{displ} = \rho_{liquid} g \pi X^2 \left(r - \frac{X}{3} \right) \tag{4.3}$$

Where ρ_{liquid} is the density of infiltrant and g is the acceleration due to gravity.

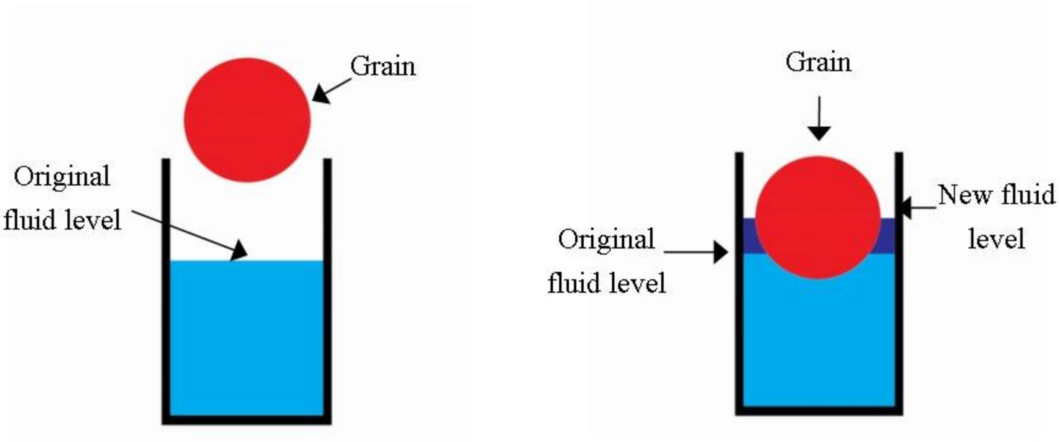

Figure 4.5: Diagram showing the displacement of a sphere within a fixed volume of liquid.

During infiltration, the tungsten preform sinks into the liquid metal at a constant speed. This can be related to terminal velocity and the equation governing Stokes law can be applied where the equation for viscous drag on a particle in fluid flow is given by:

$$F_{drag} = 6\pi\eta r v \tag{4.4}$$

Where η is the viscosity of liquid metal, v is the terminal velocity of metal preform into liquid metal, which can also be viewed as the speed for which the infiltration process proceeds.

This force is the resistance to infiltration as it works against the direction of infiltration. Stokes' Law for a sphere was found experimentally to be reasonably accurate for:

$$Re = \frac{\rho_{liquid} v 2r}{\eta} < 1$$

Mathematically, the summation for the entire process can be quantified as:

Infiltrating Force = Capillary force + Displacement force - Viscous drag

$$= 2\pi r\gamma\left(1+\cos\theta-\frac{X}{r}\right) + \rho_{liquid} g\pi X^2\left(r-\frac{X}{3}\right) - 6\pi\eta r v \quad (4.5)$$

Taking $X=r$ for full submergence of the sphere within the infiltrant, the results can be reduced to:

$$= 2\pi r\gamma(\cos\theta) + \left(\frac{2}{3}\right)\rho_{liquid} g\pi r^3 - 6\pi\eta r v$$

$$= 2\pi r\left[\gamma\cos\theta+\frac{\rho_{liquid} g r^2}{3}-3\eta v\right] \quad (4.6)$$

For continual infiltration, it is required that the infiltration force (Equation 4.6) is positive,

$$\left[\gamma\cos\theta+\frac{\rho_{liquid} g r^2}{3}-3\eta v\right] = Z > 0 \quad (4.7)$$

The value *Z*, henceforth referred to as the infiltration number, is an indication of the systems tendency towards spontaneous infiltration. A more positive value of *Z* would indicate a greater likelihood of infiltration by the liquid metal in the system. In sintering systems where ultrafine powders are the precursor, abnormal grain growth (which will be covered in greater detail later in this chapter) is often a distinct feature.

The method used in the derivation of the formula is based on a uniform particle size. It is however more accurate to include the abnormal grain growth effect on the final value. In this context, as this model is based on a series of three dimensional building blocks, the effect abnormal grain growth has on infiltration can be referenced using the rule of mixture method:

$$\sum V_f \left[\gamma \cos\theta + \frac{\rho_{liquid} g r^2}{3} - 3\eta v \right] = \quad Z' \quad > \quad 0 \qquad (4.8)$$

V_f represents the volume fraction of a particular particle size and Z' is an adjusted infiltration number that takes into the account the distribution for a range of preform particle sizes.

4.1.2. The effect of sintering temperature and tungsten powder sizes on the properties of the tungsten copper MMC

After the selection of hydrogen as a suitable atmosphere for the processing of the tungsten-copper metal matrix composites, it was necessary to study the effect that starting tungsten powder size and the various sintering and infiltration temperatures had on the final metal matrix composites.

In this phase two main parameters were investigated; starting tungsten powder size and sintering temperature. The two starting powder sizes were 100nm and 1µm, while sintering temperatures used were above the melting point of copper (1084.62°C) at 1150°C, 1200°C and 1250°C respectively.

Table 4.1: Summary of the properties of several tungsten copper MMCs. Sample 7, 8 and 9 were manufactured from one micron tungsten powders with sintering temperatures of 1150°C, 1200°C and 1250°C, respectively while samples 10, 11 and 12 are manufactured from 100nm powders at the same respective temperatures.

Sample	Composition (wt% copper)	Mean hardness (H_V)	Mean conductivity (% IACS)	Mean CTE ($10^{-6}K^{-1}$)
7	38.46	206	44.70	13.05
8	28.37	231	41.03	12.73

9	24.10	247	42.22	10.50
10	18.32	253	21.91	13.56
11	16.56	239	19.65	13.99
12	14.11	244	19.76	13.46

As solubility of tungsten in molten copper is negligible [7]. The synthesis of the metal matrix composite can be considered as comprising of two discreet stages; firstly, the solid state sintering of a tungsten preform, and subsequently the infiltration of the metal matrix preform by molten copper.

Infiltration requires the flow of molten copper through the interconnected interstices of the tungsten skeletal matrix. At higher sintering temperatures, interconnected porosity is lowered as densification becomes more extensive [8, 9]. There are two main mechanisms in play at this point, densification and grain growth. Densification reduces the porosity within the samples, while grain growth leads to the increase in grain size, with some grains growing at the expense of its neighbouring grains [10]. While uniform densification and grain growth was evident in samples processed using 1µm tungsten powders, samples produced using 100nm tungsten powders showed abnormal grain growth within the tungsten matrix.

The general trend of increasing hardness, resistivity, shrinkage factor, density and a decrease in the coefficient of thermal expansion (CTE) with increasing sintering temperatures for samples produced using 1µm tungsten powders is directly due to a decrease in infiltrant content. The large drop in percentage copper between samples 7 and

8 as compared to that between samples 8 and 9 is attributed to the lowering of densification rates at higher sintering temperatures for fine tungsten powders [11].

Experimental values for hardness of 1µm tungsten powders were higher than those predicted by the law of mixtures (Figure 4.6). Upon cooling, the molten copper solidifies to produce two interwoven matrices of copper and tungsten. These two matrices have differing coefficient of thermal expansions (CTE for copper at 20ºC is $16.5x10^{-6}K^{-1}$, CTE for tungsten at the same temperature is $4.5x10^{-6}K^{-1}$) [12]. The copper matrix, which contracts more than the tungsten matrix, has a tensile stress subjected to it. The solidification shrinkage [13, 14] that is experienced by copper upon solidification also contributes to the tensile stress. Due to the ductile nature of copper, the copper matrix is in the process of shrinking strain hardened due to an increase in dislocation density, resulting in the significant elevation of hardness throughout the composite [15]. The compressive stress experienced by the tungsten matrix as a result of copper's solidification shrinkage also constitutes to a hardening effect on the tungsten matrix [16].

Comparing samples 10, 11 and 12 where the starting powder used is 100nm, the drop in hardness for samples 11 and 12 despite containing less copper as compared to sample 10 is due to the higher density of abnormal grains (of 20-25µm diameter). This decrease in the density of grain boundaries allows for dislocations to continuously propagate without arrest, leading to hardness that is lower than theoretically predicted, despite a higher volume fraction of harder tungsten. Compared to samples 10 and 11 that were also produced using 100nm tungsten powders, the decrease in grain boundary density also resulted in a higher than expected conductivity for sample 12 as a reduction in grain boundaries resulted in a longer mean free path for unobstructed electrons propagation.

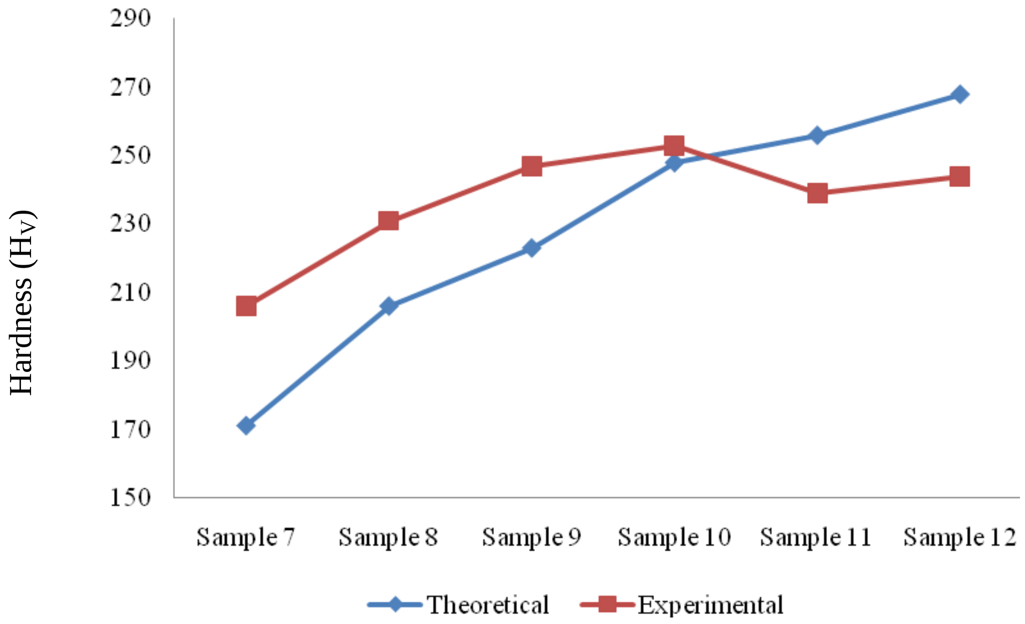

Figure 4.6: Graph showing the theoretical and experimental values of hardness for samples 7 – 12

The lower values of experimental electrical conductivity for all samples as compared to theoretical values (Figure 4.7) can also be attributed to increase in dislocation density [17, 18] within both copper and tungsten constituents due to CTE mismatch of copper and tungsten phases. Dislocations act as regions of electron scattering and this obstruction lowers the conductivity of the dislocated metal by posing as an obstacle and reduces the mean free path of an electron. The increase in grain boundary concentration in samples produced using 100nm tungsten powder as compared to those produced using 1μm powders resulted in a distinct drop in conductivity between samples using the two starting powder sizes.

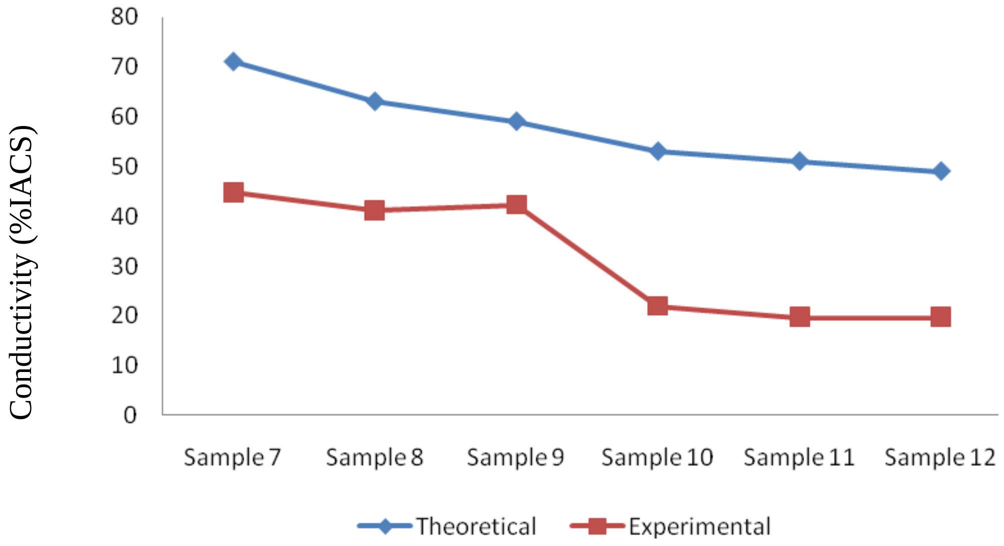

Figure 4.7: Graph showing the theoretical and experimental values of conductivity for samples 7 – 12.

It is important to note that from electrical resistivity, one can also predict the thermal resistivity of the composite using the Wiedemann-Franz law for metals [19], which states that for a given temperature, electrical resistivity is proportional to thermal resistivity.

Experimental CTE values were also shown to be significantly higher than theoretical values. This is due to elastic stress strain interactions between the interwoven infiltrant and tungsten matrices of differing modulus. During heating, the copper matrix expands isotropically and is constrained by the tungsten matrix of a lower CTE both through physical obstruction and strong interfacial bonding [6]. The tungsten matrix is not a uniformly continuous network but consists of adjacent particles that are joined together by means of a narrow neck. Expansion of copper upon heating is hence able to produce sufficient stress upon the tungsten matrix to strain it. Some of the initial sintered necks then rupture during the isotropic expansion of copper, resulting in a CTE that is closer to that of copper than the theoretically expected value.

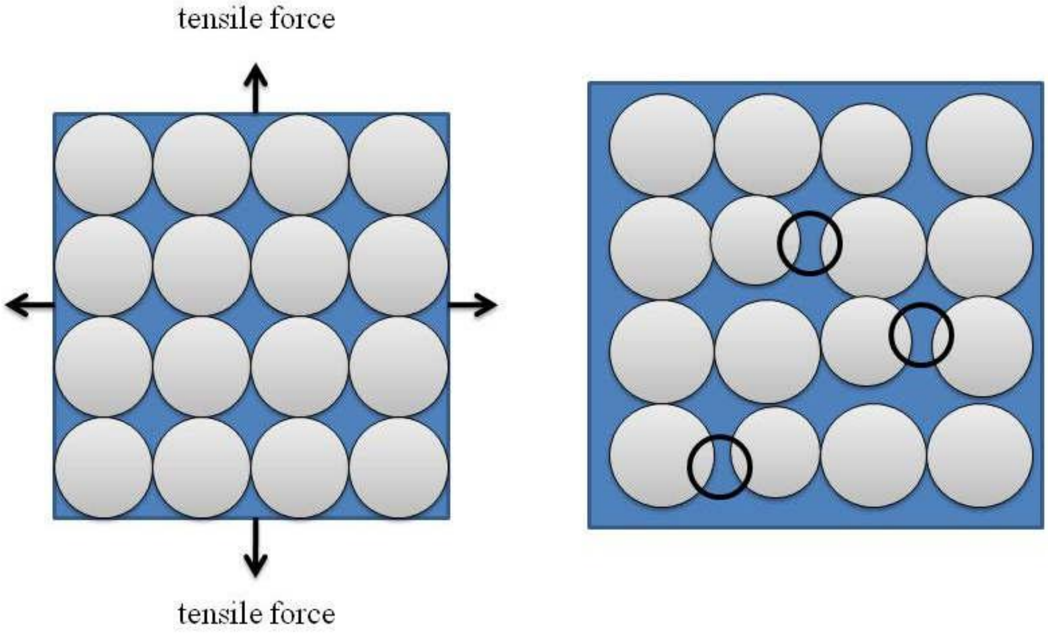

(i) (ii)

Figure 4.8: Diagram showing the effect of copper phase expansion on the tungsten matrix. On the left, (i), shows a tungsten matrix in sea of solid copper at room temperature. The arrows show the tensile forces acting on the composite during the heating process. The diagram on the right, (ii), shows the same matrix after it has been heated to an elevated temperature. During the heating process, the continuous phase of copper expands isotropically and this causes some weak necks formed between adjacent tungsten particles to break, as shown by the circles in (ii).

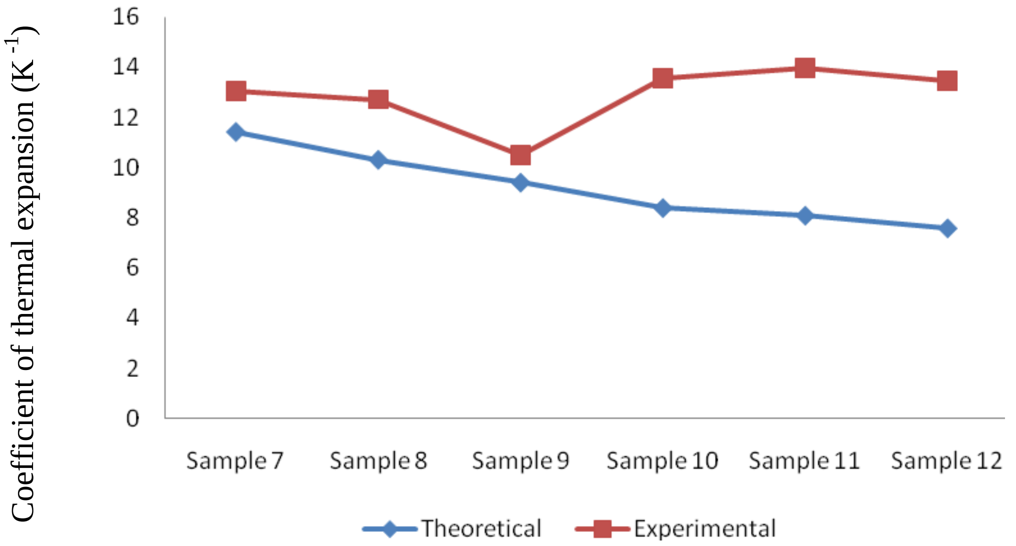

Figure 4.9: Graph showing the comparison between theoretical and experimental CTE values for samples 7-12.

A comparison between the different starting tungsten powder sizes (sample 7 vs sample 10, sample 8 vs sample 11 and sample 9 vs sample 12) for the identical processing conditions showed that MMCs processed with 100nm powders showed more extensive densification and thus a lower copper content. This lowering in copper content resulted in a lowering of conductivity and higher hardness. While a direct comparison between sample 7 to 10 and 8 to 11 yielded expectedly harder values for the latter samples, the comparison of 9 to 12 yielded an unexpected dip in hardness for the sample produced using 100nm powders. This phenomenon is attributed to the presence of abnormal grains that reduce the Hall-Petch strengthening effect as mentioned earlier.

The most discernable difference between tungsten matrices produced using 100nm and 1µm tungsten powders was the presence of abnormal grain growth. That observation was present in all sintered 100 nm samples. Abnormal grain growth was not observed in samples produced using 1µm tungsten powders.

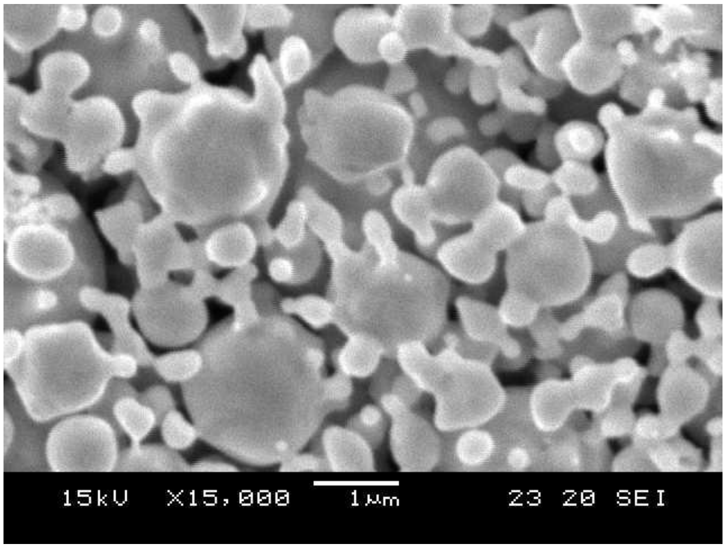

Figure 4.10: SEM photo at 15,000 times magnification showing the assimilation of 100nm tungsten grains into larger grains in excess of one micron in forming larger, more energetically stable tungsten particles.

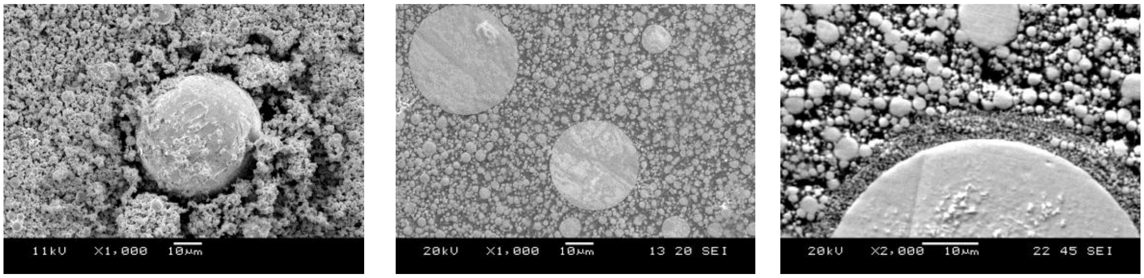

(i) (ii) (iii)

Figure 4.11: SEM photographs showing abnormal grain growth in (i) an uninfiltrated tungsten matrix and (ii) an infiltrated tungsten matrix and (iii) close up of the edge of an abnormal grain showing preferential grain growth at the expense of neighbouring grains.

For all sintering temperatures, the final grain size of the abnormal grains averaged at 20-25µm in diameter. More in depth examination showed an evidence of mass flow on the surface of the abnormal grains caused by the assimilation of the abnormal grain at the expense of its adjacent smaller neighbours (Figure 4.11(iii)).

The near perfect spherical configuration of the grains at this size was correlated directly to the lowest possible surface area to mass ratio.

The driving force towards sintering is the reduction of free surface area. While densification reduces porosity, coarsening will lead to larger interparticulate pores. To compare the driving force of abnormally large grains forming in the tungsten matrix, we shall consider the reduction in surface area from the two starting powder constituents (100nm and 1µm powder) to a finished 20µm diameter tungsten grain. We shall assume that both starting and finished grains are perfectly spherical and fully dense.

We will take the *r* to represent the lowest common factor for grain radius, which in this case would be 50nm. All subsequent radii will be multiples of *r*.

First we determine the number of starting powders required to form a 20µm diameter tungsten sphere. This can be done by dividing the volume of the 20µm sphere by the volumes of the two starting grains sizes:

For 100nm powders, the number of powders required to form a 20µm sphere is:

$$\frac{{}^{4}\!/_{3}\,\pi\left(200r\right)^{3}}{{}^{4}\!/_{3}\,\pi r^{3}} = 200^{3} \tag{4.9}$$

For 1µm powders, the number of powders required to form a 20µm sphere is

$$\frac{{}^{4}\!/_{3}\,\pi\left(200r\right)^{3}}{{}^{4}\!/_{3}\,\pi\left(10r\right)^{3}} = 20^{3} \tag{4.10}$$

Next we calculate the total surface areas for the three respective grains for a fixed volume of tungsten as:

For 100nm powders,

$$200^3\left(4\pi r^2\right)=\left(32\times10^6\right)\pi r^2 \tag{4.11}$$

For 1µm powders,

$$20^3\left(4\pi\left(10r\right)^2\right)=\left(32\times10^5\right)\pi r^2 \tag{4.12}$$

And for a 20µm powder is,

$$\left(4\pi\left(200r\right)^2\right)=\left(16\times10^4\right)\pi r^2 \tag{4.13}$$

Dividing Equation 4.11 and 4.12 by Equation 4.13 respectively, we can see that the reductions in surface areas are 200 and 20 times respectively.

Hence it can be seen that with 100nm powders as a precursor, the driving force in producing an abnormal grain of 20µm in diameter is 10 times greater than that of 1µm tungsten powders. Similar results were also observed in other independent studies [20].

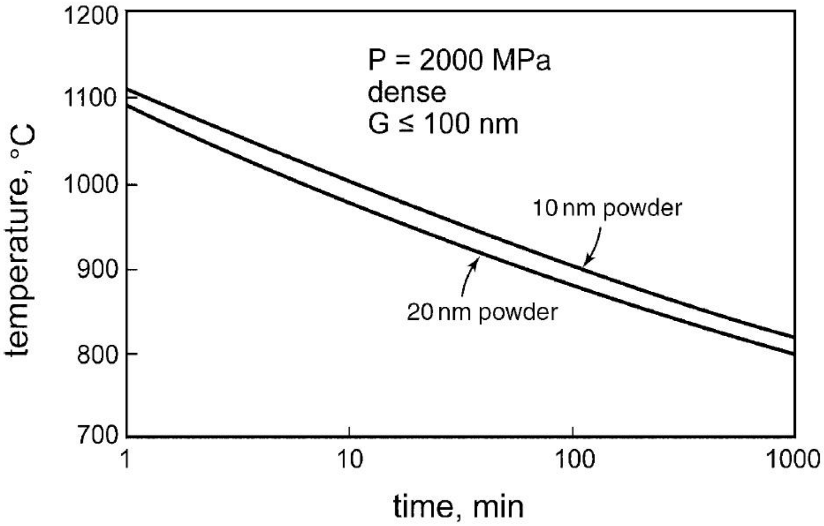

Figure 4.12: The combination of sintering temperature and sintering time needed to produce a maximum grain size of 100nm for two starting tungsten particle sizes, 10nm and 20nm. All of these solutions are based on a 2GPa compaction pressure and sintered density of at least 96% of theoretical [20].

4.1.3. The effect of holding times during sintering on the properties of the tungsten based composites

The effect of holding times was experimented on samples produced using 100nm tungsten powders. This was done in conjunction with an integrated debinding heat cycle.

The main purpose of this experiment was to determine if grain growth could be controlled significantly with a reduction in time at the lowest possible sintering temperature (which in this study was determined to be 1150°C). Apart from grain size control, reduction in sintering time can also translate into economical savings. An overall reduction in process time would reduce the amount of power, hydrogen and man hours required for the manufacturing cycle.

.

Table 4.2: Summary of the properties of tungsten copper MMCs sample 15, 14 and 10 produced using 100nm tungsten powders and infiltrated at temperatures of 1150°C for 1min, 5min and 60min soaking times.

Sample	Composition (wt% copper)	Mean hardness (H_V)	Mean conductivity (% IACS)	Mean CTE ($10^{-6}K^{-1}$)
15	10.28	281	27.69	14.80
14	25.75	287	24.50	14.86
10	18.32	253	21.91	13.56

A short sintering and infiltrating time of one minute lead to a lower than expected amount of copper present within the final MMC. SEM examination of sample 15 (Figure 4.13 below) showed that this reduction in copper content was due to incomplete infiltration of the tungsten matrix by copper when soaked at 1150°C for one minute. As the focus of this study was in the synthesis of fully dense samples, our discussion will shift towards samples 10 and 14.

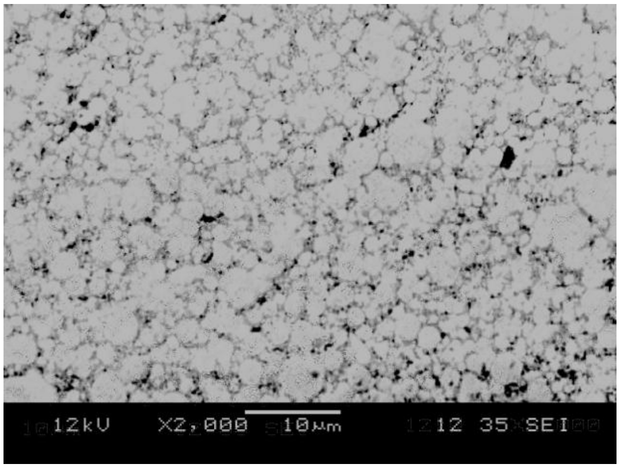

Figure 4.13: SEM photograph of a sectioned sample of the MMC which has been infiltrated/sintered at 1150°C for one minute. The black regions are voids within the MMC.

From SEM examination of the tungsten matrices of the two fully dense MMCs (sample 10 and 14). It was evident that a reduction in peak temperature dwell time from one hour to 5 minutes did manage to reduce significantly the final grain size of the tungsten matrix from 2 µm to an average of 500nm. This can be seen clearly in Figure 4.14 below.

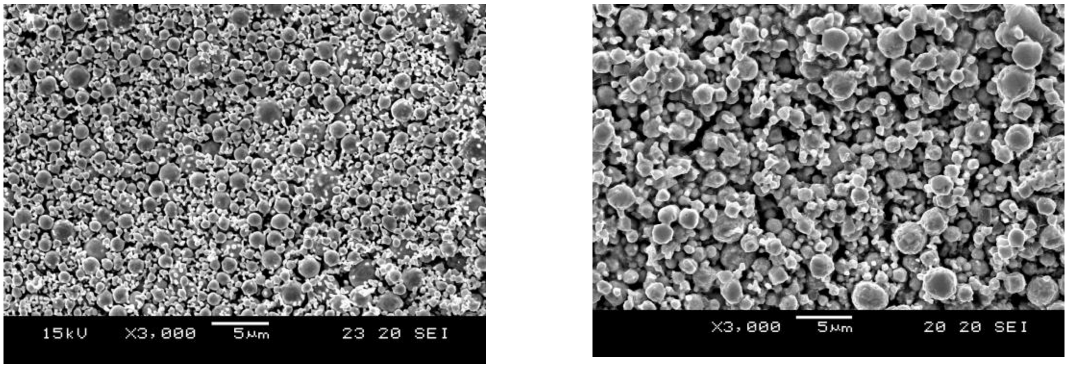

(i) (ii)

Figure 4.14: SEM photographs showing smaller tungsten grain sizes present in samples sintered and infiltrated at 1150°C for 5 minutes (i) as compared to samples done so for 60 minutes (ii).

Table 4.3: Comparison between theoretical and experimental values of hardness, conductivity and CTE for samples 10 and 14.

	Experimental			Theoretical		
Sample	Hardness (H_V)	Conductivity (% IACS)	CTE ($10^{-6}K^{-1}$)	Hardness (H_V)	Conductivity (% IACS)	CTE ($10^{-6}K^{-1}$)
14	287	24.50	14.86	216	60.53	9.64
10	253	21.91	13.56	243	53.51	8.41

While CTE and conductivity value deviations can be attributed to explanations covered in 4.1.2, a comparison between experimental and theoretical hardness values (as shown in Table 4.3 above) showed that while experimental hardness for samples sintered and infiltrated for one hour showed a 4% decrease, samples sintered for five minutes had a value of hardness that was 33% higher than determined theoretically. This phenomenon is clearly due to Hall-Petch strengthening where the finer tungsten grains lead to strengthening [21] of the matrix.

4.1.4. Tungsten feedstock containing 5.0wt% copper

1µm tungsten powders were mixed with 5.0wt% copper in the manufacture of sample 21. The purpose of this addition was to increase the amount of copper infiltrant within the final product by means of adhesive forces that draw the infiltrating front of copper up further when it came into contact with copper reservoirs present within the tungsten matrix.

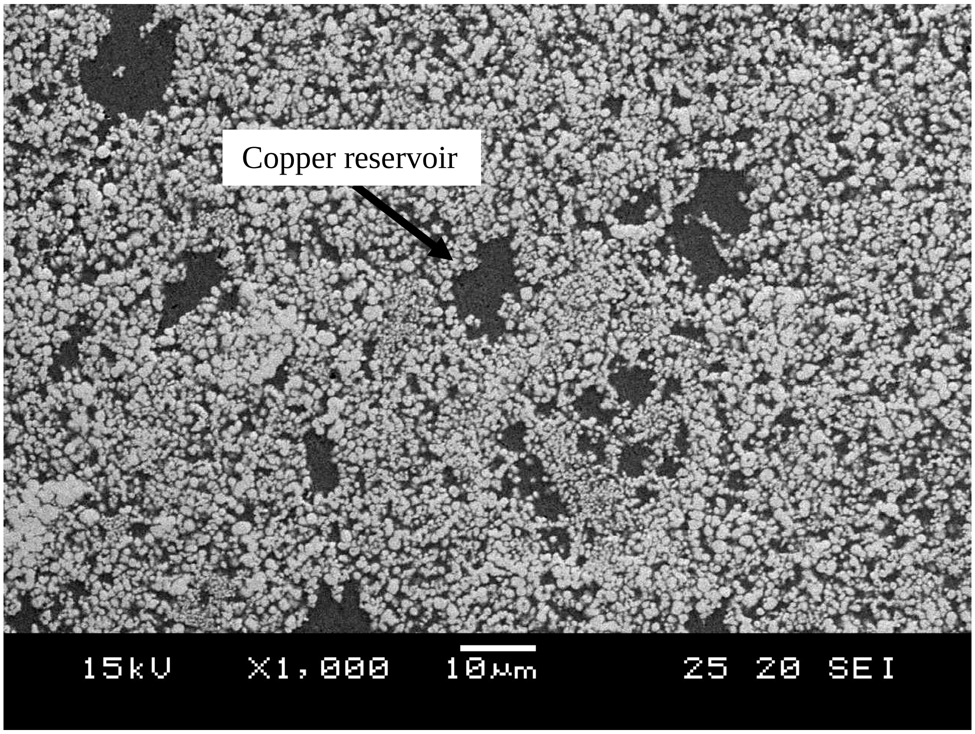

Figure 4.15: SEM micrograph showing a tungsten matrix with copper reservoirs left behind by the incorporation of 5.0wt% copper into the tungsten feedstock during mixing.

It can be seen from Figure 4.15 that bulk structural homogeneity was an issue with this sample. The tungsten matrix contained gaps that were formed from the presence of solid tungsten particles included during the mixing process. These “reservoirs” of copper were not able to shrink during the sintering phase and remained throughout the entire framework. While it is also theorized that smaller copper powders might result in smaller copper reservoirs, this could not be attempted due to material supply limitations.

Table 4.4: Summary of the properties of pure tungsten feedstock (sample 20) and tungsten feedstock mixed with 5.0wt% copper (sample 21). Both samples were sintered at 1150°C for 5 minutes.

Sample	Composition (wt% copper)	Mean hardness (H_V)	Mean conductivity (% IACS)	Mean CTE ($10^{-6}K^{-1}$)
20	34.62	198	26.21	13.21
21	40.43	161	29.33	14.81

From Table 4.4 above, lowering of the mean hardness, increase in CTE and increase in mean conductivity can be attributed to an increase in the amount of copper within the sample. The small disparity in CTE between sample 21 and 20 despite a 17% difference in copper content can be attributed to the presence of copper reservoirs. Assuming a linear law relationship for shrinkage, we will get the relation:

$$\alpha_{W-Cu} = V_{Cu}\alpha_{Cu} + V_W\alpha_W$$

Where $\alpha_{W\text{-}Cu}$ is the overall CTE, V_{Cu} and V_w are the volume fraction of copper and tungsten respectively and α_{Cu} and α_W are the CTE values for copper and tungsten respectively. With this in mind, we now consider Figure 4.16 below.

In the figure it can be seen that the central region (denoted by box 2B) has a greater volume fraction of copper as compared to the other eight boxes. As such, the expansion within the region 2B during heating will act to push the other eight regions uniaxially apart.

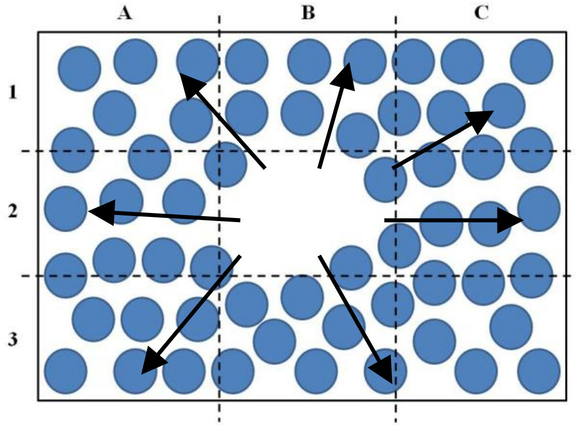

Figure 4.16: Diagram showing expansive effect copper reservoirs have on the composite. The arrows show the net force experienced by the expanding copper reservoir on that surrounding regions.

To determine the ability of the tungsten matrix to deformation, it is important then to establish the ability of the tungsten matrix in withstanding deformation. Standard tensile and three point bending tests attempted yielded inconclusive results as the tungsten porous matrix would fail suddenly and catastrophically.

Hence the Vickers hardness test was used to determine the yield strength of the matrix. The relationship between Vickers hardness and yield strength can be seen in Equation 4.14 below.

$$H_v = 3\sigma_y \qquad (4.14)$$

Where H_v is the Vickers hardness and σ_y is the yield strength of the tungsten matrix.

An uninfiltrated tungsten matrix produced using the same conditions as sample 10 and 14 was then analysed for its Vickers hardness and yielded a hardness of 198H_V (1942MPa) and a matrix yield strength of 647MPa.

Let us now consider the definition of young’s modulus as being:

$$E = \frac{\sigma_y}{\varepsilon} = \frac{\sigma_y}{\Delta B / B} = \frac{\sigma_y}{\alpha \Delta T} \tag{4.15}$$

Where E is the Young’s modulus, σ_y is the material stress, ε is the material strain, B is the original length of the material, α is the coefficient of expansion of the material and T is the temperature in Kelvin. Hence rearranging of Equation 4.15 will lead to

$$E\alpha\Delta T = \sigma_y \tag{4.16}$$

Using values of copper obtained from the Smithell’s metal reference handbook [22] and an operating temperature of up to 350°C from 25°C, the value of thermal stress induced by copper is 627MPa. This value is lower than the matrix yield strength of 647MPa obtained for the tungsten matrix.

Hence the tungsten matrix is able to sufficiently constrain the reservoir of copper during thermal expansion, resulting in an experimental CTE that is lower than that obtained by theoretical methods.

4.1.5. Investigating the viability of microwave sintering and infiltration

Microwave sintering of tungsten has been investigated and its ability to produce fine tungsten grains within pressed samples [23, 24] displayed a possible potential in producing fine grain tungsten copper MMCs otherwise not possible with standard sintering methods.

Under microwave, copper was able to melt and liquefy. However, the powdered compact of tungsten oxidized, forming oxides of tungsten which eventually sublimed. Oxides of tungsten are known to be volatile and have been shown to sublime rapidly above 750°C. [25]. It was also documented that above 1300°C, the rate of sublimation exceeds oxide formation, causing a continuous removal of tungsten (Figure 4.17). Upon inspection, it was also observed that the alumina crucible used in microwave sintering was coated with a yellow green powder that is shown in Figure 4.18. EDX analysis identified the coloured powder to be tungsten trioxide (WO_3).

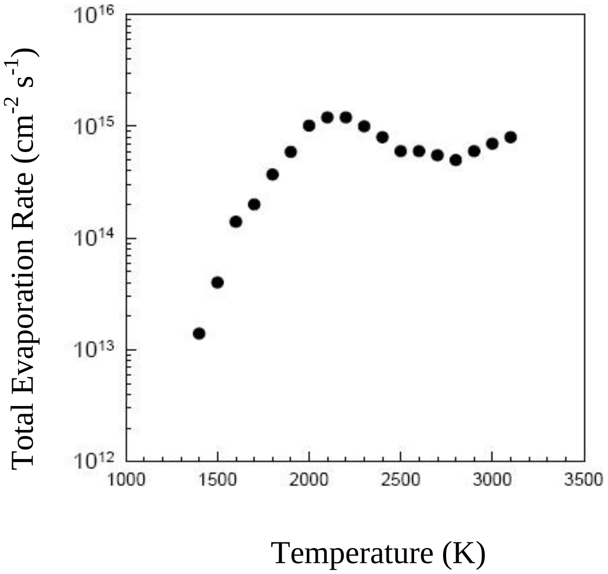

Figure 4.17: Evaporation rates of tungsten trioxide (WO_3) versus temperature [26]

Figure 4.18: Tungsten trioxide (WO_3) extracted from the sides of the crucible after microwave sintering.

The inverse heating profile synonymous to microwave sintering transfers energy directly to the sample and minimizes a significant amount of thermal losses. This efficiency provided a favourable path for the sublimation of the oxide. Bathing the setup in an inert or reducing environment would have proved more successful in producing meaningful results but given the limitations of the microwave furnace available, only open room atmosphere and pressure was available.

4.1.6. The effect of yttria addition on PM tungsten discs

Grain growth of micron and submicron tungsten even at moderate temperatures (1150°C) proceeds relatively quickly on the onset of thermal energy, despite the presence of pores that exert pore pinning pressure onto the tungsten grains [27]. An addition of a nano structured oxide at grain boundaries could have an effect in inhibiting grain growth by means of Zener pinning by an oxide phase [28].

From Figure 4.19 it can be seen that without yttria (samples 22 and 26), extensive densification was observed in samples produced by both 100nm and 1µm tungsten powder. However, when 2.0wt% yttria was added (sample 23 and 27), the samples showed a homogenous pore distribution throughout the samples. For the samples with powder size 100nm doped with 4.0wt% yttria (sample 24), abnormal grain growth was seen. This was not observed in the 1µm tungsten counterpart (sample 28).

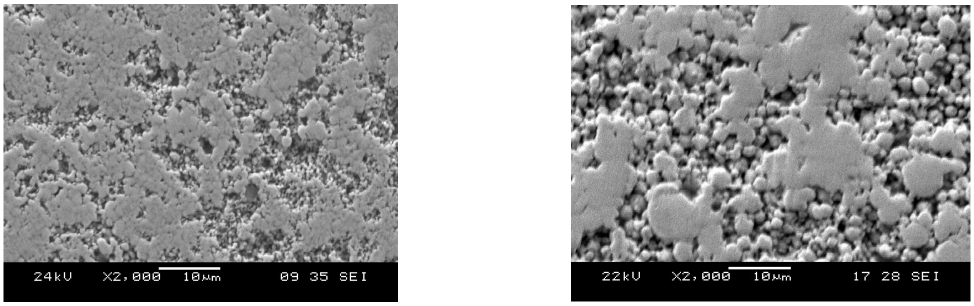

Sample 22 (100nm W-0% Y_2O_3) Sample 26 (1µm W-0% Y_2O_3)

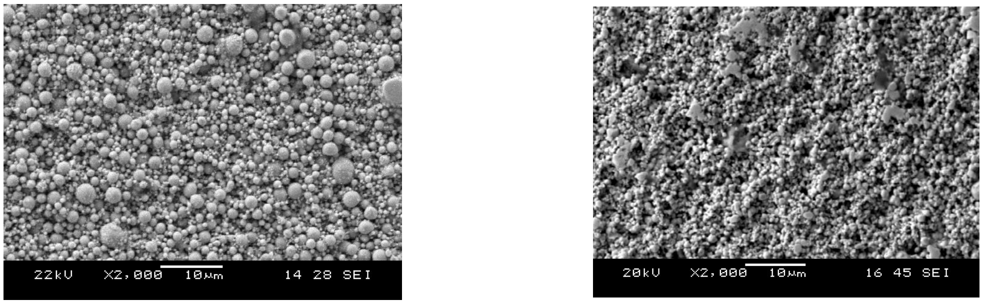

Sample 23 (100nm W-2.0% Y_2O_3) Sample 27 (1µm W-2.0% Y_2O_3)

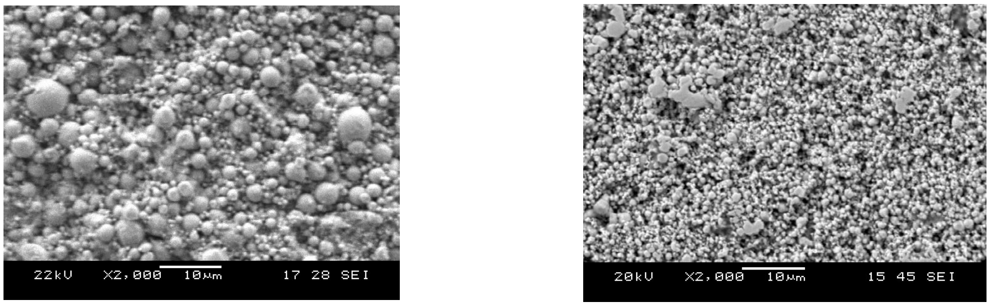

Sample 24 (100nm W-4.0% Y_2O_3) Sample 28 (1µm W-4.0% Y_2O_3)

Figure 4.19: Microstructure of pressed tungsten samples with varying starting powder sizes and yttria additive quantities.

Growth in tungsten at the 4.0wt% yttria level for 100nm tungsten can be attributed to grain growth of yttria at higher concentrations. This observation was also observed by Itoh *et al* [29]. At 4.0wt%, the high concentration of dispersed yttria within the sample was able to contact adjacent yttria particles. These particles would then grow into larger yttria grains that were unable to exert sufficient pinning pressure on the relatively small tungsten grains according to the following equation:

$$p_s = \frac{F_v \gamma}{r} \tag{4.17}$$

The equation above shows the inverse relationship of zener additive particle size, r on pinning pressure, P_s. where F_v is the force acting on the particle-boundary interface, and γ is the surface energy per area [9]. Hence as the yttria particles grow in size (increased r), a decreased pinning pressure (P_s) results.

On the other hand, the total pinning pressure of the larger yttria grains was still able to inhibit the growth of 1µm tungsten particles and resulted in grain growth being inhibited in the latter.

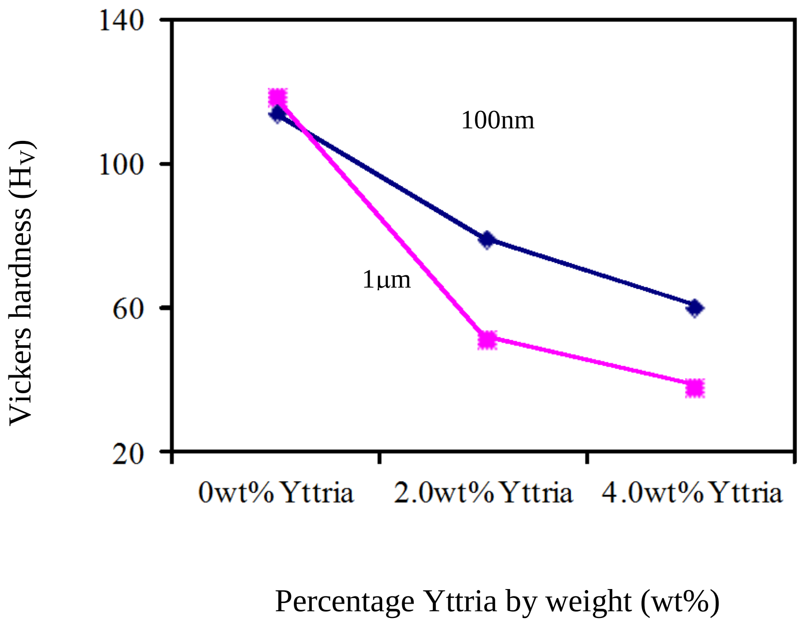

Figure 4.20. Vickers hardness values against amount of yttria addition for the sintered tungsten pressed using PM methods for 1µm and 100nm tungsten powders.

Hardness levels for samples produced without yttria were relatively constant at approximately 116H_V. The drop in hardness with addition of yttria is related to porosity throughout the bulk sample which will inadvertently lead to a reduction in its ability to withstand deformation due to an increase in the number of stress concentrators and an overall reduction in material. Drop in hardness with increased yttria addition is also a result of yttria particles impinging at tungsten grain boundaries. The pinning pressures against the boundaries serve to separate them, reducing the force required to deform the bulk by means of grain boundary separation. Due to only initial stage sintering being present, the yttria grains impinging against adjacent tungsten powders reduces the force required to separate them, lowering the amount of force needed to deform the matrix and hence lowering its hardness.

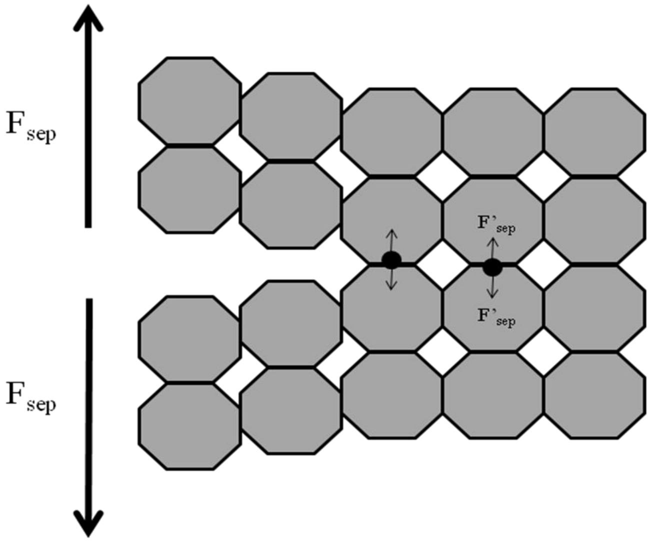

Figure 4.21: Diagram showing a zipper-like effect on a tungsten matrix when subjected to indentation. F_{sep} shows the separation force caused by the indentation while F'_{sep} shows the force on adjacent tungsten grains caused by the presence of impinging yttria grains.

It was concluded that the optimum value of yttria addition to tungsten to minimize grain growth is at the 2.0wt% level. Although pure tungsten matrices were superior in terms of matrix hardness and strength, the submicron structures of matrices formed with a 2.0wt% addition of yttria ensured greater homogeneity, greater bulk porosity (which would translate to greater infiltrate volumes in the finished MMC) and smaller grain sizes that would serve to strengthen subsequent infiltrated metal matrix composites by means of the Hall-Petch relation.

PIM tungsten feedstock doped with 2.0wt% yttria was then formulated, injection moulded and subjected to copper infiltration at 1150°C for 5 minutes. A comparison of the properties of this MMC with its non doped counterpart can be seen in Table 4.5 below.

Table 4.5: Properties of pure tungsten feedstock (sample 20) and tungsten feedstock mixed with 2.0wt% yttria (sample 33). Both samples were sintered at 1150°C for 5 minutes.

Sample	Composition (wt% copper)	Mean hardness (H_V)	Mean conductivity (% IACS)	Mean CTE ($10^{-6}K^{-1}$)
20	34.62	198	26.21	13.21
33	34.33	215	24.21	13.54

Composition, conductivity and CTE are comparable for both sample 20 and 32. With yttria's CTE of $8.1x10^{-6}K^{-1}$differing significantly from that of tungsten ($4.5x10^{-6}K^{-1}$) and copper ($16.5x10^{-6}K^{-1}$).The higher hardness of sample 33 as compared to sample 20 can be attributed to additional CTE mismatches experienced by the MMC with the presence of yttria.

4.1.7. Studies on tungsten-silver MMCs

With the success of copper as an infiltrant in forming tungsten copper MMCs by PIM, another commonly used metal in making tungsten based MMCs, silver, was also explored.

Despite its higher price, silver is commonly used for a number of current applications [30, 31] where it’s superior conductivity over copper results in lower thermal losses. The melting point of silver is also lower than that of copper, opening the avenue for lower processing temperatures, shorter manufacturing cycles and finer tungsten grains. All three samples were debinded at 450°C for one hour and subsequently heated to 1150°C and held for five minutes before cooling. The entire heat cycle was conducted in a hydrogen environment. While sample 30 and 31 consisted of 1µm and 100nm tungsten powder matrices respectively, sample 32 had 2.0wt% of yttria added to the tungsten powder during feedstock preparation to act as a grain growth inhibitor.

SEM analysis (Figure 4.22 below) showed abnormal grain growth in sample 31, the sample produced using 100nm tungsten powders. Comparing sample 30 and 32, samples produced using 1µm tungsten powders, it was observed that smaller, more uniform and discreet tungsten grains were present in sample 32 where yttria was used as a dopant.

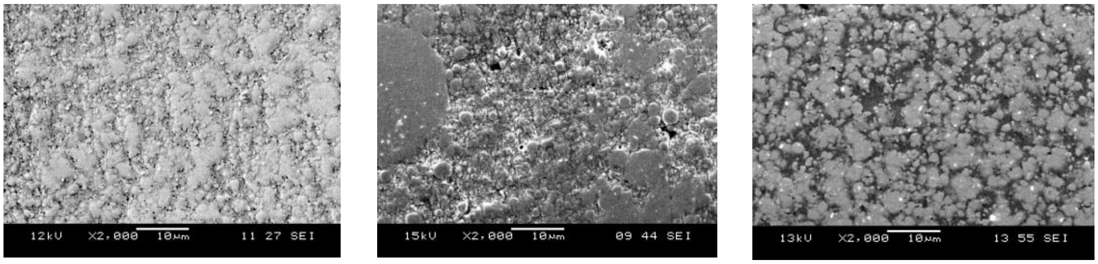

Figure 4.22: SEM micrographs showing from left to right, microstructures of samples 30, 31 and 32.

SEM analysis also displayed the obvious presence of pores throughout the entire bulk of all three samples. Porosity associated with the solidification of molten metals can be attributed to a variety of reasons.

Shrinkage pores are a result of molten metal cooling too rapidly within a matrix. When a liquid phase solidifies and shrinks, its volume decreases. Due to the presence of a secondary matrix which hinders the translation of mass during the solidification process, cavities are formed [13]. High cooling rates prevent cavities from closing before solidification, resulting in pores. The pores formed from shrinkage are elongated and non-spherical.

Gaseous pores are smooth pores formed through the evolution of gases during the solidification process. As a metal melt solidifies, gas is precipitated as a result of the lowering of gases solubility in the metal. Pores of this nature are spherical.

A third possibility in the formation of pores is that of incomplete infiltration. This can be due to lack of infiltrant or lack of time allocated to the infiltration process. Pores of this nature are non spherical and usually agglomerate at regions furthest away from the origin of infiltration.

It was observed that the pores within the samples were rounded and adhered to the tungsten matrix, characteristic of gaseous pores. Although hydrides of silver have not been observed in earlier studies, the solubility of hydrogen in silver has been reported [32]**.** During the solidification of silver, solubility of atomic hydrogen within silver decreases. This results in the evolution of hydrogen from within the matrix as a gas. Given the low viscosity of silver at 1150°C (2.96mNsm^{-2} for silver and 3.96mNsm^{-2} for copper), the partial pressure of the evolved hydrogen gas is sufficient enough to produce discernible gaps in the silver matrix.

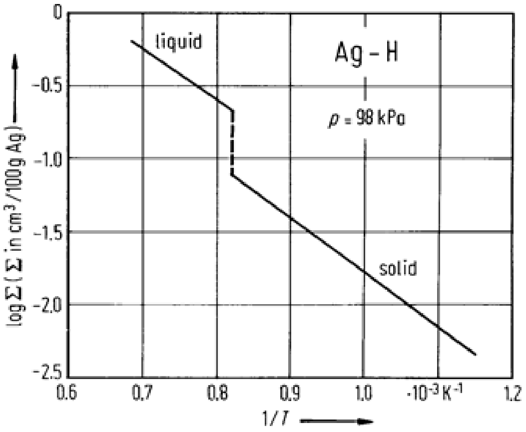

Figure 4.23: Graph showing the solubility of hydrogen gas in silver at 98 kPa.

Table 4.6: A comparison between theoretical and experimental values of hardness, conductivity and CTE for samples 30, 31 and 32.

		Experimental			Theoretical		
Sample	Composition (wt% silver)	Hardness (H_V)	Conductivity (% IACS)	CTE ($10^{-6}K^{-1}$)	Hardness (H_V)	Conductivity (% IACS)	CTE ($10^{-6}K^{-1}$)
30	36.41	133	51.02	15.10	190	66.34	10.65
31	28.74	153	42.30	14.31	217	60.33	9.60
32	37.53	127	53.49	13.03	173	61.68	10.69

Lower values of conductivity and higher values of CTE as compared to theoretical values are attributed to reasons cited in 4.1.2.

Lower values of experimental Vickers hardness as opposed to that predicted by theoretical values was however not in line with the explanations expounded in 4.1.2. The two main reasons for the drop in hardness would be firstly, the presence of gaseous pores throughout the bulk sample which reduced the overall material density and secondly the presence of yttria particles impinging against adjacent tungsten grains. The yttria particles (as explained in section 4.1.6) serve to pushing the grains in the tungsten matrix apart, leading to a lowering in overall hardness.

4.1.8. Joining of tungsten matrices in forming an MMC

This section will cover the joining of two adjacent tungsten matrices during the infiltration process. This observation was not hypothesized but showed immense potential for commercialization due to its repeatability and ease of implementation.

Sample 1 MMCs were produced in three orientations with the position of the tungsten matrix relative to the copper layers. All three set ups were debinded at 450°C for one hour, pre-sintered at 700°C for one hour and finally infiltrated/sintered at 1250°C for another hour. The entire process was done in a hydrogen reducing environment. The orientations can be seen clearly in Figure 4.24 below.

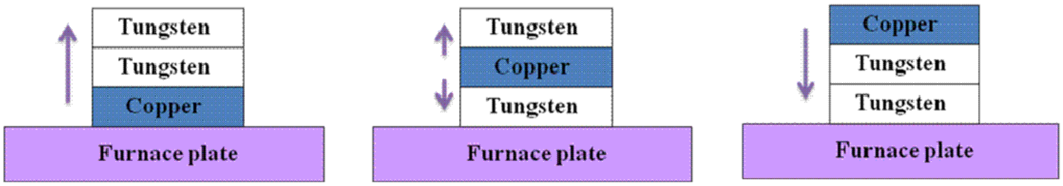

(i) (ii) (iii)

Figure 4.24: The three setups that were tested in the joining of two tungsten preforms to produce singular tungsten copper MMCs from left (i) copper below, (ii) copper in between, and (iii) copper on top. The arrow shows the direction of copper infiltration.

SEM analysis revealed presence of voids in samples produced using setup (ii) and (iii) (Figure 4.25 below), which was due to the presence of encapsulated gases within the MMCs that were unable to release themselves during infiltration. Molten copper flowing upwards in the case of setup (i) rises in fronts, resulting in a systematic expulsion of gases. This process is represented diagrammatically in Figure 4.26 below.

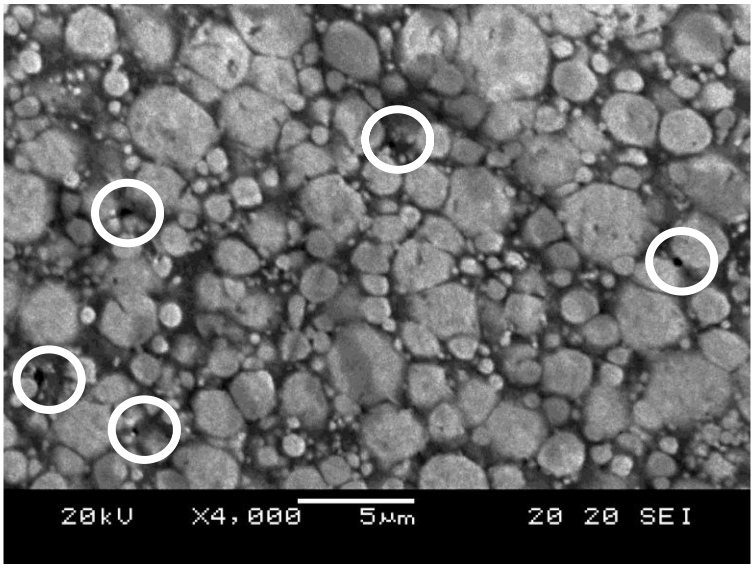

Figure 4.25: SEM photograph of the tungsten copper MMC showing voids (circled) present due to incomplete infiltration.

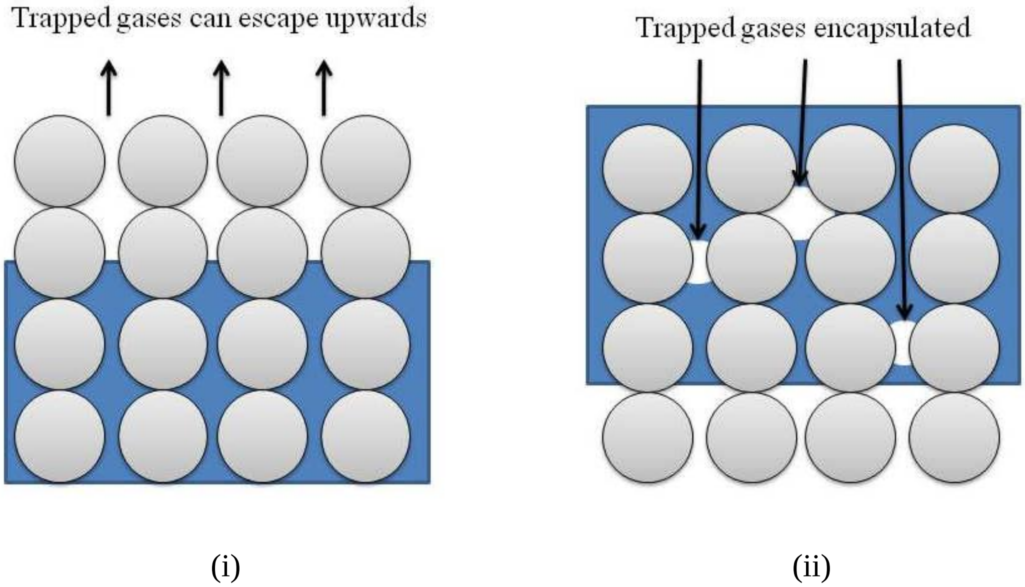

(i) (ii)

Figure 4.26: Diagram showing (i) infiltration of copper upwards into a tungsten matrix where no gases are trapped and (ii) infiltration of copper downwards into a tungsten matrix that can lead to encapsulation of gases.

Further examination of the samples produced using set up (i) was conducted. Both optical and SEM analysis (Figure 4.27 and 4.28 respectively) at the joining interface of the two matrices showed no discernable distinction.

Figure 4.27: Optical microscopy photo showing the joining interface at a magnification of 100x. The white arrow points to the location of joining interface line. The dark regions are tungsten while the lighter regions is copper

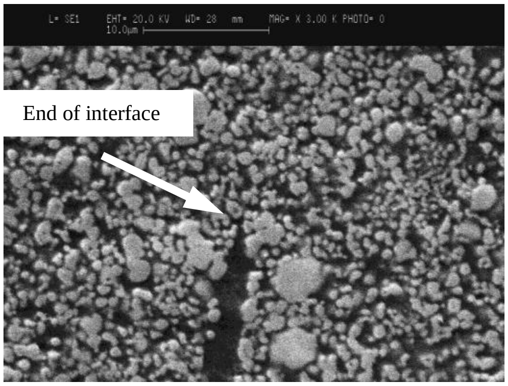

Figure 4.28: SEM micrograph showing the joining interface at magnification of 3000x. The white arrow points to the location where the interface terminates.

Examination of hardness and composition were conducted along the joining interface and along two parallel lines 1mm above and below the interface as shown in Figure 4.29 below.

Figure 4.29: Location of areas subject to composition and Vickers hardness testing.

Compositional analysis using Electron Dispersive X-ray (EDX) analysis showed a slightly higher copper content noted at the interface as compared to the regions above and below the interface. However, all values were still within 5.0% of each other (Figure 4.30).

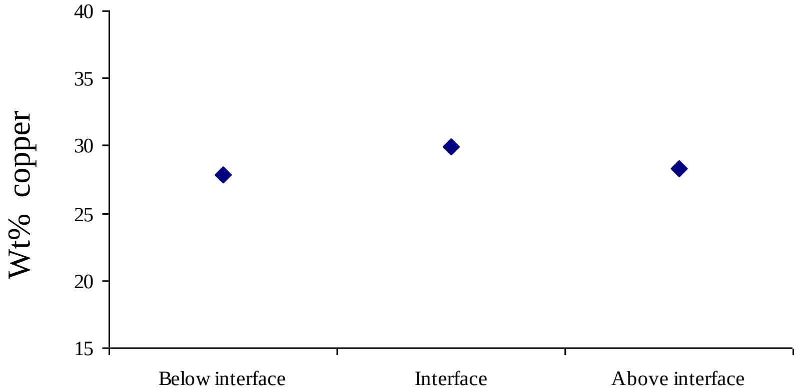

Figure 4.30: Graph showing the percentage weight of copper present at the interface and at lines 1mm parallel to the interface as obtained by EDX analysis

Vickers hardness testing yielded results similar for indentations done at the interface and 1mm below and above the interface (Figure 4.31). The difference in hardness was less than 4.0% for the readings for the three locations.

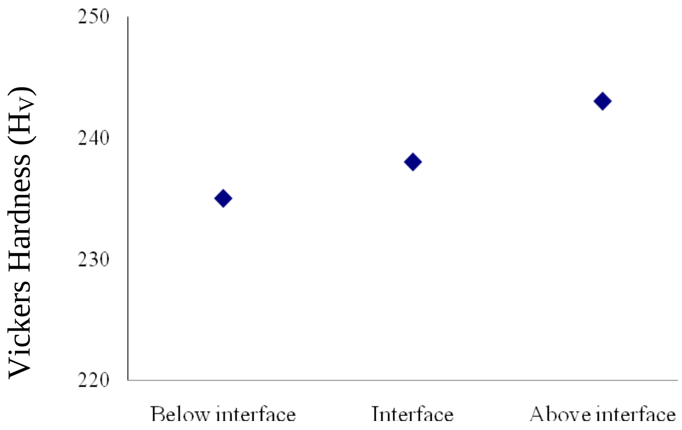

Figure 4.31: Graph showing the experimental Vickers hardness at the interface and at lines 1mm parallel to the interface as obtained by Vickers hardness indentation tests.

Upon debinding, the preform consisted of tungsten grains that were held together by a combination of lightly sintered necks as a result of initial stage sintering [9] and forces of attraction formed by interactions between minute particles as set forth by Newton's Law of Gravitation [33].

At 1150°C, the copper portion melted and flowed up through the pores of the porous matrix by means of capillary and displacement forces [3]. Fluid flow resulted in shear forces being imposed onto the tungsten grains, dragging particles in the direction of flow. The force imposed on each particle by the molten copper moving up in fronts can be generalized as being analogous to Stokes's drag;

$$F_{drag} = 6\pi\eta r v \tag{4.18}$$

Where F_{drag} is the drag force, η is the viscosity of the molten copper, r is the equivalent powder grain radius and v is the velocity of the copper flow relative to the tungsten matrix. Given the unpressurized nature of the process, Reynolds number for the laminar flow of molten copper through the pores of the preform skeleton can be taken to be less than unity ($Re < 1$).

Translation of tungsten grains into the interface gap by means of stokes drag (Figure 4.32, 4.33) is produced by the flowing copper. This translation serves to move the upper layer of tungsten grains of the lower preform into the interface.

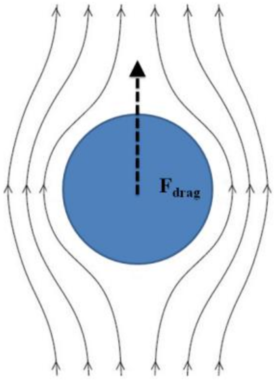

Figure 4.32: Effect of laminar fluid flow has on lifting a spherical particle. The solid lines depict laminar flow while the dashed arrow indicates the direction of lift.

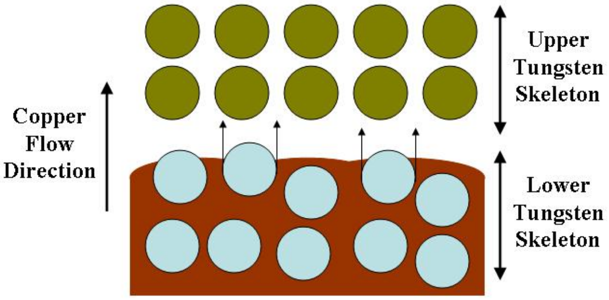

Figure 4.33: Illustration showing the effect of drag forces on the topmost layer of spheres of the lower skeleton.

This lifting force is opposed by three main forces; the weight of the individual grain, the gravitational force that acts upon it due to its proximity with other particles and finally the sinter bond strength of the necks.

The force acting on a tungsten particle due to the effect of earth's gravitation on its mass is expressed as:

$$F_{weight} = mg$$

Where m is the mass of the tungsten particle and g is the acceleration due to gravity. We can also re-express the particle's mass as a function of its particulate radius (r) and density (ρ_w) where:

$$m = \frac{4}{3}\pi r^3 \rho_w$$

Hence with this derived term we can express the function of force to be:

$$F_{weight} = \frac{4}{3}\pi r^3 \rho_w g \qquad (4.19)$$

The force contributed by the intra particle gravitation can be derived based on Newton's law of gravitation. The force of attraction acting on two masses (m_1 and m_2) at a distance of $2r$ apart can be expressed as:

$$F_{gravitation} = \frac{Gm_1 m_2}{(2r)^2}$$

Where G is the gravitational constant. As the powders used are assumed to be of equal size and mass, $m_1 = m_2 = m$, Hence:

$$F_{gravitation} = \frac{Gm^2}{4r^2} = \frac{G}{4r^2}\left(\frac{4}{3}\pi r^3 \rho_w\right)^2 = \frac{4}{9} r^4 G \pi^2 \rho_w{}^2 \qquad (4.20)$$

The sintering pressure [34] contributed by sintering strength at the necks has been calculated to be:

$$\sigma_{\text{sinter bond pressure}} = 2\left(\frac{J}{2r}\right)^2 \sigma_y V_f \frac{N}{\pi}\left(\frac{J}{2r}\right)^2$$

Where, $\sigma_{sinter\ bond\ pressure}$ the sinter bond pressure, is the pressure required to break a sinter bond, σ_y is the inherent material strength, N is the coordination number, V_f is the fractional density of the preform and J is the neck diameter.

The force acting on the grains due to necking is expressed as:

$$F_{\text{sinter bond strength}} = \left(\sigma_{\text{sinter bond pressure}}\right)\pi\left(\frac{J}{2}\right)^2$$

Where $\pi\left(\frac{J}{2}\right)^2$ is the cross sectional area of the sintered neck. Hence the sintering force can be expressed as:

$$F_{\text{sinter bond strength}} = 2\left(\frac{J}{2r}\right)^2 \sigma_y V_s \frac{N}{\pi}\left(\frac{J}{2r}\right)^2 \pi\left(\frac{J}{2}\right)^2$$

$$= \left(\frac{\sigma_y V_s N J^6}{32 r^4}\right) \qquad (4.21)$$

The forces contributed by both the sintered necks and inter particle gravitational forces act diagonally and have to be resolved into vertical components. To simplify this calculation we consider the packing of tungsten grains to be of a close packing [35] arrangement as can be seen in Figure 4.34.

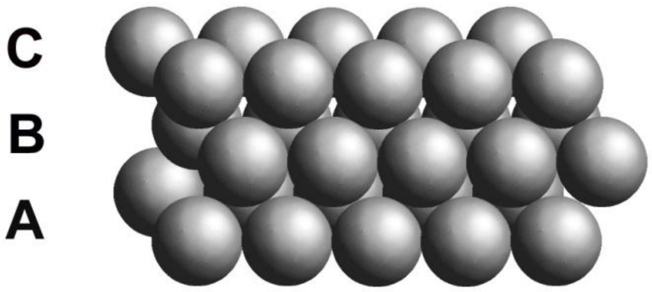

Figure 4.34: Illustration showing close packing of spheres representing the preform structure.

From Figure 4.34 above it can be seen that each sphere is influenced by three other spheres from the bottom layer. The forces holding it is resolved as lines of force intersecting the contact points and centres of all four spheres. This results in the formation of a tetrahedron where the affected sphere has its centre at the apex of the tetrahedron while the three influencing spheres have their centres at the basal vertices. The three diagonal edges represent vectorally lines of forces by which the forces of inter particular gravitational attraction and sinter bond act. The vertical height of the tetrahedron is analogous to the vector of the resolved vertical force. In this model the particle horizontally adjacent to the affected particle is ignored as the lines of action fall within the horizontal plane and do not have a vertical component.

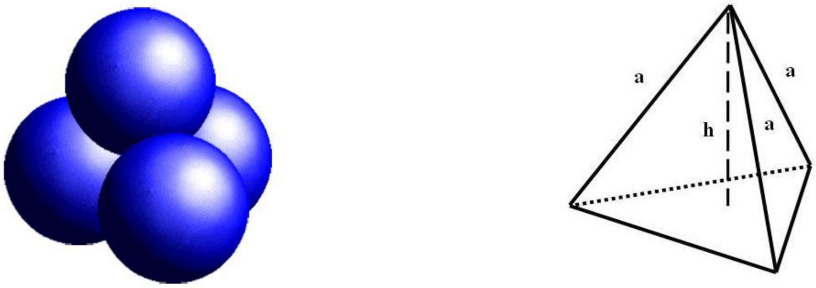

(i) (ii)

Figure 4.35: Figure showing (i) view of a sphere in a close packing arrangement showing its coordination with three lower spheres in the adjacent layer. (ii) tetrahedron formed by joining the corresponding centres of the four spheres. The edges of the tetrahedron represent the lines of force acting between the three packed spheres.

To determine the height of the tetrahedron in Figure 4.35(ii), we consider a plane perpendicular to the base that intersects the apex (*z*) and a basal vertex (in this case *x*). A projection of this plane can be seen in Figure 4.36 below.

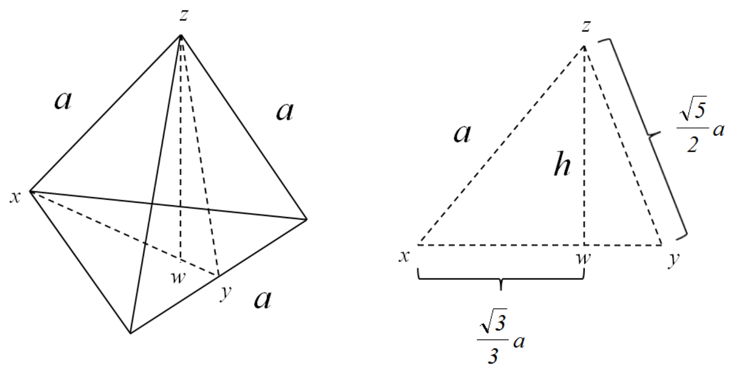

Figure 4.36: Diagram showing on the left, a tetrahedron with a plane perpendicular to the base intersecting the apex and one basal vertex; and on the right, a projection of the plane used in determining the height, *h*, of the tetrahedron.

By means of Pythagoras theorem, we can determine the length of the base of the plane where,

$$xy = \sqrt{\left[a^2 - \left(\frac{a}{2}\right)^2\right]} = \frac{\sqrt{3}}{2}a$$

As the base of the tetrahedron is an equilateral triangle where the distance of a vertex to its circumventer is given as two-thirds of the length of its sides, the length of *xw* can be determined to be;

$$xw = \frac{2}{3}xy = \frac{2}{3}\left(\frac{\sqrt{3}}{2}a\right) = \frac{\sqrt{3}}{3}a$$

Hence with both length *xw* and the *xz*, we can determine the height *wz* (*h*) to be

$$wz = \sqrt{xz^2 - xw^2} = \sqrt{a^2 - \left(\frac{\sqrt{3}}{3}a\right)^2} = \frac{\sqrt{6}}{3}a$$

Hence from Figure 4.36, as $\frac{\sqrt{6}}{3}a = h$ to resolve the forces in a vertical direction, we will need to multiply the diagonal forces by a multiple of $\frac{\sqrt{6}}{3}$.

To drag a layer of grains into the interface, the equation has to fulfil the relation:

$$0 < F_{drag} - F_{weight} - N\left[\frac{\sqrt{6}}{3}\left(F_{gravitaion} + F_{Sinter\ bond\ strength}\right)\right]$$

As we consider only the gravitational and sinter strength forces having a component in the vertical direction and not in the horizontal, the coordination number of the grain, N, can be reduced to a value of three. Therefore;

$$0 < 6\pi\eta rv - \frac{4}{3}\pi r^3\rho_w g - 3\left[\frac{\sqrt{6}}{3}\left(\frac{4}{9}r^4 G\pi^2{\rho_w}^2 + \left(\frac{\sigma_y V_s NJ^6}{32r^4}\right)\right)\right] \tag{4.22}$$

As the temperatures used are low relative to the absolute melting point of tungsten and presintering time is short, we can assume that that the neck diameter, $J \rightarrow 0$, and the equation can be further simplified to:

$$0 < 6\eta v - \frac{r^2\rho_w}{9}\left(12g + 4\sqrt{6}Gr\pi\rho_w\right) \tag{4.23}$$

As molten copper moves into the interface, liquid bridges are formed between the two opposing layers by means of capillarity and adhesive forces. Figure 4.37 shows a liquid bridge and two spheres:

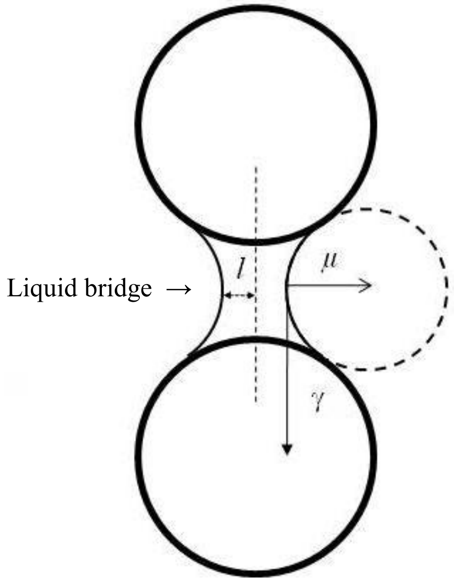

Figure 4.37: Diagram showing the two spheres and a liquid capillary neck. With *l* being the neck radius at its thinnest point, γ is the surface tension at the liquid-vapor interface and *μ* being the radius of curvature of the liquid meniscus.

Heady and Cahn [36] theorized the force acting on the top grain downward to be quantified as;

$$F_{capillary} = 2\pi l\gamma - \pi l^2 \gamma \left(\frac{1}{l} - \frac{1}{\mu} \right)$$

As with Equation 4.22, we need to take into account the effect of interparticle gravitational attraction and weight. Hence the equation takes the form;

$$0 < F_{capillary} + F_{weight} - N\left[\frac{\sqrt{6}}{3} \left(F_{gravitaion} + F_{Sinter\ bond\ strength} \right) \right]$$

Also adopting the assumption that $X \rightarrow 0$, hence $F_{sinter\ bond\ strength} \rightarrow 0$, and,

$$0 < l\gamma + \frac{l^2\gamma}{\mu} + \frac{4}{3} r^3 \rho_w g - \frac{4\sqrt{6}}{9} r^4 G\pi {\rho_w}^2 \qquad (4.24)$$

The resulting effect of a capillary bridge causes the grains at the top of the interface to be pulled downwards into the interface, as well as a smaller, less pronounced reaction force that acts to raise the lower grains up into the boundary. (Figure 4.38).

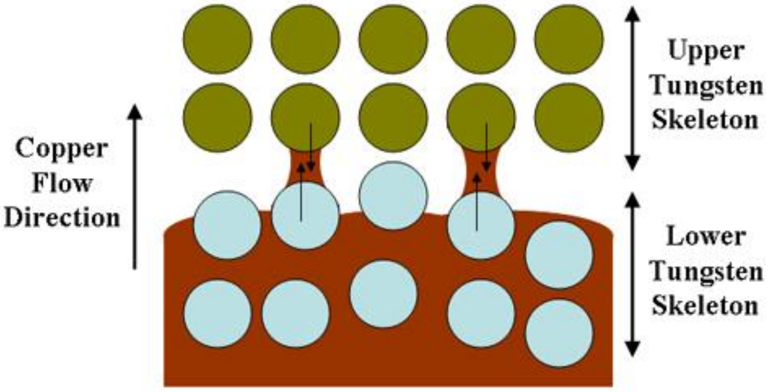

Figure 4.38: Illustration showing the influence capillary effect has in pulling both tungsten skeletons together.

Further flow of the molten copper into both preforms eventually leads to a fully saturated system comprising of tungsten grains in molten copper. This collection of solid particles in an incompressible fluid is subject to Brownian motion [37, 38]. Soaking at 1150ºC, Brownian motion serves as a vehicle by which the relatively mobile tungsten grains at the interface rearrange to configurations that possess lower grain boundary energies. [39, 40]. This effect has been observed in other research [41, 42] and leads to an overall homogenizing of the system at the interface.

Equations 4.23 and 4.24 have been derived to determine the susceptibility of joining metal matrix composite systems that can be processed using the press-sinter-infiltrate route. It is also important to note that there is a directly proportional relationship between susceptibility of joining and the magnitude of the values obtained in Equations 4.23 and 4.24.

From Equations 4.23 and 4.24, we are able to determine the theoretical range of tungsten grain sizes suitable for copper and silver joining through the infiltration process. For stoke's drag to be applicable, Reynolds number < 1, Hence,

$$1 > Re = \frac{2r\rho_{liquid}v}{\eta}$$

Where ρ_{liquid} is the density of the infiltrating liquid metal. Rearranging we get,

$$v < \frac{\eta}{2r\rho_{liquid}} \tag{4.25}$$

Rearranging Equation 4.23, we get the form

$$v > \frac{r^2\rho_w}{54\eta}\left(12g + 4\sqrt{6}Gr\pi\rho_w\right) \tag{4.26}$$

Solving Equations 4.25 and 4.26 simultaneously, given values of ρ_w = 1.93 x10^{4}kg/m^3, ρ_{liquid} = 8.00 x10^{3}kg/m^3 and η = 4.00 x10^{-3}Ns/m^2 for copper and G = 6.67 x10^{-11}m^3/kgs^2, π = 3.14 and g = 9.81m/s^2 [22, 43] we obtain the final quartic equation:

$$0 > 3.54r^4 + 10516r^3 - 2.5\times10^{-7} = R_{threshold} \tag{4.27}$$

Where positive values of $R_{threshold}$ indicate the range of solutions for r where Equation 4.27 holds true. We shall limit the scope of our analysis to metal powder sizes (r <50µm) that are commonly used in powder metallurgy and injection moulding. Hence by solving Equation 4.27 graphically for r < 50µm it can be seen from Figure 4.39 that only tungsten radii of less that 29µm and 27µm satisfy Equation 4.23 for copper and silver respectively.

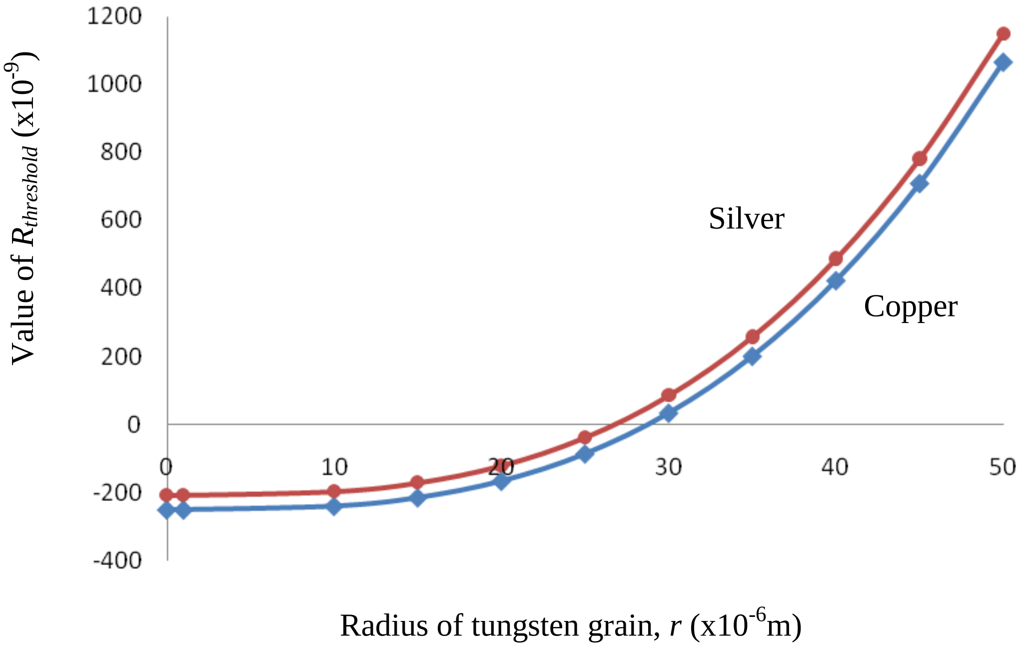

Figure 4.39: Values of $R_{threshold}$ against tungsten grain size, r. This plot is used to determine graphically the range of tungsten grain sizes that fulfil Equation 4.23.

For excess liquid used in infiltration, the liquid capillary bridge can be simplified to a cylinder linking both spheres, resulting in the value of $\mu \to \infty$ and $l \to r$ (Figure 4.40 below). Substituting into Equation 4.24 the range of tungsten grain sizes obtained from Figure 4.39, where the surface tension of liquid copper and silver, γ, is 1.303N/m and 0.966N/m respectively [12], we obtain positive values within the range $0 < r < 29$µm, hence satisfying both conditions for successful joining for the given system.

The above relations derived in this research have guided further experimental work with respect to the joining of the tungsten silver dual metal system. Tungsten copper systems where the tungsten powder sizes were as small as 100nm were also conducted with relative success. Also, being a purely mechanical process whereby the miscibility of the metal phases is not an issue, this system has the added advantage of being applied to form composite sandwiches where a common liquid infiltration phase exists during the manufacturing process. The tungsten copper/molybdenum copper/tungsten copper sandwich is one such sandwich that could be produced using this technique.

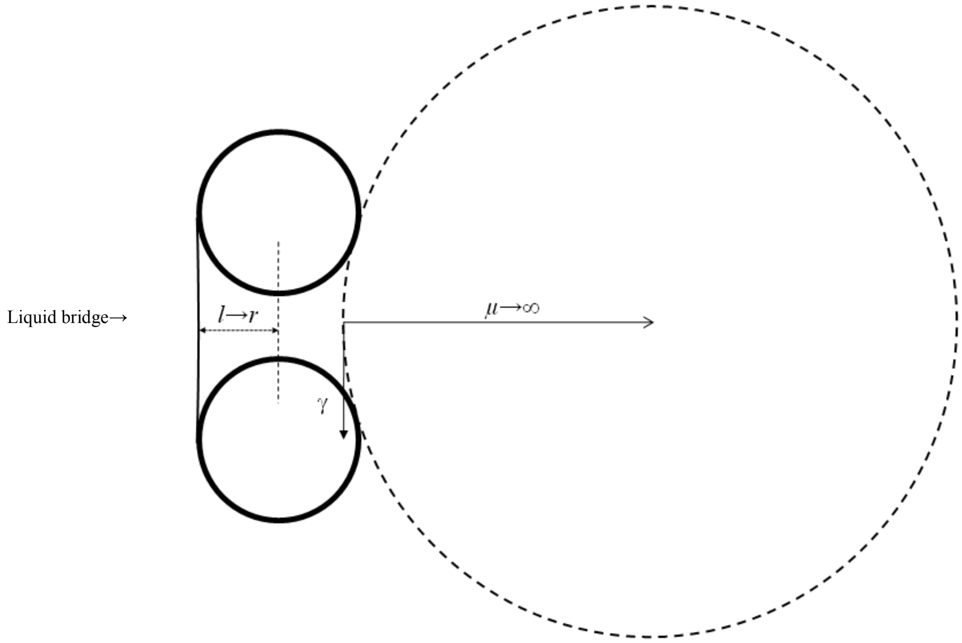

Figure 4.40: Excess liquid at a liquid bridge leading to a smoothened meniscus where meniscus radius $\mu \to \infty$ and neck radius $l \to r$

References

1. Wilcox, C.D., et al., *ImageTool Version 3.0*, U.o.T.H.S.C.a.S. Antonio, Editor. 2002.
2. Zouvelou, N., X. Mantzouris, and P. Nikolopoulos, *Interfacial energies in oxide/liquid metal systems with limited solubility.* International Journal of Adhesion & Adhesives, 2007. **27**: p. 380-386.

3. Ho, P.W., Q.F. Li, and J.Y.H. Fuh, *Evaluation of W–Cu metal matrix composites produced by powder injection molding and liquid infiltration* Materials Science and Engineering: A, 2008. **485**(1-2): p. 657-663

4. Chieh, C., *The Archimedean truncated octahedron, and packing of geometric units in cubic crystal structures.* Acta Crystallographica, Section A (Crystal Physics, Diffraction, Theoretical and General Crystallography), 1979. **A35**(6): p. 946-952.

5. Kaptay, G., *Interfacial criteria for stabilization of liquid foams by solid particles.* Colloids and Surfaces A: Physicochem. Eng. Aspects 2004. **230**: p. 67-80.

6. Challita, A., B. Chelluri, and D.P. Bauer, *Minimizing Non-arcing Contact Material Deposition on Rails.* IEEE Transactions on Magnetics, 1995. **31**(1): p. 134-137.

7. Eremenko, V.N., R.V. Minakova, and M.M. Churakov, *Solubility of tungsten in copper-nickel melts.* Powder Metallurgy and Metal Ceramics, 1977. **16**(4): p. 283-286.

8. Rahaman, M.N., *Ceramic Processing and Sintering*. 2nd ed. 2003: CRC Press.

9. Kang, S.J.L., *Sintering: Densification, Grain Growth, and Microstructure*. 2005: Butterworth-Heinemann.

10. Ratke, L. and P.W. Voorhees, *Growth and Coarsening: Ostwald Ripening in Material Processing*. 2002: Springer.

11. Wang, W.S. and K.S. Hwang, *The Effect of Tungsten Particle Size on the Processing and Properties of Infiltrated W-Cu Compacts.* Metallurgical and Materials Transactions A, 1998. **29A**: p. 1509-1516.

12. Gale, W.F. and T.C. Totemeier, *Smithells Metals Reference Handbook*. 8th ed. 2003: Elsevier.

13. Fredriksson, H. and U. Akerlind, *Materials processing during casting*. 2006: Wiley.

14. Mantaux, O., E. Lacoste, and M. Danis, *Numerical prediction of microporosity formation during the solidification of a pure metal within a porous preform.* Composites Science and Technology, 2002. **62**: p. 1801–1809.

15. Chawla, K.K. and M. Metzger, *Initial dislocation distributions in tungsten fibre-copper composites* Journal of Materials Science, 1972. **7**(1): p. 34-39.

16. Tabor, D., *The hardness of metals*. 2000: Oxford University Press.

17. Lu, L., et al., *Ultrahigh Strength and High Electrical Conductivity in Copper* Science, 2004. **304**(5669): p. 422-426.

18. Srivastava, V.C. and S.N. Ojha, *Microstructure and electrical conductivity of Al-SiCp composites produced by spray forming process* Bulletin of Materials Science, 2005. **28**(2): p. 125-130.

19. Wiedemann, G. and R. Franz, *Ueber die Wärme-Leitungsfähigkeit der Metalle (German).* Annalen der Physik, 1853. **89**(8): p. 497-531.

20. German, R.M. and E. Olevsky, *Mapping the compaction and sintering response of tungsten-based materials into the nanoscale size range.* International Journal of Refractory Metals & Hard Materials, 2005. **23**: p. 294–300.

21. Callister, W.D., *Fundamentals of Materials Science and Engineering: An Integrated Approach*. 2nd ed. 2004: Wiley.

22. Gale, W.F., C.J. Smithells, and T.C. Totemeier, *Smithells Metals Reference Handbook*. 8 ed. 2004: Butterworth-Heinemann.

23. Jain, M., et al., *Microwave Sintering: A New Approach to Fine-Grain Tungsten-I.* International Journal of Powder Metallurgy, 2006. **42**(2): p. 45-52.

24. Jain, M., et al., *Microwave Sintering: A New Approach to Fine-Grain Tungsten-II.* International Journal of Powder Metallurgy, 2006. **42**(2): p. 53-57.

25. Lassner, E. and W.D. Schubert, *Tungsten: Properties, Chemistry, Technology of the Element, Alloys, and Chemical Compounds*. 1999: Springer.

26. Ghoniem, N.M. (1998) *High temperature oxidation of Tungsten and Molybdenum*. APEX study group meeting, The University of California at Los Angeles.

27. Novikov, V., *Grain growth and control of microstructure and texture in polycrystalline materials*. 1996: CRC Press.

28. Doherty, R.D., *Current issues in recrystallization: a review.* Materials Science and Engineering: A, 1997. **238**(2): p. 219-274.

29. Yoshiyasu, I. and I.Yutaka, *Strength Properties of Yttrium-Oxide-Dispersed Tungsten Alloy.* JSME international journal. Series A, Solid mechanics and material engineering, 1996. **39A**(3): p. 429-434

30. Leung, C.H. and H.J. Kim, *A Comparison of Ag/W,Ag/WC, and Ag/Mo Electrical Contacts.* IEEE Transactions on Components, Hybrids, and Manufacturing Technology, 1984. **7**(1): p. 69-75.

31. Leung, C.H. and P.C. Wingert, *Microstructure effects on dynamic welding of Ag/W contacts.* IEEE Transactions on Components, Hybrids, and Manufacturing Technology, 1988. **11**(1): p. 64-67.

32. Bagshaw, T. and A. Mitchell, *The Solubility of Hydrogen in Liquid Silver.* Transactions of the Metallurgical Society of AIME 1968(2): p. 343.

33. Cohen, I.B., *A Guide to Newton's Principia*. 1999: University of California Press.

34. German, R.M. *Strength Evolution in Debinding and Sintering*. in *3rd International Conference on the Science, Technology & Applications of Sintering*. 2003. State College, Pennsylvania: Penn State University Press.

35. German, R.M., *Powder Packing Characteristics*. 1989: Metal Powders Industries Federation.

36. Heady, R.B. and J.W. Cahn, *Analysis of the capillary forces in liquid phase sintering of spherical particles.* Metallurgical transactions, 1970 **1**(1): p. 185-189.

37. Wendel, J.G., *Hitting Spheres with Brownian motion.* The Annals of Probability, 1980. **8**(1): p. 164-169.

38. Doi, M. and M. Makino, *Motion of micro-particles of complex shape.* Progress in Polymer Science, 2005. **30**: p. 876-884.

39. Moldovan, D., et al., *Role of grain rotation during grain growth in a columnar microstructure by mesoscale simulation.* Acta Materialia, 2002. **50** p. 3397-3414.

40. Lu, P. and R.M. German, *Multiple grain growth events in liquid phase sintering.* Journal of materials science, 2001. **36**: p. 3385-3394.

41. Fang, Z.Z. and O.O. Eso, *Liquid phase sintering of functionally graded WC-Co composites.* Scripta materialia, 2005. **52**: p. 785-791.

42. Russel, W.B., *Brownian motion of small particles suspended in liquids.* Annual review of fluid mechanics, 1991. **13**: p. 425-455.

43. Gundlach, J.H. and S.M. Merkowitz, *Measurement of Newtons constant using a torsion balance with angular acceleration feedback.* Physics review letters, 2000. **85**: p. 2869-2872.

5. Conclusions

The focus of this doctoral study was to examine and establish a series of conditions by which tungsten copper MMCs could be manufactured using the PIM technique. Presented below is a summary of the achievements and findings of this study.

5.1. Conditions for the manufacture of tungsten copper MMCs

It was determined that for successful infiltration of copper to produce tungsten copper MMCs in a CM tube furnace, reducing hydrogen atmospheres were required at temperatures in excess of 1150°C. The reducing hydrogen environment prevented the formation of a tenacious oxide layer which impeded infiltration, while 1150°C was in excess of the melting point of copper. An infiltrating orientation where the tungsten portion was placed over the molten copper was preferred as the rising of molten copper upwards in fronts prevented the trapping of gases within the finished MMC.

Powder injection moulding was successfully used in the production of tungsten preforms. Use of powder injection moulding to produce bimetallic green parts of copper and tungsten by over moulding was also successful. The integration of the thermal debinding and sintering/infiltration cycles into one comprehensive heat cycle was also successfully implemented, significantly reducing furnace run times.

The ability to produce tungsten copper MMCs through the joining of two tungsten matrices was also demonstrated and this was deemed to be able to ease the manufacture of complex components whose net shape could not be injection moulded directly.

5.2. Effect of process variables on MMC properties

It was demonstrated that in general, a higher sintering/infiltration temperature resulted in higher hardness, lower CTEs and lower conductivities due to more extensive densification of the tungsten matrix which resulted in less open porosity for subsequent copper infiltration.

An average tungsten grain size of 2µm was produced when sintered for one hour. This was independent of starting tungsten powder sizes and sintering temperatures.

It was however noted that samples which were produced using 100nm tungsten powders displayed more extensive densification and also a presence of abnormal grains.

When sintering/infiltration times for samples using 100nm tungsten powders were reduced to 5 minutes at 1150°C, it was shown that tungsten grain sizes as fine as 500nm were produced with a higher CTE, conductivity, hardness and percentage copper as compared to its one hour counterpart. This change was due to less extensive densification of the tungsten preform upon sintering, and also the Hall-Petch phenomenon produced by the smaller grain sizes.

An addition of 5.0wt% of copper to the tungsten feedstock resulted in exceptionally high amounts of copper (40.43 wt% copper) in the final tungsten copper MMC and this was due to the presence of copper reservoirs formed within the MMC.

The addition of 2.0wt% of 30nm yttria as a Zener dopant resulted in tungsten grains as small as 200nm when added to feedstocks produced using 100nm tungsten powders. Subsequent infiltration of copper to tungsten matrices containing 2.0wt% yttria was also successful with no porosity detected.

Tungsten silver MMCs were also successfully synthesized using the method developed; however smooth pores were evident in the final microstructure. The smooth pores were due to the evolution of hydrogen gas resulting from a reduction in gaseous solubility during solidification.

5.3. Development of models to explain various phenomenon

A mathematical equation (Equation 4.8) was derived to predict the viability of infiltrating a porous matrix with a liquid. A second set of mathematical equations (Equations 4.23 and 4.24) were also derived to determine the viability of joining two porous bodies using the infiltration method to produce a single MMC.

A conceptual model (as shown in Figure 4.16) was developed to explain the lower than expected CTE values experienced by samples produced using tungsten feedstocks with 5.0wt% copper added.

Finally a physical model (Figure 4.21) was produced to explain the lowering of hardness values for pressed tungsten samples subjected to yttria doping.

5.4. Recommendation for future work

Due to the high cost of silver powder, work done on tungsten silver was limited. With the work done with copper, it is possible to translate the processes studied and developed into the tungsten silver context. Copper and silver both belong to group 11 in the periodic table of elements and possess one electron in their outermost valence shell. Elements within the same group display similar chemical properties and thus can be used in similar processes.

Microwave sintering in alternative environments other than air should also be studied further. While this was not possible during the course of the study due to equipment restrictions, microwave furnaces which have dedicated abilities to safely sinter samples in controlled environments have become more readily available commercially within the last few years. With higher heating rates and lower process times associated with microwave processing, further studies with this technology could yield increased process efficiency and refined microstructures for improved properties.

APPENDICES

Appendix A: Sample conditions table

Sample	Atmosphere	Thermal debinding conditions	Sintering/Infiltration conditions	Formed sample	Matrix Material	Infiltrate	Hypothesis Investigated
1	Hydrogen	450°C for one hour, and subsequently 700°C and held for another hour under Hydrogen	1250°C for 1 hour	Two material macro tensile bar	1µm tungsten powders	Copper	To determine the effect sample orientation and atmosphere have on the samples.
2	Vacuum						
3	Nitrogen						
4	Hydrogen	450°C for one hour, and subsequently 600°C and held for another hour under Hydrogen					To determine the effect presintering temperature has on
5		450°C for one hour, and subsequently 800°C and held for another hour under Hydrogen					
6		450°C for one hour, and subsequently 900°C and held for another hour under Hydrogen					

7	Hydrogen	450°C for one hour, and subsequently 700°C and held for another hour under Hydrogen	1150°C for 1 hour	Diagnostic component	1µm tungsten powders	Copper	Effect of sintering/infiltrating temperature on the samples made with 1µm tungsten powders
8			1200°C for 1 hour				
9			1250°C for 1 hour				
10			1150°C for 1 hour	Two material micro tensile bar	100nm tungsten powders		Effect of sintering/infiltrating temperature on the samples made with 100nm tungsten powders
11			1200°C for 1 hour				
12			1250°C for 1 hour				
13			1100°C for 1 hour				
14			1150°C for 5 minutes	Two material micro tensile bar	100nm tungsten powders		To investigate the effect reduced sintering/infiltration time had on the samples.
15			1150°C for 1 minute				
16			1150°C for 5 minutes	Rectangular bar	1µm tungsten mixed with 5.0wt% copper		To investigate the effect that an addition of 5.0wt% of copper would have on the sample
17		450°C for one hour,	1150°C for 1 hour	Two	1µm		To investigate the viability

		and subsequently heated directly to 1150°C		material macro	tungsten powders		of integrating thermal debinding and sintering/infiltration into one heat cycle.
18	Hydrogen	450°C for one hour, and subsequently 700°C and held for another hour under Hydrogen	N/A	Two material micro tensile bar	100nm tungsten powders	Copper	To investigate the viability of microwave sintering.
19		450°C for one hour, and subsequently heated directly to 1150°C	1150°C for 5 minutes		100nm tungsten powders		To investigate the effect of having an integrated heat cycle with a lower maximum temperature and shorter sintering time.
20				Diagnostic component	1µm tungsten powders		
21				Rectangular Bar	1µm tungsten mixed with 5.0wt% copper		

22	Hydrogen	No thermal debinding done as no binder was used	1150°C for 1 hour	PM pressed discs	100nm tungsten	No Infiltration	Investigate the effect yttria addition had on the structure of tungsten matrices formed using 100 nm tungsten powders
23					100nm tungsten doped with 2.0wt% yttria powders		
24					100nm tungsten doped with 4.0wt% yttria powders		
25					100nm tungsten doped with 6.0wt% yttria powders		

26	Hydrogen	No thermal debinding done as no binder was used	1150°C for 1 hour	PM pressed discs	1µm tungsten	No Infiltration	Investigate the effect yttria addition had on the structure of tungsten matrices formed using 1 µm tungsten powders
27					1µm tungsten doped with 2.0wt% yttria powders		
28					1µm tungsten doped with 4.0wt% yttria powders		
29					1µm tungsten doped with 6.0wt% yttria powders		

30	Hydrogen	450°C for one hour, and subsequently heated directly to 1150°C	1150°C for 5 minutes	Diagnostic component	1µm tungsten	Silver	Infiltration with silver
31	Hydrogen			Micro tensile bar	100nm tungsten		
32	Hydrogen			Rectangular Bar	1µm tungsten doped with 2.0wt% yttria		Infiltration of copper and silver into tungsten matrices made from 1µm tungsten powders and 2.0wt% yttria
33	Hydrogen				1µm tungsten doped with 2.0wt% yttria	Copper	

APPENDIX B: SUMMARY OF RESULTS

Summary of results for sample 1

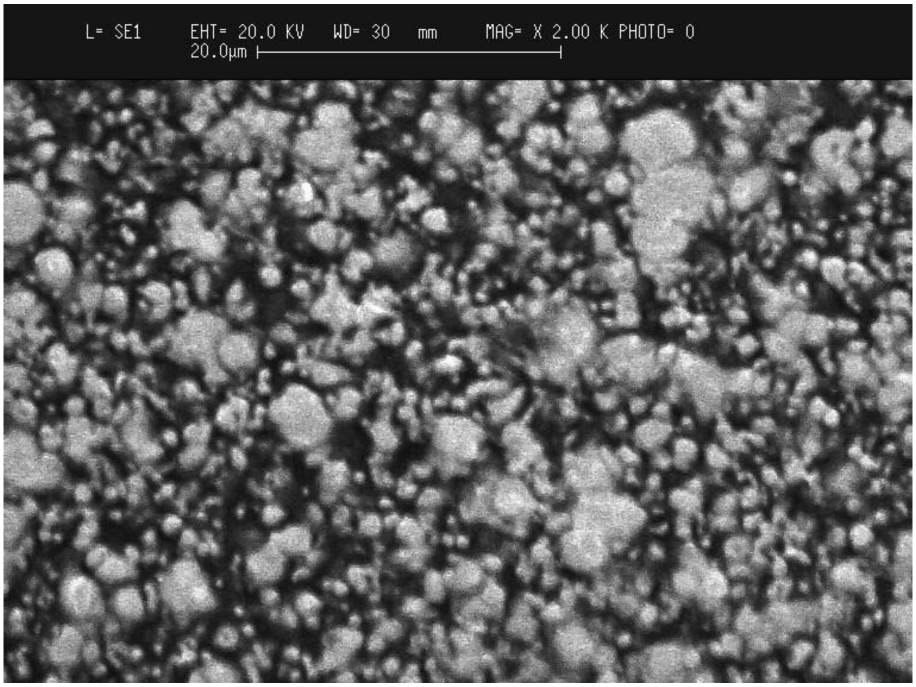

Figure B-1: SEM image (x2000) of copper infiltrated tungsten produced using 1µm tungsten powders with a pre-sintering temperature of 700°C and at a sintering/infiltration temperature of 1250°C for 1 hour under hydrogen.

Summary of results for sample 2 and 3

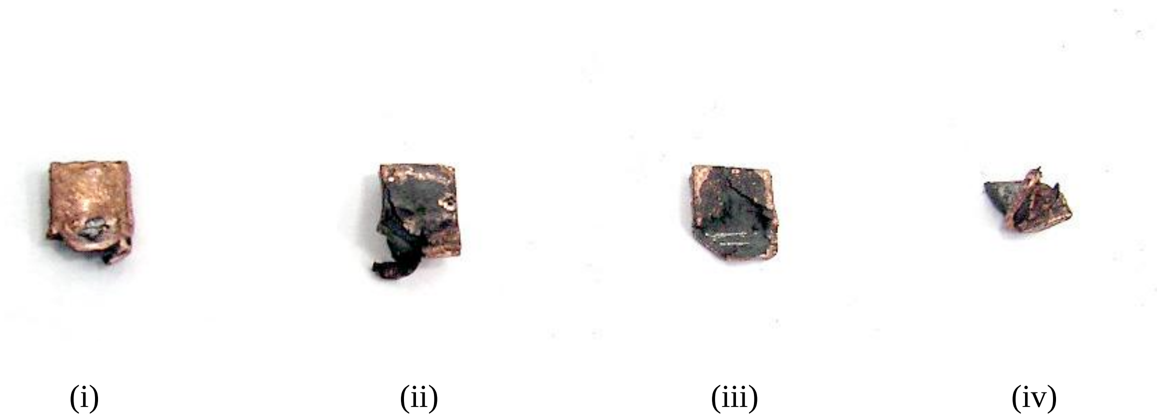

(i) (ii) (iii) (iv)

Figure B-2: Photo showing failed infiltration of samples sintered/infiltrated under conditions of vacuum (i and ii) and under nitrogen (iii and iv).

Summary of results for sample 4

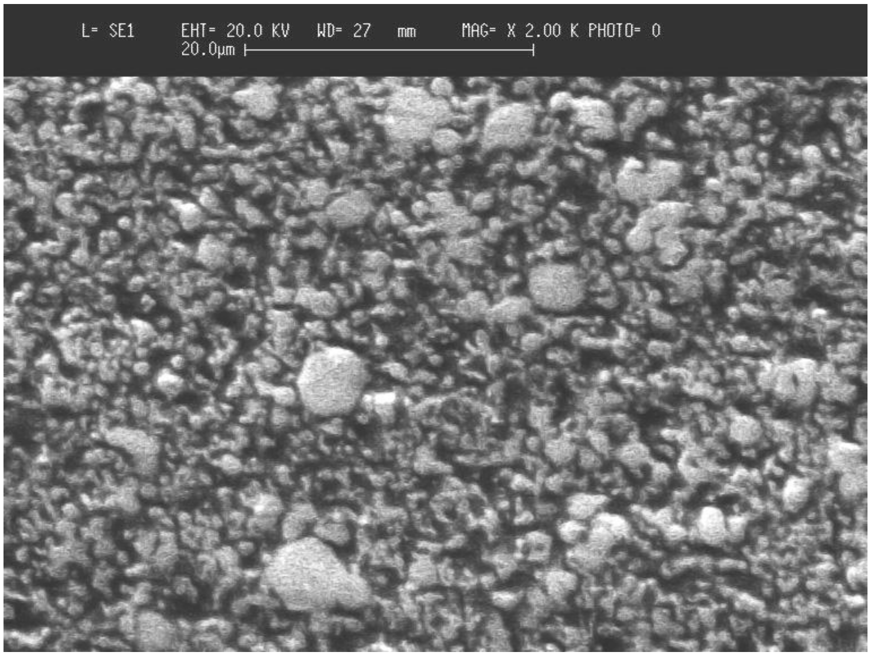

Figure B-3: SEM image (x2000) of copper infiltrated tungsten produced using 1µm tungsten powders with a pre-sintering temperature of 600°C and at a sintering/infiltration temperature of 1250°C for 1 hour under hydrogen.

Summary of results for sample 5

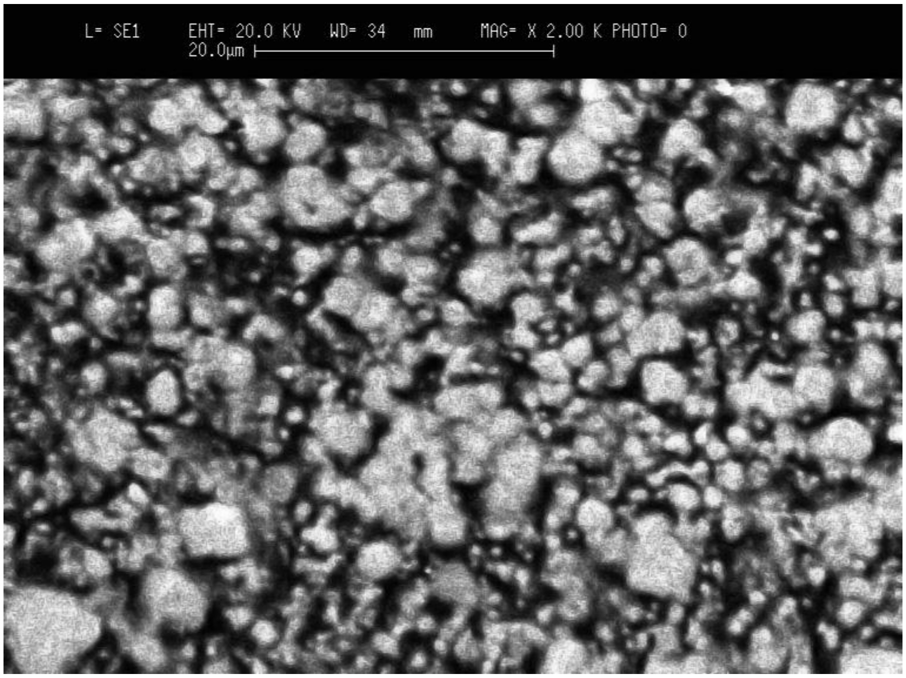

Figure B-4: SEM image (x2000) of copper infiltrated tungsten produced using 1µm tungsten powders with a pre-sintering temperature of 800°C and at a sintering/infiltration temperature of 1250°C for 1 hour under hydrogen.

Summary of results for sample 6

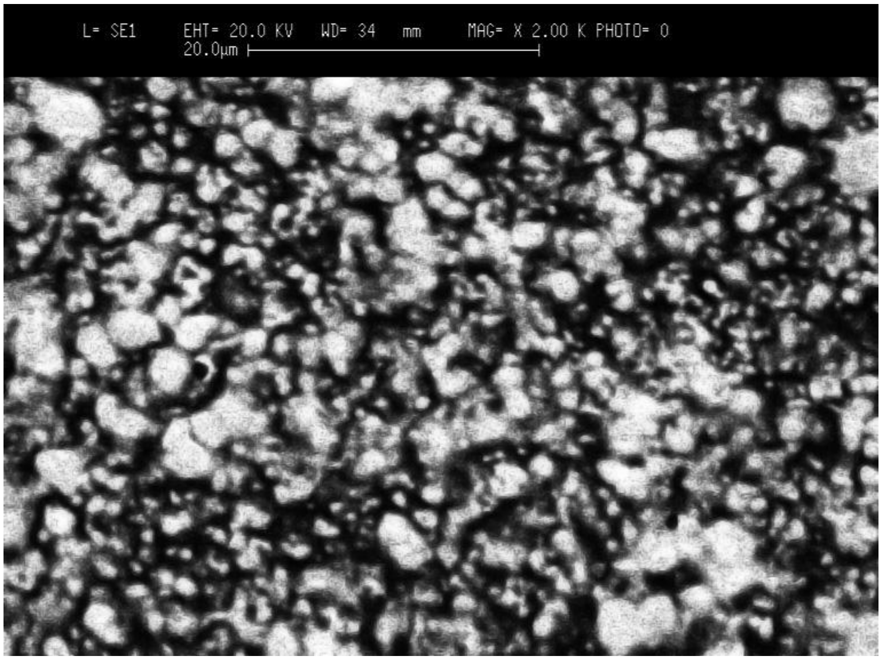

Figure B-5: SEM image (x2000) of copper infiltrated tungsten produced using 1µm tungsten powders with a pre-sintering temperature of 900°C and at a sintering/infiltration temperature of 1250°C for 1 hour under hydrogen.

Summary of results for sample 7

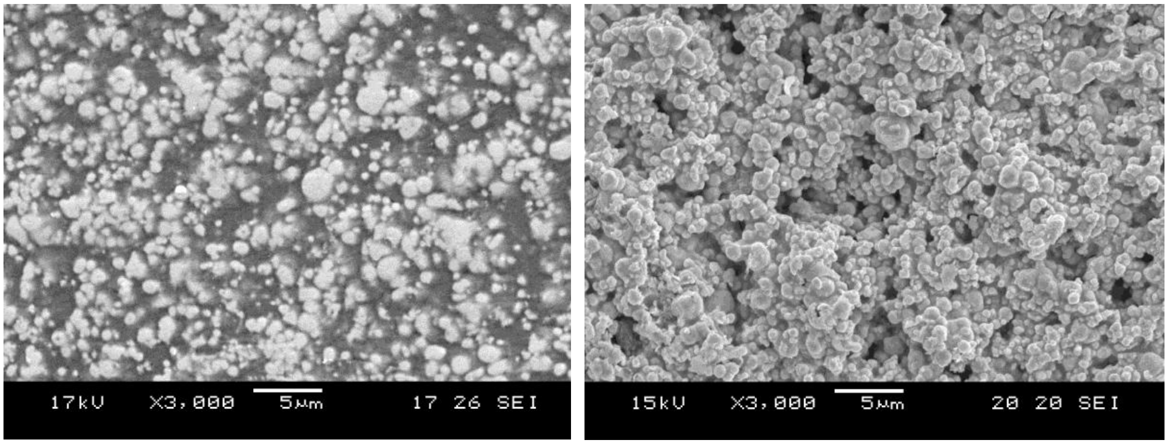

(i) (ii)

Figure B-6: SEM image (x3000) of (i) copper infiltrated tungsten and (ii), an uninfiltrated tungsten matrix, produced using 1µm tungsten powders with a pre-sintering temperature of 700°C and at a sintering/infiltration temperature of 1150°C for 1 hour under hydrogen.

Table B-1: Summary of properties for copper infiltrated tungsten produced using 1µm tungsten powders with a pre-sintering temperature of 700°C and at a sintering/infiltration temperature of 1150°C for 1 hour under hydrogen.

Composition	Wt% Copper	38.46
	Wt% Tungsten	61.54
Mean hardness (H_v)		205
Mean conductivity (%IACS)		44.70
Mean dimensional change (%)		-5.60
Mean CTE ($10^{-6}K^{-1}$)		13.05
Mean density (g/cm3)		13.45

Summary of results for sample 8

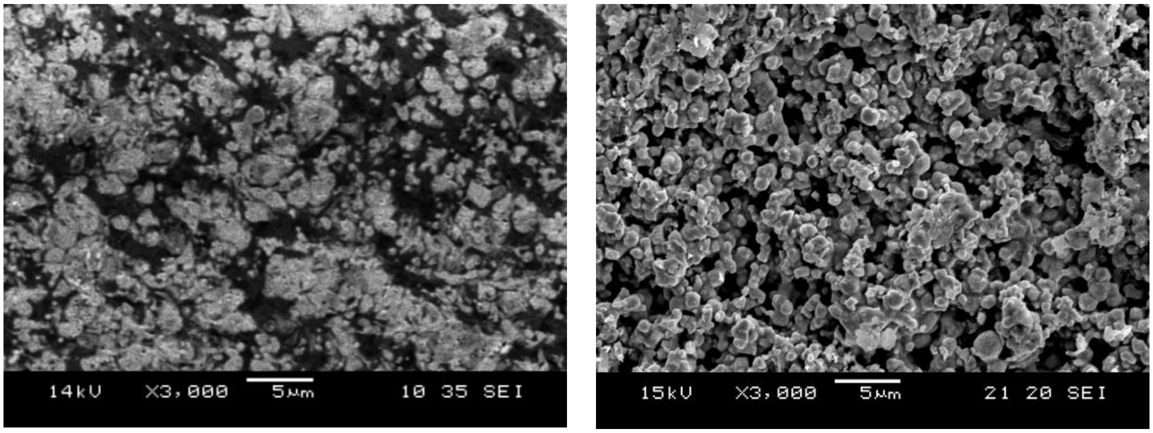

(i) (ii)

Figure B-7: SEM image (x3000) of (i) copper infiltrated tungsten and (ii), an uninfiltrated tungsten matrix, produced using 1µm tungsten powders with a pre-sintering temperature of 700°C and at a sintering/infiltration temperature of 1200°C for 1 hour under hydrogen.

Table B-2: Summary of properties for copper infiltrated tungsten produced using 1µm tungsten powders with a pre-sintering temperature of 700°C and at a sintering/infiltration temperature of 1200°C for 1 hour under hydrogen.

Composition	Wt% Copper	28.37
	Wt% Tungsten	71.63
Mean hardness (H_v)		231
Mean conductivity (%IACS)		41.03
Mean dimensional change (%)		-6.39
Mean CTE ($10^{-6}K^{-1}$)		12.73
Mean density (g/cm3)		13.54

Summary of results for sample 9

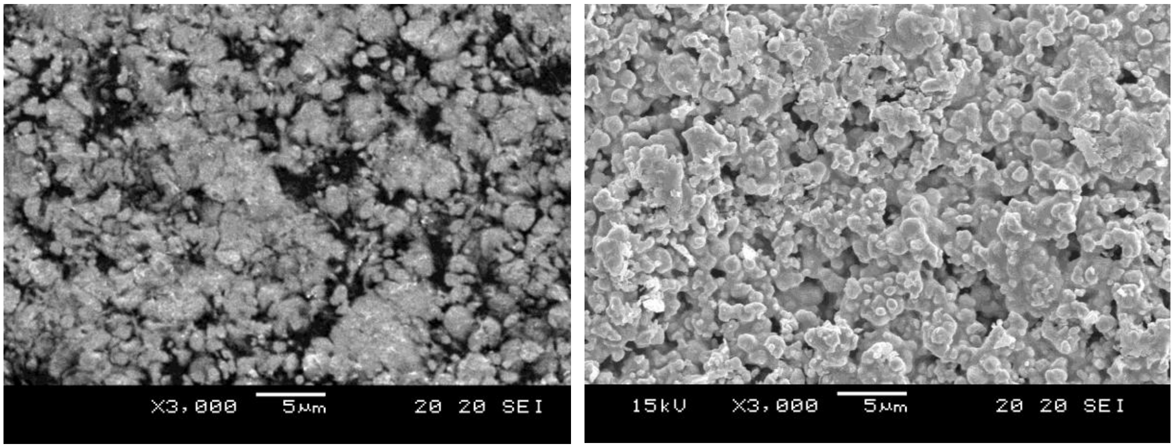

(i) (ii)

Figure B-8: SEM image (x3000) of (i) copper infiltrated tungsten and (ii), an uninfiltrated tungsten matrix, produced using 1µm tungsten powders with a pre-sintering temperature of 700°C and at a sintering/infiltration temperature of 1250°C for 1 hour under hydrogen.

Table B-3: Summary of properties for copper infiltrated tungsten produced using 1µm tungsten powders with a pre-sintering temperature of 700°C and at a sintering/infiltration temperature of 1250°C for 1 hour under hydrogen.

Composition	Wt% Copper	24.10
	Wt% Tungsten	75.90
Mean hardness (H_v)		247
Mean conductivity (%IACS)		42.22
Mean dimensional change (%)		-6.88
Mean CTE ($10^{-6}K^{-1}$)		10.50
Mean density (g/cm3)		13.62

Summary of results for sample 10

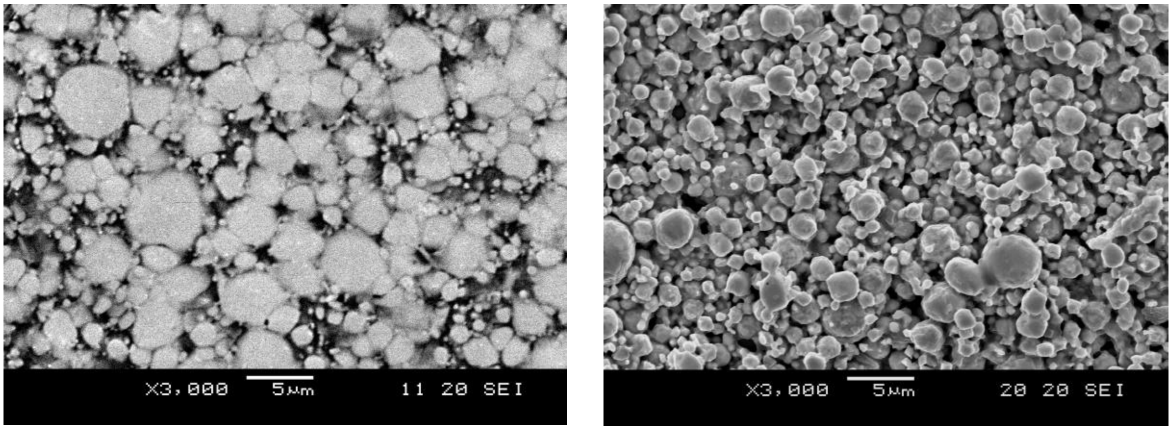

(i) (ii)

Figure B-9: SEM image (x3000) of (i) copper infiltrated tungsten and (ii), an uninfiltrated tungsten matrix, produced using 100nm tungsten powders with a pre-sintering temperature of 700°C at a sintering/infiltration temperature of 1250°C for 1 hour under hydrogen.

Table B-4: Summary of properties for copper infiltrated tungsten produced using 100nm tungsten powders with a pre-sintering temperature of 700°C at a sintering/infiltration temperature of 1250°C for 1 hour under hydrogen.

Composition	Wt% Copper	18.32
	Wt% Tungsten	81.68
Mean hardness (H_v)		253
Mean conductivity (%IACS)		21.91
Mean dimensional change (%)		-7.01
Mean CTE ($10^{-6}K^{-1}$)		13.56
Mean density (g/cm3)		14.47

Summary of results for sample 11

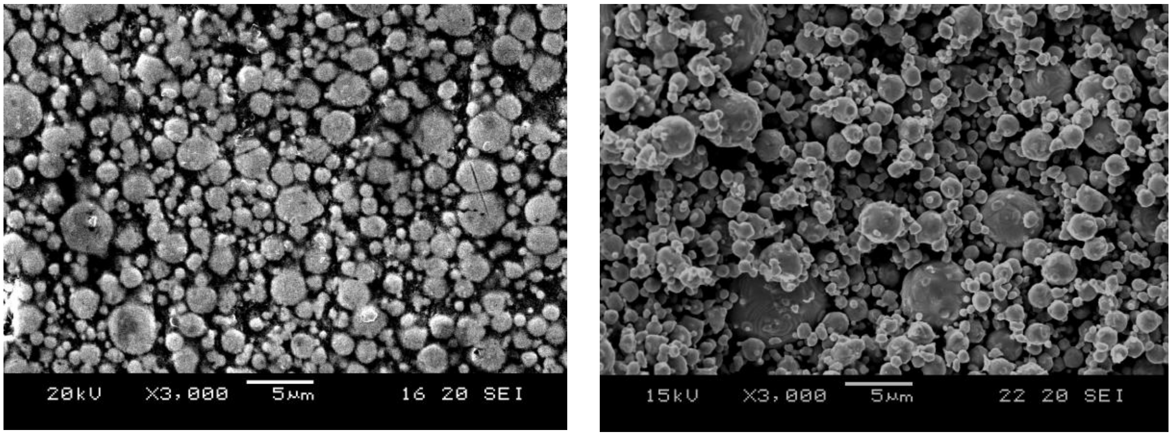

(i) (ii)

Figure B-10: SEM image (x3000) of (i) copper infiltrated tungsten and (ii), an uninfiltrated tungsten matrix, produced using 100nm tungsten powders with a pre-sintering temperature of 700°C and at a sintering/infiltration temperature of 1200°C for 1 hour under hydrogen.

Table B-5: Summary of properties for copper infiltrated tungsten produced using 100nm tungsten powders with a pre-sintering temperature of 700°C and at a sintering/infiltration temperature of 1200°C for 1 hour under hydrogen.

Composition	Wt% Copper	16.56
	Wt% Tungsten	83.44
Mean hardness (H_v)		239
Mean conductivity (%IACS)		19.65
Mean dimensional change (%)		-6.88
Mean CTE ($10^{-6}K^{-1}$)		13.99
Mean density (g/cm3)		13.43

Summary of results for sample 12

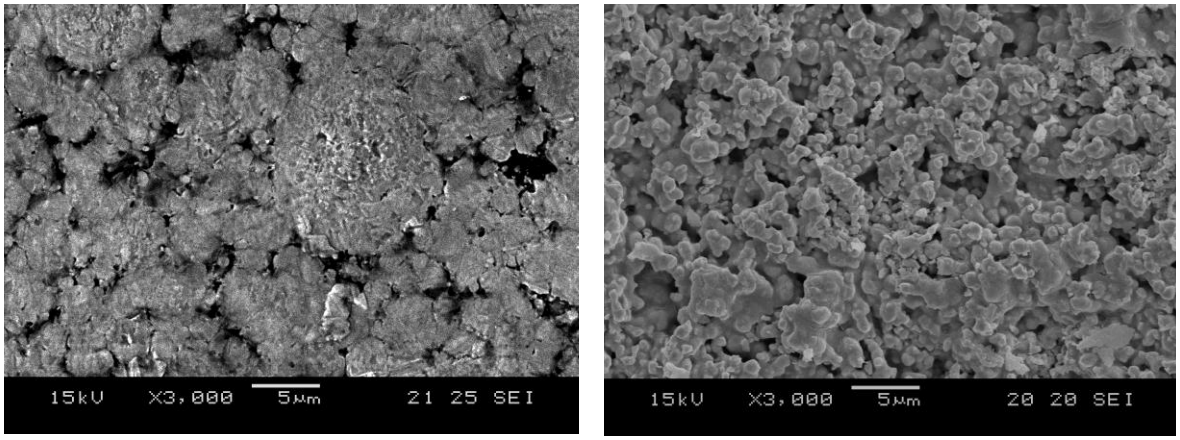

(i) (ii)

Figure B-11: SEM image (x3000) of (i) copper infiltrated tungsten and (ii), an uninfiltrated tungsten matrix, produced using 100nm tungsten powders with a pre-sintering temperature of 700°C and at a sintering/infiltration temperature of 1250°C for 1 hour under hydrogen.

Table B-6: Summary of properties for copper infiltrated tungsten produced using 100nm tungsten powders with a pre-sintering temperature of 700°C and at a sintering/infiltration temperature of 1250°C for 1 hour under hydrogen.

Composition	Wt% Copper	14.11
	Wt% Tungsten	85.89
Mean hardness (H_v)		244
Mean conductivity (%IACS)		19.76
Mean dimensional change (%)		-7.14
Mean CTE ($10^{-6}K^{-1}$)		13.46
Mean density (g/cm3)		13.78

Summary of results for sample 13

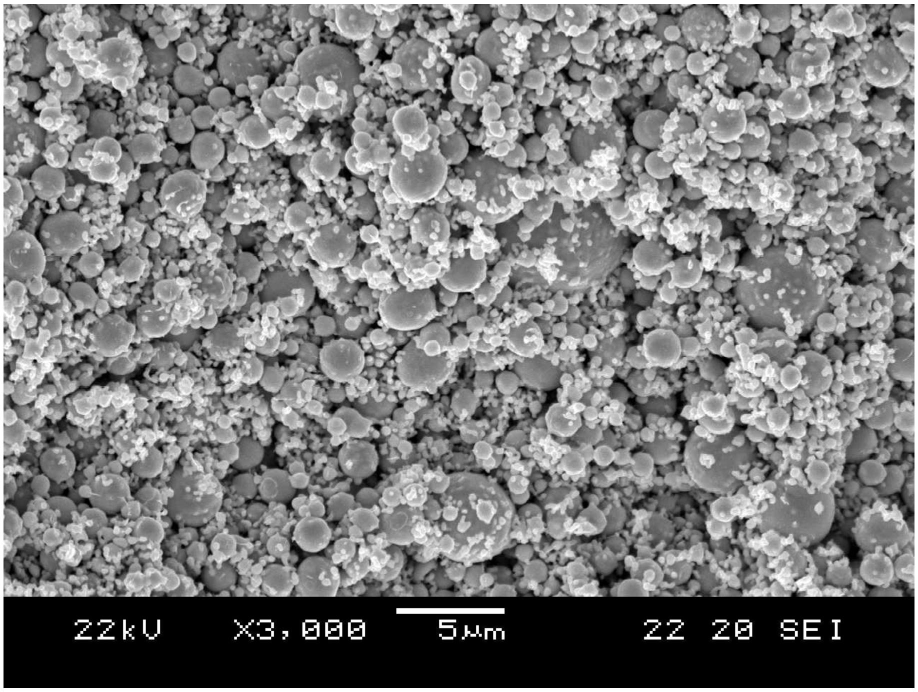

Figure B-12: SEM image (x3000) showing uninfiltrated tungsten matrix produced using 1µm tungsten powders with a pre-sintering temperature of 700°C and at a sintering/infiltration temperature of 1250°C for 1 hour under Hydrogen. No infiltration occurred for all sample 13 parameters.

Summary of results for sample 14

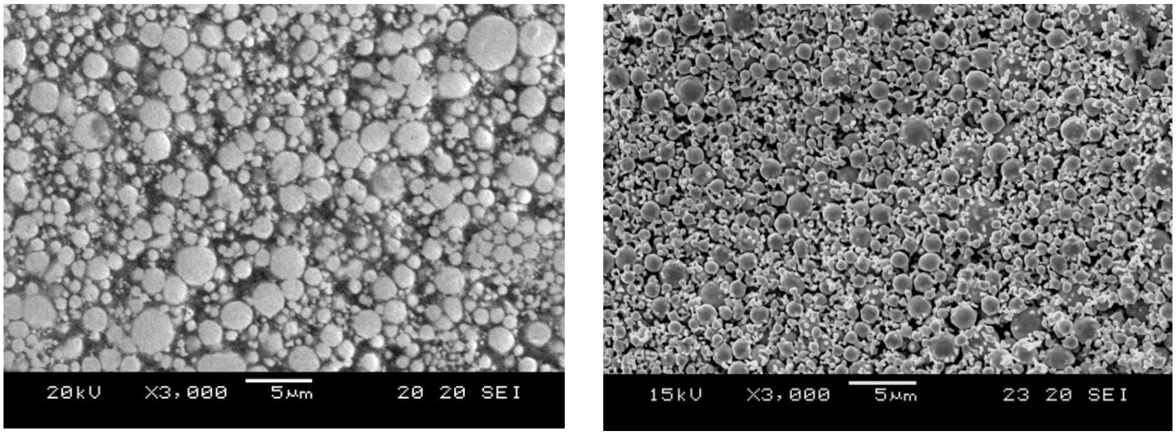

(i) (ii)

Figure B-13: SEM image (x3000) of (i) copper infiltrated tungsten and (ii), an uninfiltrated tungsten matrix, produced using 100nm tungsten powders with a pre-sintering temperature of 700°C and at a sintering/infiltration temperature of 1150°C for 5 minutes under hydrogen.

Table B-7: Summary of properties for copper infiltrated tungsten produced using 100nm tungsten powders with a pre-sintering temperature of 700°C and at a sintering/infiltration temperature of 1150°C for 5 minutes under hydrogen.

Composition	Wt% Copper	25.75
	Wt% Tungsten	74.25
Mean hardness (H_v)		287
Mean conductivity (%IACS)		24.50
Mean dimensional change (%)		-1.67
Mean CTE ($10^{-6}K^{-1}$)		14.86
Mean density (g/cm3)		14.15

Summary of results for sample 15

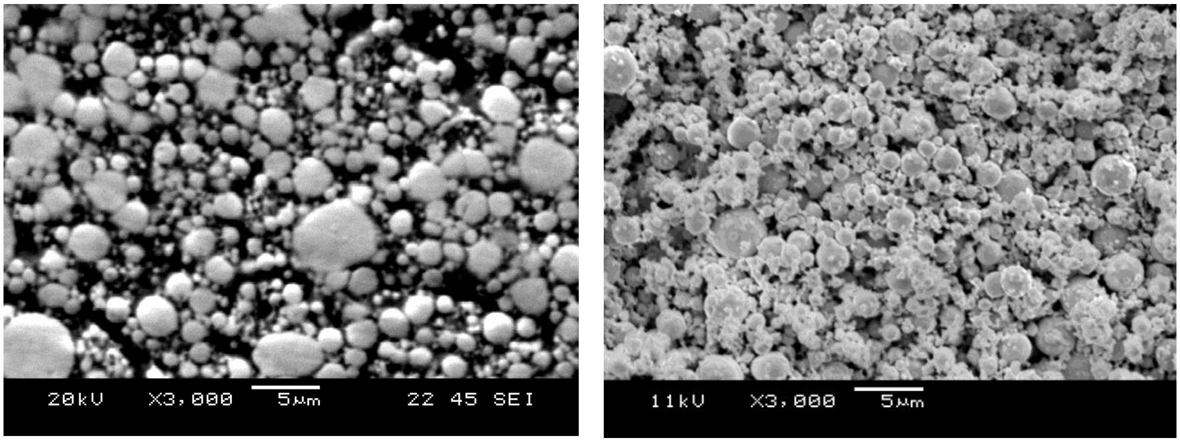

(i) (ii)

Figure B-14: SEM image (x3000) of (i) copper infiltrated tungsten and (ii), an uninfiltrated tungsten matrix, produced using 100nm tungsten powders with a pre-sintering temperature of 700°C and at a sintering/infiltration temperature of 1150°C for 1 minute under hydrogen.

Table B-8: Summary of properties for copper infiltrated tungsten produced using 100nm tungsten powders with a pre-sintering temperature of 700°C and at a sintering/infiltration temperature of 1150°C for 1 minute under hydrogen.

Composition	Wt% Copper	10.28
	Wt% Tungsten	89.72
Mean hardness (H_v)		281
Mean conductivity (%IACS)		27.69
Mean dimensional change (%)		-6.59
Mean CTE ($10^{-6}K^{-1}$)		14.80
Mean density (g/cm3)		14.24

Summary of results for sample 16

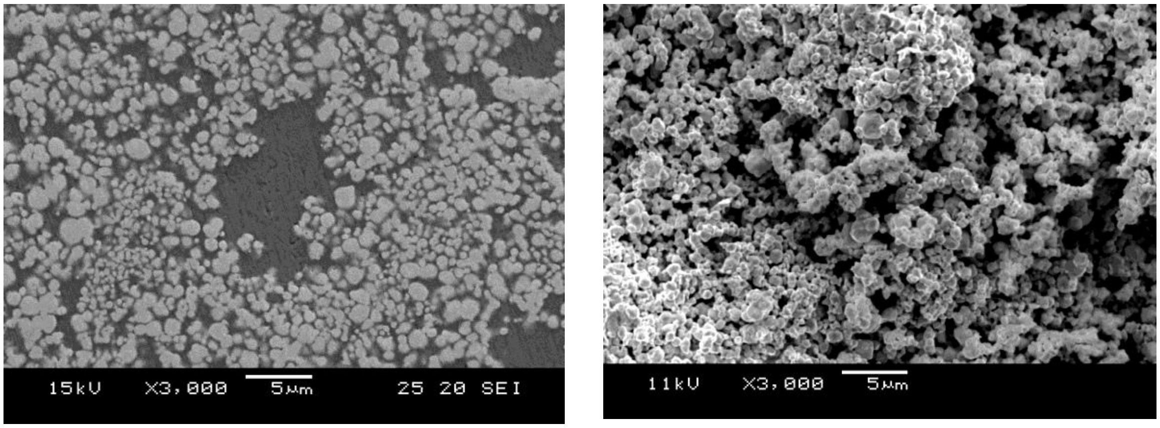

(i) (ii)

Figure B-15: SEM image (x3000) of (i) copper infiltrated tungsten and (ii), an uninfiltrated tungsten matrix, produced using 1µm tungsten powders premixed with 5.0wt% copper with a pre-sintering temperature of 700°C and at a sintering/infiltration temperature of 1150°C for 5 minutes under hydrogen.

Table B-9: Summary of properties for copper infiltrated tungsten produced using 1µm tungsten powders premixed with 5.0wt% copper with a pre-sintering temperature of 700°C and at a sintering/infiltration temperature of 1150°C for 5 minutes under hydrogen.

Composition	Wt% Copper	34.17
	Wt% Tungsten	65.83
Mean hardness (H_v)		217
Mean conductivity (%IACS)		31.13
Mean dimensional change (%)		-5.66
Mean CTE ($10^{-6}K^{-1}$)		13.00
Mean density (g/cm3)		13.41

Summary of results for sample 17

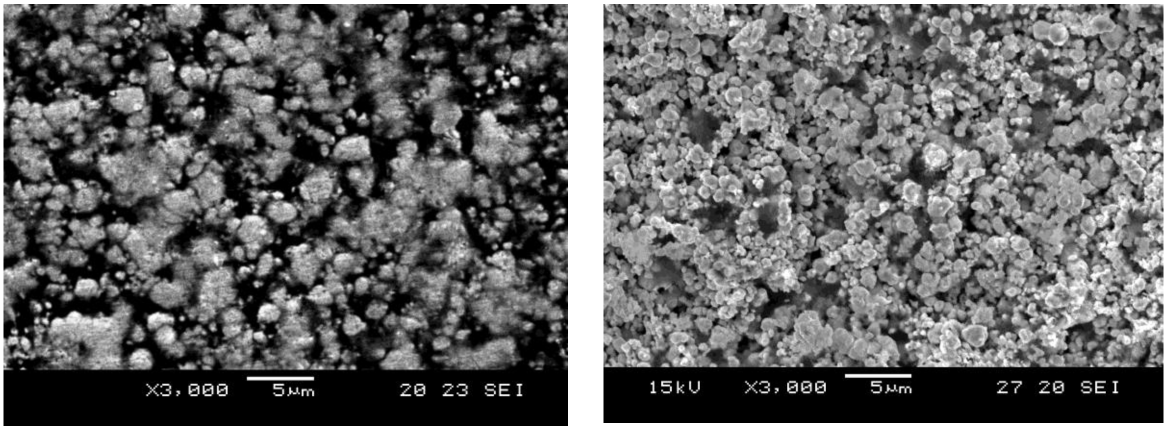

(i) (ii)

Figure B-16: SEM image (x3000) of (i) copper infiltrated tungsten and (ii), an uninfiltrated tungsten matrix, produced using 1μm tungsten powders and a direct sintering heating profile with a sintering/infiltration temperature of 1150°C for 1 hour under hydrogen.

Table B-10: Summary of properties for copper infiltrated tungsten produced using 1μm tungsten powders and a direct sintering heating profile with a sintering/infiltration temperature of 1150°C for 1 hour under hydrogen.

Composition	Wt% Copper	31.74
	Wt% Tungsten	68.26
Mean hardness (H_v)		221
Mean conductivity (%IACS)		41.06
Mean dimensional change (%)		-6.36
Mean CTE ($10^{-6}K^{-1}$)		14.71
Mean density (g/cm3)		13.70

Summary of results for sample 18

Figure B-17: Photo showing Copper (II) Carbonate that was extracted from the crucible of the microwave furnace. No infiltration occurred in the process.

Summary of results for sample 19

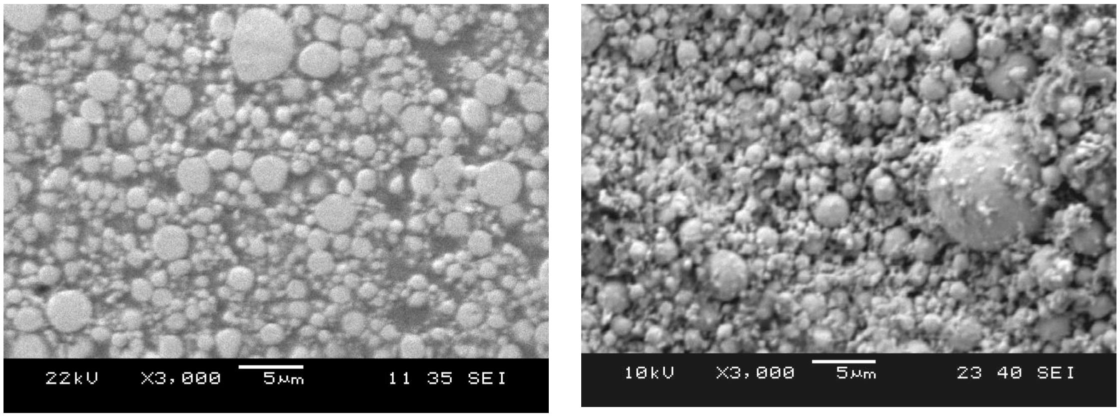

(i) (ii)

Figure B-18: SEM image (x3000) of (i) copper infiltrated tungsten and (ii), an uninfiltrated tungsten matrix, produced using 100nm tungsten powders and a direct sintering heating profile with a sintering/infiltration temperature of 1150°C for 5 minutes under hydrogen.

Table B-11: Summary of properties for copper infiltrated tungsten produced using 100nm tungsten powders and a direct sintering heating profile with a sintering/infiltration temperature of 1150°C for 5 minutes under hydrogen.

Composition	Wt% Copper	32.98
	Wt% Tungsten	67.02
Mean hardness (H_v)		190
Mean conductivity (%IACS)		26.59
Mean dimensional change (%)		-8.96
Mean CTE ($10^{-6}K^{-1}$)		15.01
Mean density (g/cm3)		14.04

Summary of results for sample 20

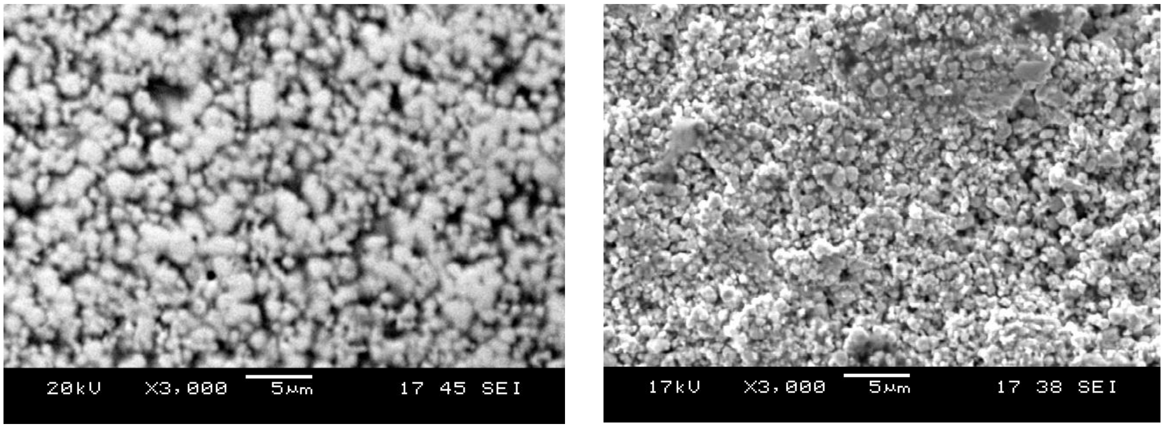

(i) (ii)

Figure B-19: SEM image (x3000) of (i) copper infiltrated tungsten and (ii), an uninfiltrated tungsten matrix, produced using 1µm tungsten powders and a direct sintering heating profile with a sintering/infiltration temperature of 1150°C for 5 minutes under hydrogen.

Table B-12: Summary of properties for copper infiltrated tungsten produced using 1µm tungsten powders and a direct sintering heating profile with a sintering/infiltration temperature of 1150°C for 5 minutes under hydrogen.

Composition	Wt% Copper	34.62
	Wt% Tungsten	65.38
Mean hardness (H_v)		198
Mean conductivity (%IACS)		26.21
Mean dimensional change (%)		-4.17
Mean CTE ($10^{-6}K^{-1}$)		13.21
Mean density (g/cm3)		13.62

Summary of results for sample 21

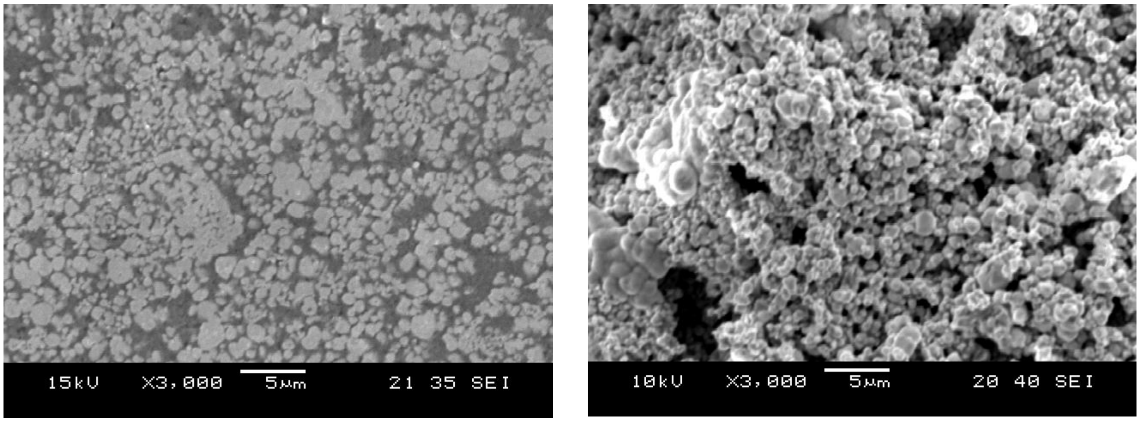

(i) (ii)

Figure B-20: SEM image (x3000) of (i) copper infiltrated tungsten and (ii), an uninfiltrated tungsten matrix, produced using 1µm tungsten powders premixed with 5.0wt% copper and a direct sintering heating profile with a sintering/infiltration temperature of 1150°C for 5 minutes under hydrogen.

Table B-13: Summary of properties for copper infiltrated tungsten produced using 1µm tungsten powders premixed with 5.0wt% copper and a direct sintering heating profile with a sintering/infiltration temperature of 1150°C for 5 minutes under hydrogen.

Composition	Wt% Copper	40.43
	Wt% Tungsten	59.57
Mean hardness (H_v)		161
Mean conductivity (%IACS)		29.33
Mean dimensional change (%)		-9.84
Mean CTE ($10^{-6}K^{-1}$)		14.81
Mean density (g/cm3)		12.63

Summary of results for sample 22

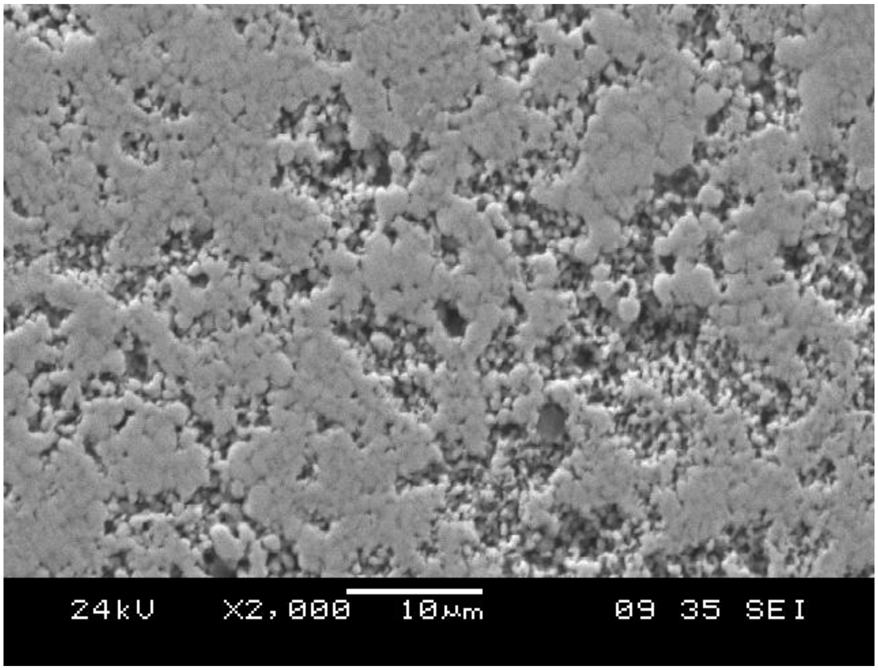

Figure B-21: SEM image (x2000) of a PM pressed disc made from 100nm tungsten powders sintered at 1150°C for 1 hour.

Table B-14: Hardness of a PM pressed disc made from 100nm tungsten powders sintered at 1150°C for 1 hour.

Mean hardness (H_v)	114

Summary of results for sample 23

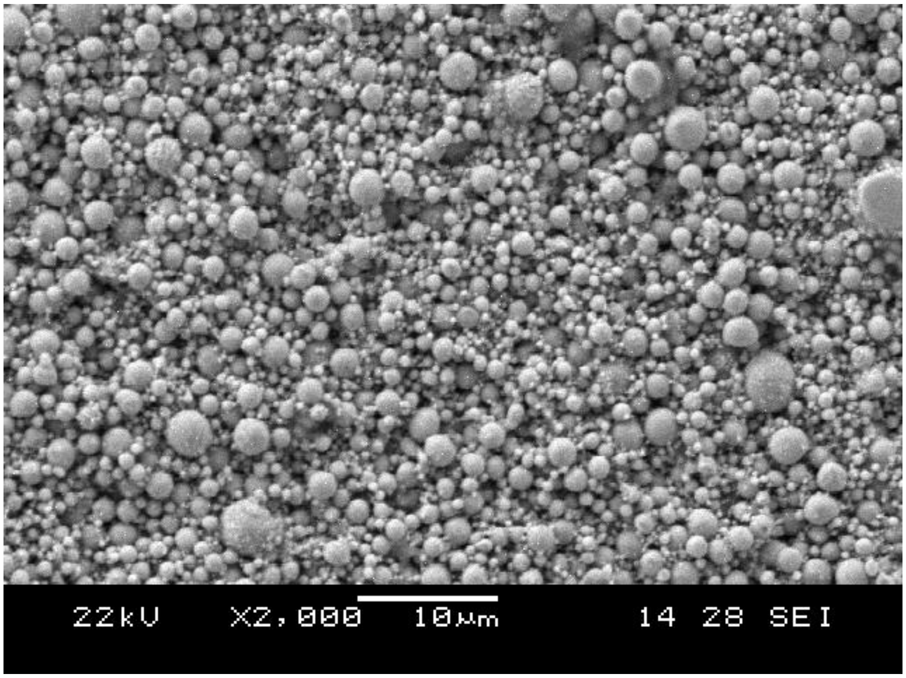

Figure B-22: SEM image (x2000) of a PM pressed disc made from 100nm tungsten powders doped with 2.0wt% yttria sintered at 1150°C for 1 hour.

Table B-15: Hardness of a PM pressed disc made from 100nm tungsten powders doped with 2.0wt% yttria sintered at 1150°C for 1 hour.

Mean hardness (H_v)	79

Summary of results for sample 24

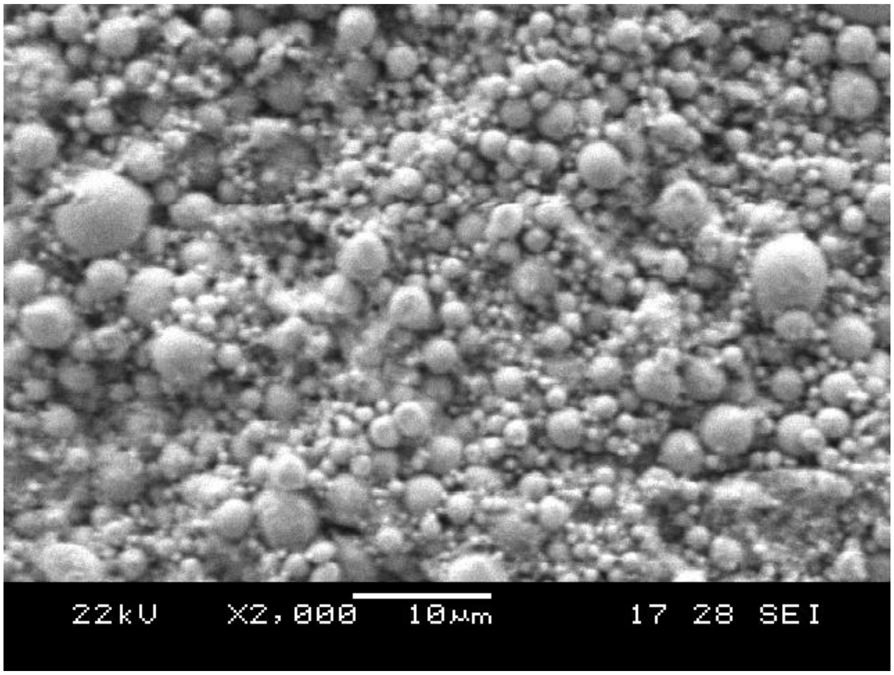

Figure B-23: SEM image (x2000) of a PM pressed disc made from 100nm tungsten powders doped with 4.0wt% yttria sintered at 1150°C for 1 hour.

Table B-16: Hardness of a PM pressed disc made from 100nm tungsten powders doped with 4.0wt% yttria sintered at 1150°C for 1 hour.

Mean hardness (H_v)	61

Summary of results for sample 25

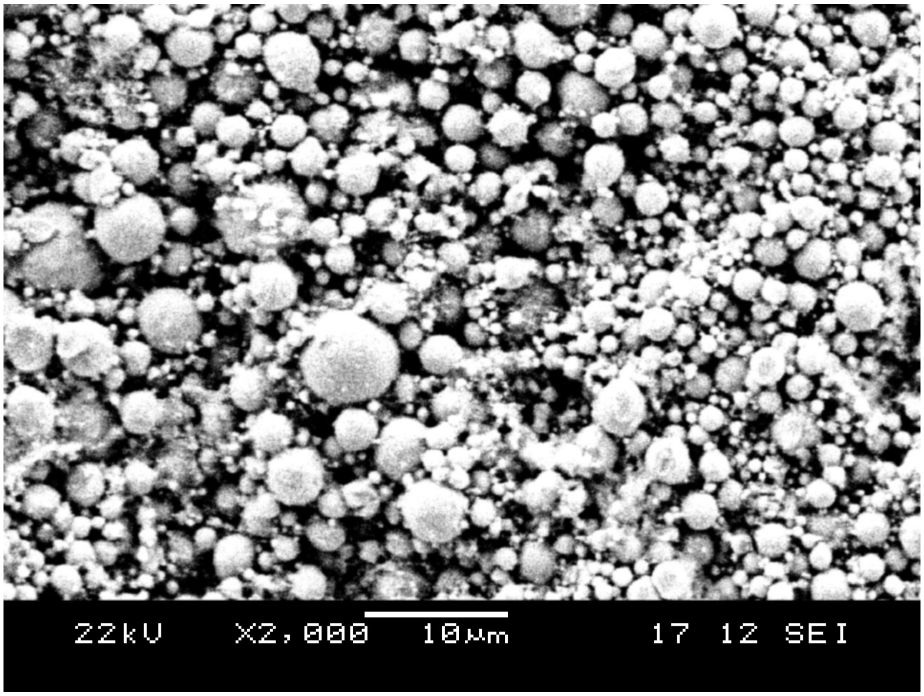

Figure B-24: SEM image (x2000) of a PM pressed disc made from 100nm tungsten powders doped with 6.0wt% yttria sintered at 1150°C for 1 hour.

Table B-17: Hardness of a PM pressed disc made from 100nm tungsten powders doped with 6.0wt% yttria sintered at 1150°C for 1 hour.

Mean hardness (H_v)	82

Summary of results for sample 26

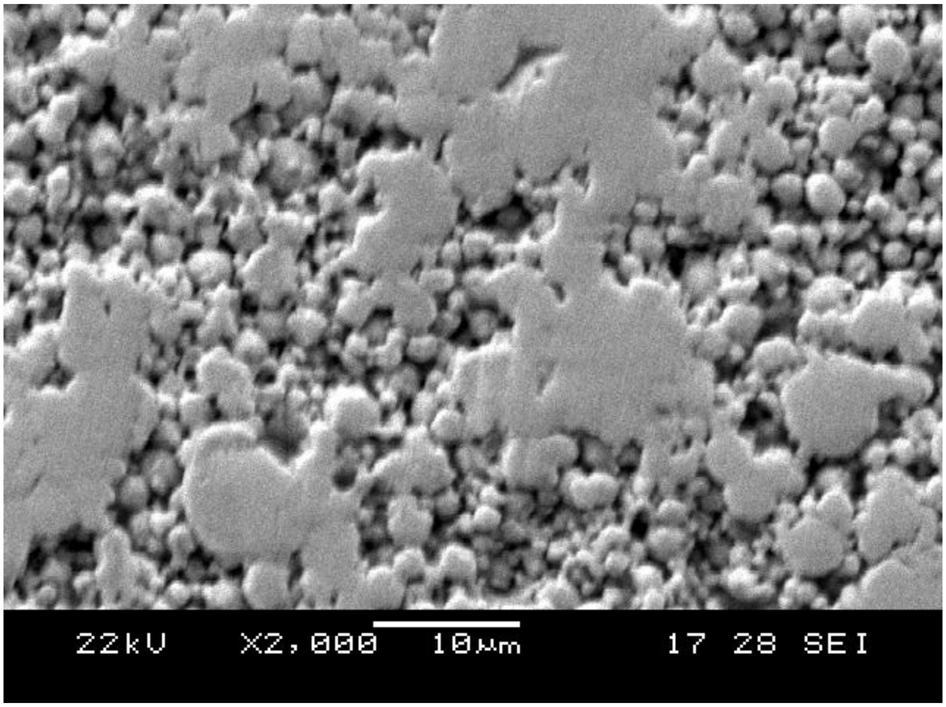

Figure B-25: SEM image (x2000) of a PM pressed disc made from 1µm tungsten powders sintered at 1150°C for 1 hour.

Table B-18: Hardness of a PM pressed disc made from 1µm tungsten powders sintered at 1150°C for 1 hour.

Mean hardness (H_v)	119

Summary of results for sample 27

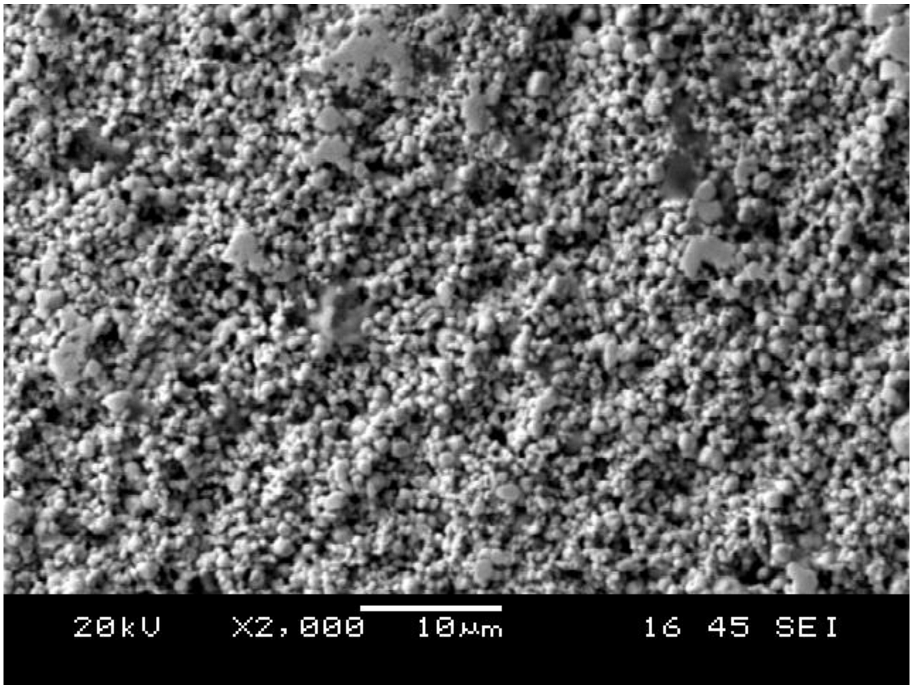

Figure B-26: SEM image (x2000) of a PM pressed disc made from 1µm tungsten powders doped with 2.0wt% yttria sintered at 1150°C for 1 hour.

Table B-19: Hardness of a PM pressed disc made from 1µm tungsten powders doped with 2.0wt% yttria sintered at 1150°C for 1 hour.

Mean hardness (H_v)	52

Summary of results for sample 28

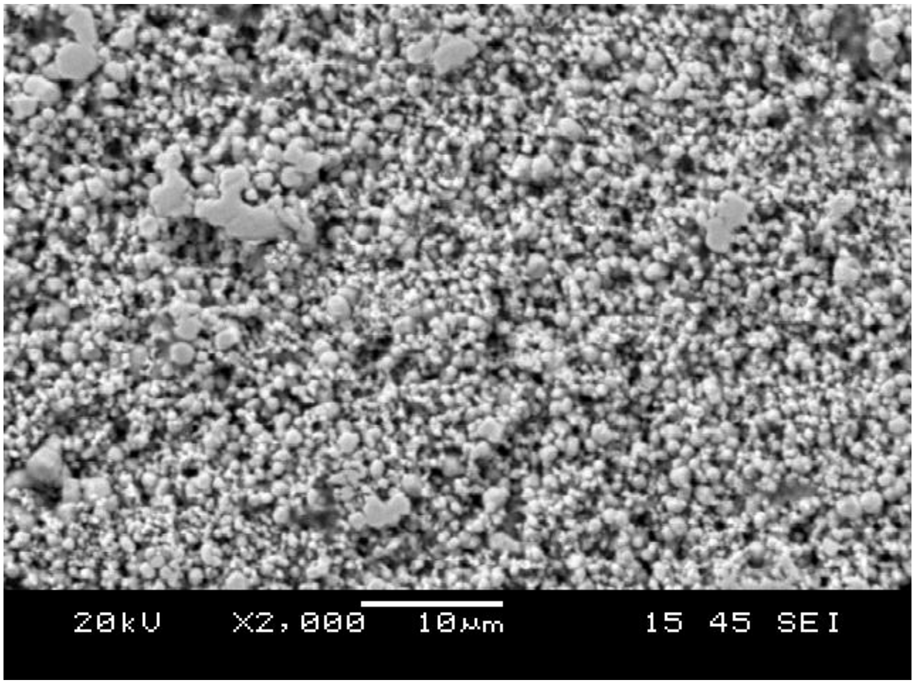

Figure B-27: SEM image (x2000) of a PM pressed disc made from 1µm tungsten powders doped with 4.0wt% yttria sintered at 1150°C for 1 hour.

Table B-20: Hardness of a PM pressed disc made from 1µm tungsten powders doped with 4.0wt% yttria sintered at 1150°C for 1 hour.

Mean hardness (H_v)	39

Summary of results for sample 29

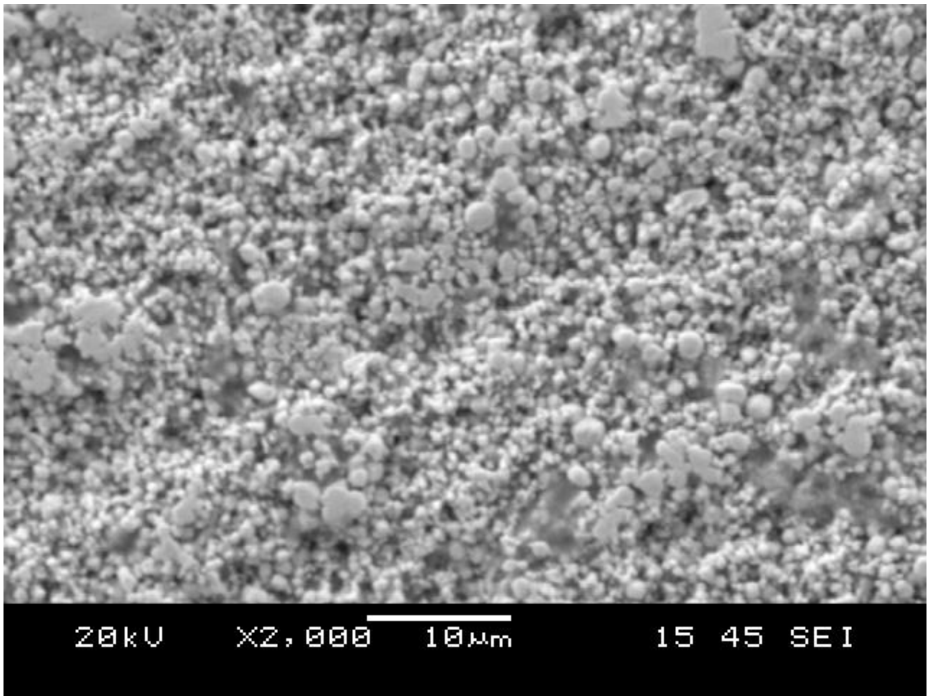

Figure B-28: SEM image (x2000) of a PM pressed disc made from 1µm tungsten powders doped with 6.0wt% yttria sintered at 1150°C for 1 hour.

Table B-21: Hardness of a PM pressed disc made from 1µm tungsten powders doped with 6.0wt% yttria sintered at 1150°C for 1 hour.

Mean hardness (H_v)	39

Summary of results for sample 30

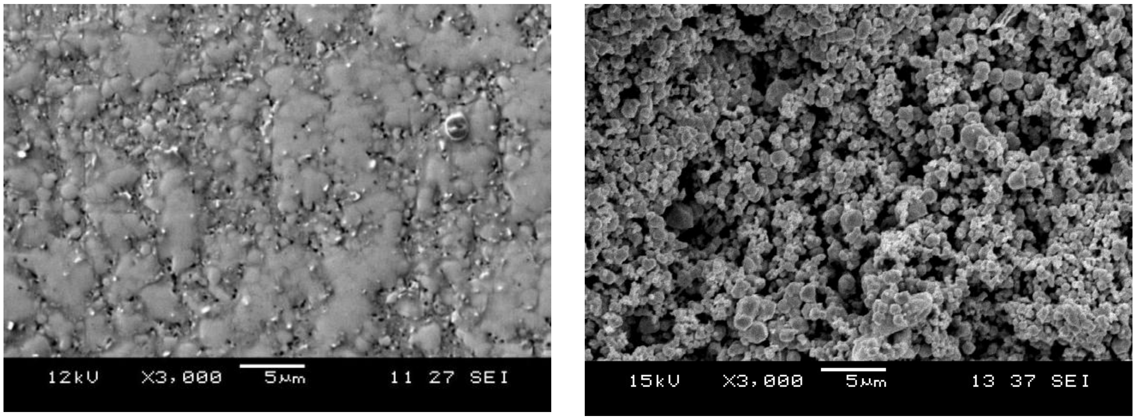

(i) (ii)

Figure B-29: SEM image (x3000) of (i) silver infiltrated tungsten and (ii), an uninfiltrated tungsten matrix, produced using 1µm tungsten powders and a direct sintering heating profile with a sintering/infiltration temperature of 1150°C for 5 minutes under hydrogen.

Table B-22: Summary of properties for copper infiltrated tungsten produced using 1µm tungsten powders and a direct sintering heating profile with a sintering/infiltration temperature of 1150°C for 5 minutes under hydrogen.

Composition	Wt% Silver	36.41
	Wt% Tungsten	63.59
Mean hardness (H_v)		133
Mean conductivity (%IACS)		51.02
Mean dimensional change (%)		-2.22
Mean CTE ($10^{-6}K^{-1}$)		15.10
Mean density (g/cm3)		13.16

Summary of results for sample 31

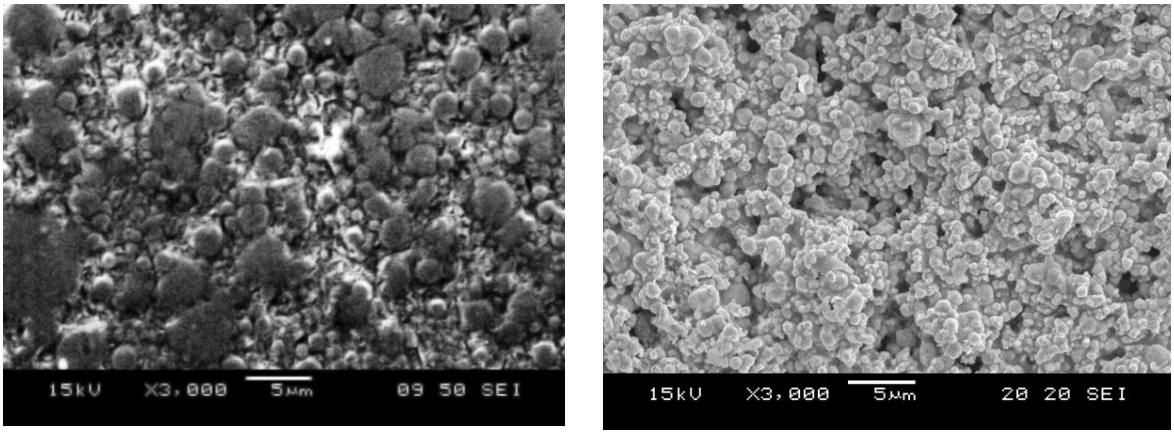

(i) (ii)

Figure B-30: SEM image (x3000) of (i) silver infiltrated tungsten and (ii), an uninfiltrated tungsten matrix, produced using 100nm tungsten powders and a direct sintering heating profile with a sintering/infiltration temperature of 1150°C for 5 minutes under hydrogen.

Table B-23: Summary of properties for copper infiltrated tungsten produced using 100nm tungsten powders and a direct sintering heating profile with a sintering/infiltration temperature of 1150°C for 5 minutes under hydrogen.

Composition	Wt% Silver	28.74
	Wt% Tungsten	71.26
Mean hardness (H_v)		153
Mean conductivity (%IACS)		42.30
Mean dimensional change (%)		-4.33
Mean CTE ($10^{-6}K^{-1}$)		14.31
Mean density (g/cm3)		14.51

Summary of results for sample 32

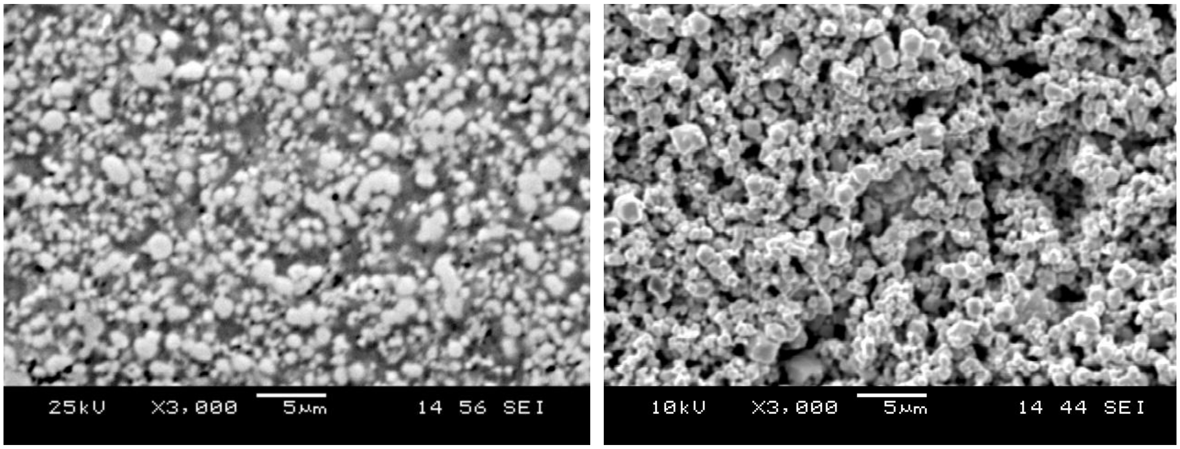

(i) (ii)

Figure B-31: SEM image (x3000) of (i) silver infiltrated tungsten and (ii), an uninfiltrated tungsten matrix, produced using 1µm tungsten powders doped with 2.0wt% yttria and a direct sintering heating profile and a sintering/infiltration temperature of 1150°C for 5 minutes under hydrogen.

Table B-24: Summary of properties for copper infiltrated tungsten produced using 1µm tungsten powders doped with 2.0wt% yttria and a direct sintering heating profile and a sintering/infiltration temperature of 1150°C for 5 minutes under hydrogen.

Composition	Wt% Silver	37.53
	Wt% Tungsten	58.98
	Wt% Yttrium	1.37
	Wt% Oxygen	2.12
Mean hardness (H_v)		127
Mean conductivity (%IACS)		53.49
Mean dimensional change (%)		-3.94
Mean CTE ($10^{-6}K^{-1}$)		13.03
Mean density (g/cm3)		13.48

Summary of results for sample 33

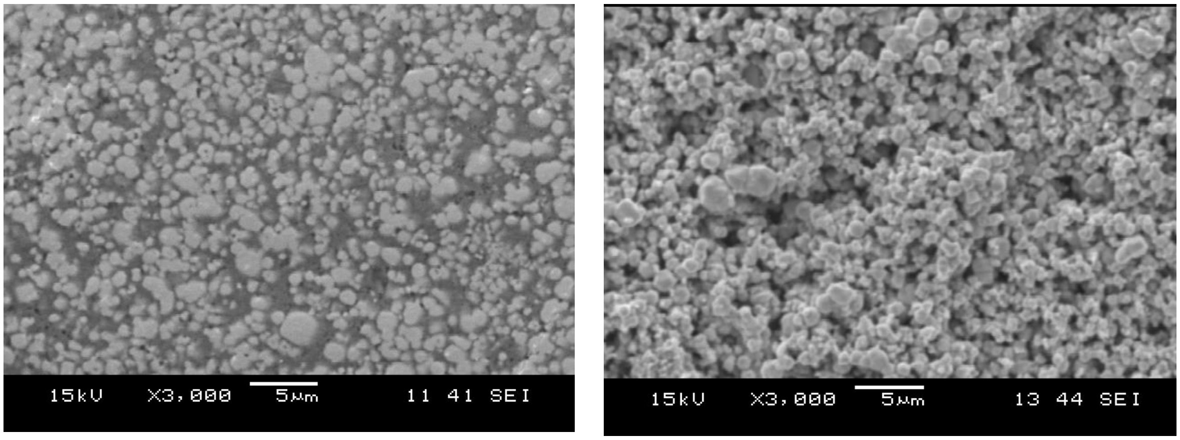

(i) (ii)

Figure B-32: SEM image (x3000) of (i) copper infiltrated tungsten and (ii), an uninfiltrated tungsten matrix, produced using 1µm tungsten powders doped with 2.0wt% yttria and a direct sintering heating profile and a sintering/infiltration temperature of 1150°C for 5 minutes under hydrogen.

Table B-25: Summary of properties for copper infiltrated tungsten produced using 1µm tungsten powders doped with 2.0wt% yttria and a direct sintering heating profile and a sintering/infiltration temperature of 1150°C for 5 minutes under hydrogen.

Composition	Wt% Copper	34.33
	Wt% Tungsten	64.01
	Wt% Yttrium	1.66
	Wt% Oxygen	2.44
Mean hardness (H_v)		215
Mean conductivity (%IACS)		24.21
Mean dimensional change (%)		-2.19
Mean CTE ($10^{-6}K^{-1}$)		13.54
Mean density (g/cm3)		15.72

APPENDIX C: LIST OF PUBLICATIONS

The 4th International Conference on Materials Processing for Properties and Performance (MP3) 30th November – 2nd December 2005 Tsukuba Science City Ibaraki, Japan

P.W. Ho, Q.F. Li, J. Y. H. Fuh, S.F. Pook, Studies on Properties of Vacuum Sintered Zirconia, Materials Processing for Properties and Performance (MP3) Vol. 4, pp. 116-120, 2005

S.F. Pook, Eric, Q.F. Li, N.H Loh, P.W. Ho, M.K. Ho, Studies on Powder Injection Molding (PIM) of Nanosize Alumina (Al2O3) Powder, Materials Processing for Properties and Performance (MP3) Vol. 4, pp. 111-115, 2005

International Conference on Advances in Materials, Product Design & Manufacturing Systems, 12 -14 December, 2005, Bannari Amman Institute of Technology, Sathyamangalam - 638 401, Erode Dt., Tamil Nadu India

P.W. Ho, Q.F. Li, J. Y. H. Fuh, Studies on W-CU composite materials produced by combination of powder injection molding and CU infiltration, Advances in Materials, Product Design & Manufacturing Systems, pp. 109-114, 2005

The 5th International Conference on Materials Processing for Properties and Performance (MP3) 11 - 15 December 2006, Singapore

P.W. Ho, Q.F. Li, J. Y. H. Fuh, Q.Y. Wong, Effect of sintering temperatures on properties of copper-tungsten metal matrix composites produced by two-colour powder injection moulding, Materials Processing for Properties and Performance (MP3) Vol. 5, pp.212-214, 2006

Materials Science and Engineering A

P.W. Ho, Q.F. Li, J. Y. H. Fuh, Evaluation of W-Cu metal matrix composites produced by powder injection molding and liquid infiltration, Materials Science and Engineering A, Vol. 485 pp.657–663, 2008

P.W. Ho, Q.F. Li, J. Y. H. Fuh, Forming of metal matrix composite components by liquid phase joining of porous metal preforms, Materials Science and Engineering A, Submitted.

The Fifteenth International Conference on composites and nano engineering (ICCE-15), 15-21 July 2007 Hainan Island, China

P.W. Ho, Q.F. Li , J.Y.H. Fuh, P.C.Yu , Liquid Phase Joining of Porous Metals to Produce Metal Matrix Composites, Fifteenth International Conference on composites and Nano Engineering, pp. 320-321, 2007

The 8th Asia Pacific Conference on Materials Processing, (8TH APCMP), 2008,
15-20 June, Guilin-Guangzhou, China

P.W. Ho, Q.F. Li, J. Y. H. Fuh, S. Ma, Effect of Yttria addition on the structure and hardness of porous tungsten matrices, Proceedings of the 8th Asia Pacific Conference on Materials Processing, pp 143-147, 2008

The 2nd International conference on Science and Technology, (ICSTIE 08), 2008,
12-13 December, Kuala Lumpur, Malaysia.

P.W. Ho, Q.F. Li , J.Y.H. Fuh, Comparative studies between W-Ag and W-Cu Metal Matrix composites produced by powder injection moulding, Proceedings of the International Conference on Science and Technology (ICSTIE ’08), pp. 101-104, 2008.

Microsystem Technologies

P. C. Yu, Q. F. Li, J. Y. H. Fuh, T. Li and P. W. Ho, Micro injection molding of micro gear using nano-sized zirconia powder, Vol. 15, No. 3, pp. 401-406, 2009